AEDC-TR-87-45

C-5

Evaluation of Wall Interference Assessment and Correction Techniques

W. L. Sickles and J. C. Erickson, Jr.
Calspan Corporation/AEDC Division

June 1988

Final Report for Period October 1, 1986 – September 30, 1987

TECHNICAL REPORTS
FILE COPY

PROPERTY OF U.S. AIR FORCE
AEDC TECHNICAL LIBRARY

Approved for public release; distribution unlimited.

ARNOLD ENGINEERING DEVELOPMENT CENTER
ARNOLD AIR FORCE BASE, TENNESSEE
AIR FORCE SYSTEMS COMMAND
UNITED STATES AIR FORCE

NOTICES

When U. S. Government drawings, specifications, or other data are used for any purpose other than a definitely related Government procurement operation, the Government thereby incurs no responsibility nor any obligation whatsoever, and the fact that the Government may have formulated, furnished, or in any way supplied the said drawings, specifications, or other data, is not to be regarded by implication or otherwise, or in any manner licensing the holder or any other person or corporation, or conveying any rights or permission to manufacture, use, or sell any patented invention that may in any way be related thereto.

Qualified users may obtain copies of this report from the Defense Technical Information Center.

References to named commercial products in this report are not to be considered in any sense as an endorsement of the product by the United States Air Force or the Government.

This report has been reviewed by the Office of Public Affairs (PA) and is releasable to the National Technical Information Service (NTIS). At NTIS, it will be available to the general public, including foreign nations.

APPROVAL STATEMENT

This report has been reviewed and approved.

Approved for publication:

FOR THE COMMANDER

Marion L. Laster

MARION L. LASTER
Technical Director
Directorate of Technology
Deputy for Operations

UNCLASSIFIED
SECURITY CLASSIFICATION OF THIS PAGE

REPORT DOCUMENTATION PAGE

Form Approved OMB No. 0704-0188

1a. REPORT SECURITY CLASSIFICATION Unclassified	1b. RESTRICTIVE MARKINGS
2a. SECURITY CLASSIFICATION AUTHORITY	3. DISTRIBUTION/AVAILABILITY OF REPORT Approved for public release; distribution unlimited.
2b. DECLASSIFICATION/DOWNGRADING SCHEDULE	
4. PERFORMING ORGANIZATION REPORT NUMBER(S) AEDC-TR-87-45	5 MONITORING ORGANIZATION REPORT NUMBER(S)
6a. NAME OF PERFORMING ORGANIZATION Arnold Engineering Development Center 6b OFFICE SYMBOL (If applicable) DOF	7a. NAME OF MONITORING ORGANIZATION
6c. ADDRESS (City, State, and ZIP Code) Air Force Systems Command Arnold Air Force Base, TN 37389-5000	7b ADDRESS (City, State, and ZIP Code)
8a. NAME OF FUNDING/SPONSORING ORGANIZATION Arnold Engineering Development Center 8b. OFFICE SYMBOL (If applicable) DOT	9 PROCUREMENT INSTRUMENT IDENTIFICATION NUMBER
8c. ADDRESS (City, State, and ZIP Code) Air Force Systems Command Arnold Air Force Base, TN 37389-5000	10. SOURCE OF FUNDING NUMBERS PROGRAM ELEMENT NO. 65807F PROJECT NO. 9R02 TASK NO WORK UNIT ACCESSION NO

11 TITLE (Include Security Classification)

Evaluation of Wall Interference Assessment and Correction Techniques (U)

12. PERSONAL AUTHOR(S)
Sickles, W.L. and Erickson, J.C., Jr., Calspan Corporation/AEDC Division

13a. TYPE OF REPORT	13b. TIME COVERED	14. DATE OF REPORT (Year, Month, Day)	15. PAGE COUNT
Final	FROM 10/1/86 TO 9/30/87	June 1988	111

16. SUPPLEMENTARY NOTATION

Available in Defense Technical Information Center (DTIC).

17. COSATI CODES			18. SUBJECT TERMS (Continue on reverse if necessary and identify by block number)
FIELD	GROUP	SUB-GROUP	wall interference, flight performance prediction, transonic testing, assessment/correction techniques, wind tunnel data
14	02		

19. ABSTRACT (Continue on reverse if necessary and identify by block number)

Evaluation of wall interference correction procedures developed at AEDC was performed using experimental data. The correction procedures incorporated the use of measured data made on an interface near the tunnel wall and the use of two flow-field solvers, a transonic small disturbance solver and an Euler solver. Interference corrections were calculated for data obtained in Tunnel 1T with varying amounts of interference. Results are given for representative subcritical, mildly supercritical, and supercritical flows. Calculated interference levels are compared to experimental interference levels between the interference-free reference data from Tunnel 4T and the data with interference from Tunnel 1T.

20. DISTRIBUTION/AVAILABILITY OF ABSTRACT ☐ UNCLASSIFIED/UNLIMITED ☒ SAME AS RPT ☐ DTIC USERS	21. ABSTRACT SECURITY CLASSIFICATION Unclassified
22a NAME OF RESPONSIBLE INDIVIDUAL Carlton L. Garner	22b TELEPHONE (Include Area Code) (615) 454-7813 22c. OFFICE SYMBOL DOCS

DD Form 1473, JUN 86 Previous editions are obsolete.

SECURITY CLASSIFICATION OF THIS PAGE
UNCLASSIFIED

PREFACE

The work reported herein was conducted by the Arnold Engineering Development Center (AEDC), Air Force Systems Command (AFSC), under Program Element 65807F, Control Number 9R02, at the request of the AEDC Directorate of Technology (DOT). The AEDC/DOT project manager was Dr. M. L. Laster. The results were obtained by the Calspan Corporation/AEDC Division, operating contractor for the Aerospace Flight Dynamics testing effort at the AEDC, AFSC, Arnold Air Force Base, Tennessee. The manuscript was submitted for publication on March 31, 1988.

CONTENTS

Page

1.0 INTRODUCTION 7
2.0 WIAC DATA BASE 8
3.0 WIAC PROCEDURES 9
3.1 Single-Measured-Variable Procedures 10
3.2 Two-Measured-Variable Procedures 12
4.0 CODES AND FLOW SOLVERS 12
5.0 RESULTS AND DISCUSSION 13
5.1 TUNCOR SMV Procedure 14
5.2 Categorization of Results 14
5.3 Subcritical and Mildly Supercritical Flow 14
5.4 Strongly Supercritical Flow 19
5.5 Interface Results 25
6.0 CONCLUDING REMARKS 26

REFERENCES 27

ILLUSTRATIONS

Figure Page

1. Three-Dimensional Experimental Model 31
2. Aerodynamic Wind Tunnel (1T) Interface Measurement System 32
3. AEDC Single-Measured-Variable Procedure 33
4. TUNCOR Single-Measured-Variable Procedure 34
5. AEDC Two-Measured-Variable Procedure 35
6. Model Pressures Measured and Calculated Using the SMV-TSD Code, $M_E = 0.80$ and $\alpha_E = 0$ deg 36
7. Model Local Corrections Measured and Calculated Using the SMV-TSD Code, $M_E = 0.80$ and $\alpha_E = 0$ deg 39
8. Model Pressures Measured and Calculated Using the SMV-TSD Code, $M_E = 0.80$ and $\alpha_E = 6$ deg 42
9. Model Local Corrections Measured and Calculated Using the SMV-TSD Code, $M_E = 0.80$ and $\alpha_E = 6$ deg 45
10. Corrected Lift Coefficient at α_E and α_T Using the SMV-TSD Code for $M_E = 0.80$ 48

Figure | Page

11. Model Pressures Measured and Calculated Using the SMV-TSD Code While Matching Measured Lift, 60-percent Wing Semispan, M_E = 0.80, and α_T = 9.5 deg 49
12. Model Local Corrections Measured and Calculated Using the SMV-TSD Code While Matching Measured Lift, 60-percent Wing Semispan, M_E = 0.80 , α_E = 6 deg, and α_T = 9.5 deg 50
13. Corrected Lift Coefficient at α_E and α_T Using the SMV-TSD and SMV-TUNCOR Codes for M_E = 0.90 51
14. Model Pressures Measured and Calculated Using the SMV-TSD Code, M_E = 0.90 and α_E = 0 deg 52
15. Model Local Corrections Measured and Calculated Using the SMV-TSD Code, M_E = 0.90 and α_E = 0 deg 55
16. Model Pressures Measured and Calculated Using the SMV-Euler Code, M_E = 0.90 and α_E = 0 deg 58
17. Model Local Corrections Measured and Calculated Using the SMV-Euler and SMV-TSD Codes, M_E = 0.90 and α_E = 0 deg 61
18. Model Pressures Measured and Calculated Using the SMV-TSD Code, M_E = 0.90 and α_E = 4 deg 64
19. Model Local Corrections Measured and Calculated Using the SMV-TSD Code, M_E = 0.90 and α_E = 4 deg 67
20. Corrected Lift Coefficient at α_E and α_T Using the SMV-TSD, SMV-Euler, and Pretest-Euler Codes for M_E = 0.90 70
21. Model Pressures Measured and Calculated Using the SMV-Euler Code, M_E = 0.90 and α_E = 4 deg 71
22. Model Local Corrections Measured and Calculated Using the SMV-Euler and SMV-TSD Codes, M_E = 0.90 and α_E = 4 deg 76
23. Model Local Corrections Measured and Calculated Using the Pretest-Euler and SMV-Euler Codes, M_E = 0.90 and α_E = 4 deg 79
24. Interface Pressures Measured and Calculated Using the Pretest-Euler Code, M_E = 0.90, α_E = 4 deg, and τ = 3 percent 82
25. Interface $\partial v_n/\partial x$ Measured and Calculated Using the Pretest-Euler Code, M_E = 0.90, α_E = 4 deg, and τ = 3 percent 86
26. Interface $\partial v_n/\partial x$ Measured and Calculated Using the SMV-Euler and Pretest-Euler Codes, M_E = 0.90, α_E = 4 deg, and τ = 3 percent 90

Figure | Page

27. Interface Pressures Measured and Calculated Using the Euler Code, M_E = 0.90 and α_E = 4 deg 92
28. Interface Pressures Measured and Calculated Using the Euler Code, M_E = 0.90, and α_E = 4 deg 96
29. Interface $\partial v_n/\partial x$ Measured and Calculated Using the Euler Code, M_E = 0.90 and α_E = 4 deg 98

TABLES

Tables | Page

1. Test Conditions in Aerodynamic Wind Tunnel (1T) 102
2. Lift Coefficient Increments-Subcritical and Mildly Supercritical Cases, SMV-TSD Results 103
3. Lift Coefficient Increments-Strongly Supercritical Cases, SMV-TSD Results 104
4. Lift Coefficient Increments-Comparison of TSD and Euler Flow Solvers, M_E = 0.90 and α_E = 4 deg 105

NOMENCLATURE 106

1.0 INTRODUCTION

Wall interference in three-dimensional (3-D) transonic testing has been identified as a significant source of error when wind tunnel data are used to predict flight performance (Ref. 1). Wall interference can produce significant errors even when small models below the standard one-percent blockage criteria or incremental data are used, as shown in Ref. 2. Wall interference effects can also appear to be Reynolds number effects because Reynolds number affects the wall boundary layer, thereby changing the perforated wall characteristics. Consequently, it is important to account for wall interference at transonic speeds.

AEDC has recognized the importance of accounting for wall interference and has had a continuous, comprehensive program to develop techniques to determine and minimize the effects of wall interference in transonic wind tunnel tests. Advances in three major technologies have evolved from this program:

1. Pretest prediction of 3-D transonic wall interference is now routinely performed for production wind tunnel tests using advanced computational fluid dynamics techniques and a local semi-empirical description of perforated wall characteristics.

2. Wall interference assessment/correction (WIAC) techniques have been developed for 3-D transonic flow, and initial evaluation of these techniques has been accomplished using numerical simulations.

3. A 3-D variable porosity adaptive-wall system has successfully eliminated wall interference at near sonic conditions.

Pretest prediction, WIAC, and the adaptive wall are complementary approaches to the wall interference problem. The development of the first and last technologies is given in Refs. 2, 3, 4, and 5. This report will emphasize the WIAC approach but will use results and data from the other efforts in the evaluation process.

A WIAC technique uses boundary data measured on or near the wind tunnel wall. This technique differs from the predictive technique, which uses a model of the wall boundary condition in lieu of measurements. A WIAC technique consists of two components: (1) a flow solver that adequately represents the tunnel and free-air flows, and (2) a procedure for using the measured boundary data and the flow solver to determine wall interference.

Application of WIAC techniques to two-dimensional (2-D) flow is well established for subsonic and transonic flows and is summarized in Ref. 6. Techniques for 3-D flows have

been developed and numerically investigated through simulation, and are reported in Ref. 2. To perform an extensive experimental evaluation, a data base was obtained in Aerodynamic Wind Tunnel (1T) with various levels of interference and in Aerodynamic Wind Tunnel (4T) for interference-free reference data. This report will concentrate on the development and experimental evaluation of the 3-D WIAC techniques using the Tunnel 1T data base.

2.0 WIAC DATA BASE

To perform an extensive experimental evaluation of the WIAC codes and procedures, it is necessary to have a good experimental data base. Such data were primarily provided as a byproduct of the adaptive-wall experimental program in Tunnel 1T. Additional experimental data were obtained in Tunnel 1T with the adaptive-wall test section to assist in the design effort of a measurement system for Tunnel 4T.

The generic wing-body-tail configuration employed in the experiments is shown in Fig. 1 and has wing and tail surfaces midmounted on an axisymmetric body. The lifting surfaces have constant chord NACA-0012 sections and are swept 30 deg. Model instrumentation includes 134 pressure orifices distributed as shown in Fig. 1, and strain gages applied to the sting support to measure normal force, pitching moment, and sting deflection. Although balance instrumentation provides more reliable force and moment data, the gages were utilized because the pressure tubing did not leave sufficient space for balance instrumentation. The pressure measurements on the model were required to make detailed comparisons of pressure distributions between Tunnel 1T and the reference data. The gages gave reasonable quality lift data that were repeatable and had consistent trends between data sets; however, the moment data were not repeatable or consistent. Reference data for the model at nominally free-air conditions were obtained in Tunnel 4T, in which the blockage of the model is 0.156 percent. Data with varying amounts of interference were measured in the adaptive-wall test section of Tunnel 1T, in which the blockage is 2.5 percent. In the adaptive-wall configuration, the 1-ft-sq test section has 60-deg inclined-hole perforated walls which have been segmented to provide variably distributed porosity for adaptive-wall control as detailed in Refs. 3 and 4. The conditions at which data were obtained for the WIAC code evaluation are shown in Table 1. These data were obtained with uniform wall porosity except as noted.

Flow-field data were obtained in Tunnel 1T by the interface measurement system shown in Fig. 2. This system is comprised of a pair of two-component static pipes that can be positioned to any desired azimuth about the test article. The pipe measurements are used to infer the axial distributions of the static pressure, $C_{p_I}(x)$, and the longitudinal derivative of the velocity component normal to the cylindrical surface defined by the rotating pipes, $\partial v_n(x)/\partial x$. A data reduction procedure for these two quantities is derived in Refs. 7 and 8 using slender body theory for a cylinder in nonuniform flow. The distribution of static pressure

at the centerline of the pipe is determined by averaging the upper and lower pressure measurements on the pipe as

$$C_{p_I}(x) = \frac{C_{p_\ell}(x) + C_{p_u}(x)}{2} \tag{1}$$

and the distribution for the derivative of normal velocity is proportional to the difference of the upper and lower pressure measurements on the pipe as

$$\frac{\partial v_n(x)}{\partial x} = \frac{C_{p_\ell}(x) - C_{p_u}(x)}{8r} \tag{2}$$

where r is the radius of the pipe.

The current data base contains model data taken only in the pitch plane, and lateral symmetry is assumed for the WIAC calculations. To enhance data quality, however, measurements were obtained with both pipes at laterally symmetric locations and averaged to overcome alignment bias errors.

3.0 WIAC PROCEDURES

Two basic transonic WIAC procedures have been evaluated at AEDC and are distinguished by the number of interface variables required to be measured near the tunnel boundary. The procedures are designated as the single-measured-variable (SMV) procedure and the two-measured-variable (TMV) procedure. Smith, in Ref. 9, classifies these procedures as Schwarz-type and Cauchy-type, respectively, based on the mathematical statement of the boundary condition. Codes for the procedures have been developed, investigated by numerical simulation (Ref. 2), and, in this report, are evaluated using experimental data. The procedures that have been developed and evaluated in the current effort emphasize wall interference corrections to the data rather than qualitative assessments of wall interference.

Two types of corrections for either the SMV and TMV procedures can be applied to wind tunnel data. Global corrections increment the tunnel conditions of Mach number and angle of attack to determine equivalent free-air conditions for the data obtained in the tunnel. For this type of correction, it is assumed that the interference effect is uniform in nature and that some corresponding free-air conditions exist for the measured data. The other type of correction is a local correction, or increment, to the surface pressure on or near the model. The increments to the pressure distribution can be integrated over the surface to determine corrections to the force and moment data.

The advantages of the local corrections over the global corrections are the ability to account for longitudinal and lateral gradients in interference effects and to correct data at the specified test condition. The advantage of the global corrections over the local corrections is that the matching process can alleviate the large local increments in the region of the shock.

The procedures are independent of the flow solver so that solution of the tunnel and free-air flows can be performed using any appropriate solver. The solvers used in the evaluation, as well as their advantages and disadvantages, will be discussed in Section 4.0.

3.1 SINGLE-MEASURED-VARIABLE PROCEDURES

The SMV procedures generally use measured pressure at the interface. The concept of using measured interface data is used for 2-D, nonlinear transonic flows in Refs. 10 and 11. The 2-D procedures assumed model pressures are obtained and an inverse problem is solved to determine an effective shape of the model. The effective shape implicitly includes viscous effects on the model, even though inviscid flow solvers are used to determine the corrections. The 2-D procedures are classified as matching procedures by Smith (Ref. 9). For 3-D testing, model pressure distributions are not generally obtained, and the measured interface-pressure data must be supplemented by knowledge of the model geometry. Therefore, any simulation of viscous effects has to be generated by the flow solver.

The SMV procedure developed and implemented at AEDC is illustrated in Fig. 3. If local corrections are to be determined, only two flow-field calculations are required. The first is a tunnel calculation with the interface pressures specified, and the second is a free-air calculation. Both calculations are performed at the experimental tunnel conditions (M_E, α_E) and with model geometry, or hard geometry, specified. The local increments of interference on the model are defined by

$$\Delta C_p = C_{p_\infty} - C_{p_T} \tag{3}$$

If experimental model pressures, $C_{p_{mE}}$, are obtained, the local corrections, ΔC_p, are added to obtain a corrected model pressure distribution, $C_{p_{mc}}$. The experimental lift is corrected by integrating the distribution of ΔC_p.

If global corrections are to be determined, an iterative process is required to adjust the flow conditions (M_∞, α_∞) until the differences between model surface pressures calculated in the tunnel and in free air are minimized. Once the minimization has been obtained and the difference is within a given tolerance, the new flow conditions (M_∞, α_∞) are considered the equivalent free-air conditions for the tunnel data. If the minimization does not yield a

difference within the given tolerance, no equivalent free-air conditions are considered to exist for the tunnel data, and the data are uncorrectable.

Special attention is necessary when the model pressure distributions are compared at the adjusted free-stream Mach number so that a consistent comparison can be made with the tunnel solution. The basis for comparison used here is matching model surface pressure distributions in dimensional form with the assumption that the stagnation pressure is the same in both the tunnel and the equivalent free-air flow fields. This is essentially what is done in Ref. 10 to compare pressure distributions.

Another SMV procedure that was evaluated at AEDC is the TUNCOR code that is discussed in Refs. 12 and 13. The TUNCOR code was developed by Flow Research with funding by NASA Langley Research Center and AEDC. The basic TUNCOR scheme provides global corrections to Mach number and angle of attack. Lift and pitching moment, pressure measurements near the tunnel wall, and model shape are required. The correction procedure may be divided into two steps. First, the flow about the model is computed by using the measured interface pressures as boundary conditions. In this step, the wing and tail angles of attack, $\alpha_{T,w}$ and $\alpha_{T,t}$, respectively, are determined such that the calculated lift and pitching moment are equal to the experimental lift and pitching moment. The angles of attack will generally be different from the experimental values, $\alpha_{E,w}$ and $\alpha_{E,t}$, because of viscous effects present in the experiment as well as geometrical differences between the test model and the computational representation. In the second step, the flow about the model in free air is computed. Angle-of-attack and Mach number corrections are determined such that the calculated model lift and pitching moment match the experimental values, and the calculated Mach number difference on the model surface in the tunnel and free air is minimized. A summary of the correction procedure is given in Fig. 4.

Numerical investigation of the TUNCOR code at AEDC suggested several refinements. One necessary refinement was a conversion of the code to cylindrical coordinates to accommodate the pressure measurements that are made on the cylindrical interface in Tunnel 1T. This modification is summarized in Ref. 13. Additional modifications that have been implemented are (1) defining a global angle-of-attack correction instead of independent corrections to wing and tail angles of attack, (2) including the body lift in the total lift, and (3) determining local pressure corrections as an alternative to global corrections to Mach number and angle of attack. Results have been obtained with TUNCOR and compared to the other codes developed and are discussed in Section 5.0.

3.2 TWO-MEASURED-VARIABLE PROCEDURES

In an SMV procedure, any simulation of the viscous effects on the model must be provided by the flow solver. In contrast, by using both measured variables at the interface, it is possible to eliminate the need for representation of the model and the viscous effects, at least for subsonic, linear flows (Refs. 14 and 15). With the second-measured variable, an effective shape of the model can be determined that is similar to the effective shape determined by the 2-D methods of Refs. 10 and 11.

For subsonic flow, where Prandtl-Glauert theory can be used, the wall interference can be determined directly from the two-measured variables without an explicit determination of the effective shape. This has been shown in Refs. 14 and 15 for 2-D subsonic flow and has also been extended at AEDC to subsonic flow for 3-D wings.

For nonlinear, transonic flow, however, it is necessary to define an effective shape from the two-measured variables. In principle, one can define an arbitrary reference surface surrounding the model and, using the measured pressure at the interface, iteratively determine the normal velocity distribution on that reference surface that is compatible with the other-measured variable at the interface (Ref. 16). The normal velocity distribution on the reference surface or effective shape can then be used in a free-air calculation. A comparison of effective shape pressure distributions in the tunnel and in free air then defines the wall interference.

A transonic TMV procedure has been developed at AEDC and is shown by the block diagram in Fig. 5. The TMV procedure is similar to the SMV procedure except for the determination of the effective shape. The process for determining the effective shape does not use the arbitrary reference surface, but rather starts with the test model geometric shape and then adjusts the shape to match the measured interface distribution of $\partial v_n/\partial x$ while continuing to impose the interface distribution of pressure. The process is accomplished by adding mode shapes, such as a constant, a linear distribution, or square root distribution to the model geometric shape, until the match is obtained on $\partial v_n/\partial x$ at the interface. The approach is equivalent to the general approach mentioned above with the reference surface collapsed to the model surface. Like the SMV procedures described earlier, the TMV procedure requires the model shape. However, the determination of the effective shape includes an approximation of the viscous effects.

4.0 CODES AND FLOW SOLVERS

The procedures described in the previous section are independent of the flow-field equations and algorithm or flow solver used to solve the tunnel and free-air flows. In the current evaluation, two flow-field equations were employed, the transonic small disturbance (TSD)

equation and the Euler equations. Other flow solvers could be incorporated into the procedures, depending on the amount of computational accuracy required in the simulation of the tunnel and free-air flows.

The TSD equation used in the AEDC SMV and TMV procedures for both global and local corrections is given in Refs. 3 and 4. The TSD equation used in the TUNCOR SMV procedure is the same equation with some additional cross-flow derivatives and is given in Ref. 13. Both forms of the equation are solved using the Murman line-relaxation solver described in Ref. 17.

The TSD solver has the advantage of being computationally inexpensive, which is desirable for routine application. However, it also has basic shortcomings, namely, the lack of physics to prescribe model boundary conditions accurately and the lack of adequate grid resolution in the global mesh system where grid spacing is constrained by the wing and tail sweep. These shortcomings will be discussed in detail in Section 5.0. Another limitation of the TSD solver is that it can only handle simple geometric models and must be extensively modified to simulate more general configurations.

The Chimera domain decomposition technique, (Refs. 5 and 18), has been routinely applied for wall interference prediction using the Euler equations. It has been modified for use as a WIAC tool by incorporating an interface pressure boundary condition (Ref. 19) and employed in the AEDC SMV procedure for local corrections. The Euler solver with the Chimera domain decomposition technique offers some significant advantages over the TSD solver. Grid-resolution difficulties are solved by the Chimera domain decomposition technique; specification of model boundary condition is improved by a body-conforming grid; and more general configurations can be represented without major modifications other than new grid generation. A disadvantage is the additional computational resources required to perform these calculations. However, recent improvements have been incorporated into the code at AEDC that have significantly reduced computational resources. Additional improvements to reduce computational times are being investigated. The Chimera approach has the additional capability of using a thin-layer Navier-Stokes solver.

5.0 RESULTS AND DISCUSSION

Numerical verification of the WIAC codes investigated at AEDC is reported in Refs. 2 and 12. Experimental evaluation of the codes using the data base obtained in Tunnel 1T and reference data from Tunnel 4T is presented herein.

5.1 TUNCOR SMV PROCEDURE

The TUNCOR and the AEDC SMV-TSD codes gave similar results in numerical verification studies. Global and local corrections were obtained with the TUNCOR code for a limited number of experimental cases and compared with corresponding results obtained for the AEDC SMV-TSD code. These comparisons will be discussed further in Section 5.4. Good agreement between the corrected lift using the TUNCOR and AEDC SMV-TSD codes was obtained in all cases.

As discussed in Section 3.1, the pitching moment is an integral part of the TUNCOR correction procedure. The crude model force and moment instrumentation (Section 2.0) compromised the accuracy of the measurement of pitching moment. The TUNCOR code requires more computational resources, for comparable grids, than the more streamlined AEDC procedures and solver. Since TUNCOR gave results similar to the AEDC SMV-TSD code, required the use of inaccurate pitching-moment data, and required more computational resources, most of the experimental evaluation was performed with the AEDC SMV-TSD and TMV-TSD procedures. The AEDC procedures will be referred to simply as the SMV-TSD and TMV-TSD procedures for the remainder of the report.

5.2 CATEGORIZATION OF RESULTS

The wall interference data cases listed in Table 1 can be separated naturally into two categories, those at $M_E \leq 0.80$ that have subcritical or mildly supercritical flow over the model, and those at $M_E \geq 0.90$ that have strongly supercritical flow over the model and at the interface in the vicinity of the wing tip. There are no Tunnel 4T reference data available in the M_E interval between 0.80 and 0.90, so a clear dividing Mach number cannot be ascertained. In each category, specific nonlifting and lifting cases will be discussed as representative. General, but less detailed results will be given for all of the cases. All of the results for subcritical and mildly supercritical flow in Section 5.3 were obtained using the TSD flow solver exclusively in both SMV and TMV procedures. For strongly supercritical flow (Section 5.4), the Euler flow solver was used in both the SMV and pretest prediction procedures in addition to the TSD solver in the SMV procedure.

5.3 SUBCRITICAL AND MILDLY SUPERCRITICAL FLOW

Eleven cases in Table 1 fall into the mildly supercritical or subcritical flow category. Three are nonlifting, and the mildly supercritical flow case $M_E = 0.80$, $\alpha_E = 0$ deg, and porosity, τ, of 2 percent has been chosen as representative. The case of $M_E = 0.80$, $\alpha_E = 6$ deg, $\tau = 2$ percent, has been chosen as representative of the eight lifting configurations.

5.3.1 SMV-TSD Nonlifting Cases

Since the AEDC wall interference model in Fig. 1 is vertically symmetrical about its centerline, results for $\alpha_E = 0$ deg should display symmetry. The interface data are mildly asymmetrical above and below the model centerline, but no consistent trends were observed. A method of correcting for the asymmetry is to average the interface measurements at equivalent locations above and below the model. Preliminary interference calculations indicated that both local and global corrections were essentially the same whether or not the correction for asymmetry was applied to the data. All the nonlifting cases reported herein used interface data averaged for vertical symmetry except as noted.

Results of SMV-TSD calculations at $M_E = 0.80$, $\alpha_E = 0$ deg, and $\tau = 2$ percent for measured data obtained at the empty tunnel calibration values of P_C/P_T, the ratio of plenum pressure to stagnation pressure, will be described first with emphasis on local corrections at M_E. Figure 6 contains comparisons of the measured and calculated distributions of model pressures, C_{p_m}, in the tunnel and in free air at M_E. Representative model stations have been selected, namely 60 percent of the semispan on the wing and tail and on the upper surface of the fuselage in the lateral plane of symmetry (see Fig. 1). The fidelity of the calculated C_{p_m} on the wing is reasonably satisfactory over the aft part of the chord, as shown in Fig. 6a, but does not resolve the flow adequately near the leading edge and the suction peak. The critical value of C_p at $M_E = 0.80$ is approximately -0.43 so that the measured data are supercritical, whereas the calculations remain subcritical. The overall fidelity of the calculated C_{p_m} distribution on the tail shown in Fig. 6b is poor, but the fidelity shown on the fuselage in Fig. 6c is satisfactory except in the vicinity of the wing (near $x/L = 0.5$) and the tail (near $x/L = 0.85$).

The interference in this case is relatively small but has a gradient in the x direction that can be observed most easily on the fuselage (shown in Fig. 6c). However, the fidelity of the corrections, not the fidelity of the calculated tunnel and free-air C_{p_m} distributions, is the principal issue. The measured and computed distributions of ΔC_p for this case are given in Fig. 7. The corrections are small and match the measured differences reasonably well, particularly on the tail and fuselage.

5.3.2 SMV-TSD Lifting Cases

The representative mildly supercritical lifting configuration in Table 1 selected for presentation is $M_E = 0.80$, $\alpha_E = 6$ deg, and $\tau = 2$ percent with the empty-tunnel calibration value of P_C/P_T. Local corrections will be emphasized again so that the results are at the nominal test Mach number. Figure 8 contains comparisons of the C_{p_m} distributions at the

same model locations as in Fig. 6. Both tunnel and free-air calculations were made at α_E = 6 deg. The fidelity of the wing C_{p_m} calculations shown in Fig. 8a is even less satisfactory than it was at 0 deg in Fig. 6a. The C_{p_m} distribution on the entire upper surface of the wing in front of the shock wave location is not predicted well, although the region aft of the shock and the entire lower surface are reasonably satisfactory. The tail C_{p_m} fidelity shown in Fig. 8b also is unsatisfactory and does not reproduce the measured supercritical flow at the suction peak. The fuselage C_{p_m} fidelity presented in Fig. 8c is fair and displays the longitudinal gradient of interference.

The corresponding local ΔC_p corrections are plotted in Fig. 9. The fidelity of the wing ΔC_p corrections shown in Fig. 9a is not outstanding, but the tail fidelity on both the upper and lower surfaces shown in Fig. 9b is excellent. This occurs despite the poor fidelity of the C_{p_m} distributions observed in Fig. 8b. The ΔC_p corrections on the fuselage, although small, are predicted well including the gradient of interference, as shown in Fig. 9c.

At any spanwise station of the wing and tail, the local correction to the sectional lift coefficient, ΔC_ℓ, based on the local chord, is given by

$$\Delta C_\ell = C_{\ell_\infty} - C_{\ell_T} = \int_0^c [\Delta C_{p_\ell}(x) - \Delta C_{p_u}(x)]dx \tag{4}$$

where the subscripts ℓ and u denote the lower and upper surfaces, respectively. With reference to Fig. 9a for the representative wing section, the integrated ΔC_ℓ from the predicted ΔC_p corrections is less than zero, the same as is indicated by the measured ΔC_p. Both the integrated ΔC_ℓ and measured ΔC_p corrections are consistent in sign with the overall ΔC_L measured by the sting support strain gages, and will be discussed next.

Overall $\Delta C_{L_c}(\alpha_E)$ corrections were calculated by suitable integrations over the computational grid on the surfaces of the wing, body, and tail. The measured Tunnels 1T and 4T lift-curve slopes are nearly constant over the α interval from 0 to 6 deg. The curves for the Tunnels 1T and 4T data presented in Fig. 10 for M_E = 0.80 are broken for convenience of scale to show details of the corrections more clearly. Results are shown for both τ = 2 and 5 percent, as well as corrections, $\Delta C_{L_c}(\alpha_T)$, based on matching the calculated and measured C_L in Tunnel 1T by adjusting the angle of attack of the entire configuration to the value α_T. The latter corrections will be discussed later in this section. The data shown in Fig. 10, corrected according to calculation at α_E, are close to the Tunnel 4T values despite the relative crudeness of the TSD calculations. The comparison in Fig. 10 is representative of all subcritical and mildly supercritical cases, as summarized in Table 2. The main exception is the high lift case, M_E = 0.60, α_E = 10 deg, and τ = 5 percent where the sign of $\Delta C_{L_c}(\alpha_E)$ differs from ΔC_{L_E}, although the overall magnitude of the discrepancy is not out of line with those at τ = 2 and 7 percent at the same Mach number and angle of attack.

A global correction is shown in Fig. 10 at $\alpha_E = 2$ deg and $\tau = 2$ percent. The lift is not constrained in the AEDC SMV-TSD procedure, in contrast to TUNCOR. Therefore, in addition to a Mach number correction, $\Delta M = 0.009$, and an angle-of-attack correction, $\Delta\alpha = -0.03$ deg, there also is a lift correction, $\Delta C_L = -0.005$, as interpreted at the adjusted Mach number. Approximate adjustment of the Tunnel 4T data by the Prandtl-Glauert rule from $M_E = 0.800$ to $M_\infty = 0.809$ is such as to increase the measured C_L at $\alpha_E = 2$ deg by 0.003. Consequently, the global correction and local correction correspond very closely. Other global corrections gave similar results at a variety of flow conditions.

The SMV procedure was modified to mimic TUNCOR more closely. While continuing to prescribe the C_{p_I} distribution measured at α_E, the model angle of attack was adjusted to a value α_T, which resulted in agreement between the calculated and measured lift in Tunnel 1T. The free-air solution also was calculated at α_T so that local corrections could be found. These results are plotted in Fig. 10 and listed in Table 2. The SMV-TSD code underpredicts the lift in all cases at α_E, and the adjusted angles, α_T, in Table 2 run between 1.5 and 1.7 times α_E. Generally, it would be expected that the inviscid lift prediction at α_E would be greater than measured, but the typical lack of fidelity in the predicted C_{p_m} distributions, as shown in Fig. 8, leads to the discrepancy. In every case in Table 2 except $M_E = 0.65$, $\alpha_E = 4$ deg, and $\tau = 5$ percent, $\Delta C_{L_c}(\alpha_T)$ is farther from ΔC_{L_E} than $\Delta C_{L_c}(\alpha_E)$. In many cases the sign of the correction has reversed.

The detailed nature of a matched Tunnel 1T lift example is examined for the same representative case of $M_E = 0.80$, $\alpha_E = 6$ deg, and $\tau = 2$ percent, but here with $\alpha_T = 9.5$ deg. The C_{p_m} distributions on the representative wing section are given in Fig. 11 for comparison with Fig. 8a. The larger α_T leads to better C_{p_m} fidelity on the upper surface up to the shock wave location. However, C_{p_m} fidelity on the upper surface downstream of the shock and on the entire lower surface is worse. The corresponding ΔC_p distributions are presented in Fig. 12 together with the $\alpha_E = 6$ deg results from Fig. 9a for ease of comparison. The sign reversal in $\Delta C_{L_c}(\alpha_T)$ (See Fig. 10 and Table 2) is evident in the reversed sense of the predicted ΔC_{p_ℓ} and ΔC_{p_u}, which integrate to give $\Delta C_\ell > 0$.

The tail results for C_{p_m} and ΔC_p, although not shown, are roughly the same as seen in Figs. 8b and 9b, which follows, apparently, from the increase in downwash at the tail caused by the wing as the wing lift increases. The increased downwash at the tail counters the increase in the tail angle of attack. For all of the subcritical and mildly supercritical flow lifting cases, the tail lift is very small and does not change appreciably with angle of attack. It must be emphasized, though, that even small changes in tail lift can have a major effect on pitching moment because of the large moment arm. The absence of reliable pitching-moment data prevents comparisons. Finally, the fuselage C_{p_m} and ΔC_p results calculated at α_T are similar to those shown in Figs. 8c and 9c, except that the fidelity of both is much worse in the immediate vicinity of the wing.

5.3.3 SMV-TSD Grid Refinement

It was mentioned in Section 4.0 that the cylindrical coordinate system used in the SMV-TSD and TMV-TSD flow solvers requires a computational grid spacing that is uniform in the x direction to account for wing and tail sweep. This grid constraint removes the possibility of refining the grid distribution just in the vicinity of the leading edge where large gradients exist in the flow. However, in a series of calculations the basic x spacing was halved and then halved again. Remarkably, the fidelity in the vicinity of the wing and tail leading edges did not improve greatly and the resulting calculated ΔC_p and ΔC_L corrections were virtually unchanged. Similar calculations for a strongly supercritical case also showed no significant improvement in predicted C_{p_m} fidelity, although there was some shock relocation. Therefore, the lack of fidelity may be related more to deficiencies in prescribing boundary conditions near the wing and tail leading edges in the TSD solver than to grid resolution.

5.3.4 TMV-TSD Investigation

A TMV-TSD investigation was carried out for some nonlifting cases. Small magnitude changes in wing surface shape were introduced to represent the estimated growth of the boundary layer. Negligible changes were observed in the calculated $\partial v_n/\partial x$ distributions at the interface and in the calculated C_{p_m} and ΔC_p distributions on the wing surfaces. In addition, a 2-D, direct, integral boundary-layer calculation procedure (Ref. 20) was introduced into a stripwise, weak-interaction method to estimate the viscous effects on the model. In this procedure, too, there were negligible changes in the ΔC_p corrections on the model surface. Accordingly, large magnitude changes in wing section shape were introduced by means of the TMV-TSD procedure, particularly near the leading edge. The resulting effective shapes did improve the fidelity of the calculated wing C_{p_m} distributions, but these improvements did not correlate well with the agreement between measured and calculated $\partial v_n/\partial x$ at the interface. Furthermore, the resulting ΔC_p corrections did not change greatly, so no real improvement could be achieved.

Investigation of the TMV-TSD procedure for the lifting cases led to the same difficulties. Inasmuch as small shape changes to represent the boundary-layer growth had proved inadequate, large changes in model shape were necessary to match both interface measurements and so improve C_{p_m} fidelity on the model. All of the results indicate the requirements for a research effort to solve a design problem for model effective shapes based solely on two independent measurements at the interface. Furthermore, it is not clear whether such a problem is posed properly mathematically, as discussed in Ref. 16. Consequently, further TMV development was postponed beyond the duration of the investigation reported here.

5.3.5 Summary of Subcritical and Mildly Supercritical Flow Results

Nonlifting interference is small for subcritical and mildly supercritical flow, although there are measurable gradients of interference in the longitudinal direction. Local SMV-TSD correction procedures appear to do a reasonable job of predicting the ΔC_p corrections, including the gradients.

The interference is greater for lifting cases. The local and global SMV-TSD correction procedures calculated at the test angle of attack, α_E, assess the sign of the lift-interference errors properly, but do not predict correction magnitudes adequately. However, the trend of the longitudinal gradients of interference seems to be predicted reasonably well. Lift corrections are totally unsatisfactory when applied at the angle of attack, α_T, that has been adjusted to match the calculated lift with the lift measured in the tunnel test.

Refinement of the longitudinal spacing in the computational grid for the TSD flow solver by halving it and then halving it again did not affect the fidelity of the calculated model pressure distributions and corrections significantly. The lack of fidelity appears to be related more to deficiencies in the TSD solver for treating the boundary conditions near the rounded leading edges of the lifting surfaces than to grid resolution. Development of TMV procedures is more difficult than originally anticipated and was postponed at an early stage of the investigation.

5.4 STRONGLY SUPERCRITICAL FLOW

Table 1 includes 18 strongly supercritical conditions from the WIAC tests. All of the data were obtained using the empty-tunnel calibration value of P_C/P_T for the given Mach number and porosity. In addition, Table 1 lists two test conditions from the adaptive-wall experiments. Data at these conditions are available for several adaptive-wall iterative steps.

A summary of the overall ΔC_L corrections for all 13 lifting cases in Table 1, as calculated with the SMV-TSD procedure, is given in Table 3. Plots of C_L for the Tunnel 1T data, the corrected Tunnel 1T data, and the Tunnel 4T reference data at $M_E = 0.90$, $\alpha_E = 2$ and 4 deg, and $\tau = 2$, 5, and 7 percent are given in Fig. 13. The broken form is used again to show the details, even though the C_L versus α slopes are not constant in this regime. The results in the table and figure are unsatisfactory in most cases. The sign of $\Delta C_{L_c}(\alpha_E)$ is predicted incorrectly in every case except two, and the magnitude is greatly in error for one of them. At $M_E = 0.90$, $\alpha_E = 4$ deg, and $\tau = 2$, 3 and 7 percent, the angle of attack of the entire configuration was adjusted to α_T values of 4.8, 4.6, and 4.8 deg, respectively, so that the measured lift is matched in each case. Also, the example $M_E = 0.9$, $\alpha_E = 2$ deg, and $\tau = 2$ percent was adjusted to $\alpha_T = 2.5$ deg. The overall results shown in Table 3 and

Fig. 13 are in even worse agreement than at α_E, which is consistent with the experience in the mildly supercritical cases. There is every indication that the α_T adjustment procedure would exacerbate the already unsatisfactory lift corrections in the remaining cases. TUNCOR results are included in Fig. 13 for the $M_E = 0.90$, $\alpha_E = 2$ deg, and $\tau = 2$ percent case. Both local and global TUNCOR corrections are consistent with each other and with the SMV-TSD local correction at $\alpha_T = 2.5$ deg. TUNCOR results at $\tau = 5$ and 7 percent are similar, but not shown.

The lift correction results shown in Table 3 demonstrated that the TSD-based correction procedures are inadequate in their present form, independent of whether local or global corrections are considered. As discussed in the previous section, the subcritical and mildly supercritical results are not entirely satisfactory, either. It was not clear whether the fault lay with aspects of the TSD approximation, particularly inadequate treatment of the leading edge region, or with the inviscid assumption that can affect shock wave location and strength significantly. The availability of the Chimera domain decomposition method and the fact that corresponding body-conforming computational grids already had been generated for the wall-interference model led to the decision to perform two series of benchmark calculations to examine these questions. The first series, which is reported herein, used the Euler solver capability in the Chimera method to examine the TSD approximations to the Euler equations. The second series, which will be reported later, will use the thin-layer Navier-Stokes solver capability that also is resident in the Chimera method to examine the effects of viscosity.

Euler solutions have been applied in the sense of local corrections, ΔC_p, and, by integration over the model surfaces, ΔC_L at the test Mach number. Solutions have been obtained at α_E and by adjusting to α_T for both the WIAC SMV procedure prescribing the measured C_{p_I} distribution at the interface and the AEDC pretest prediction procedure using Jacocks' semi-empirical, local perforated wall boundary condition (Ref. 2). The cases selected for comparing the TSD and Euler solvers are those for which the C_{p_I} distribution at the interface is very close to zero far upstream. This was necessary because the Euler solutions with the pretest prediction procedure typically yield $C_{p_I} \approx 0$ upstream, and comparisons of predicted and measured C_{p_I} were desired. It should be emphasized, however, that the WIAC SMV procedures with measured interface pressure distributions as boundary conditions, for TSD or Euler solvers, can handle arbitrary upstream values of C_{p_I}. The adaptive-wall data are particularly useful because suitable data with $C_{p_I} \approx 0$ exist at various iterative steps. In addition, Euler solutions were obtained for the $M_E = 0.90$, $\alpha_E = 4$ deg, and $\tau = 7$ percent case since the calibration plenum pressure ratio, P_C/P_T, led to $C_{p_I} \approx 0$ upstream.

The following discussion will concentrate on the representative nonlifting case $M_E = 0.90$, $\alpha_E = 0$ deg, and $\tau = 3$ percent and lifting case $M_E = 0.90$, $\alpha_E = 4$ deg, and $\tau = 3$ percent from the adaptive-wall experiments. These cases are chosen because they served

as the basis for the Euler solver investigation using the Chimera domain decomposition technique, both in the SMV and pretest prediction procedures.

5.4.1 Nonlifting Cases

Local correction results using the SMV-TSD procedure were obtained for $M_E = 0.90$, $\alpha_E = 0$ deg, and $\tau = 3$ percent and will be presented first. Figure 14 contains comparisons of the measured and calculated C_{p_m} distributions. The fidelity of the calculated C_{p_m} distribution on the wing, as shown in Fig. 14a, is poor with a failure to resolve the flow near the leading edges and peak suction regions just as in the mildly supercritical case shown in Fig. 6a. The overall fidelity of the calculated C_{p_m} distributions on the tail, Fig. 14b, is considerably better than on the wing as is the C_{p_m} fidelity on the fuselage, Fig. 14c. The corresponding distributions of the ΔC_p corrections are plotted in Fig. 15. Although the signs of the predicted ΔC_p generally are correct, the magnitudes are not, especially in the vicinity of the shock waves.

The longitudinal gradient of the interference can be seen most clearly on the fuselage C_{p_m} and ΔC_p distributions in Figs. 14c and 15c, respectively. SMV-TSD calculations for the related case of $M_E = 0.90$, $\alpha_E = 0$ deg, and $\tau = 5$ percent gave global corrections of $\Delta M = 0.000$ if local pressures were matched on the entire configuration, on the wing only or on the body only, but gave $\Delta M = 0.010$ by matching on the tail only. This is another manifestation of the strong longitudinal gradient of interference, and shows the impossibility of global ΔM corrections for reducing interference on the wing and tail simultaneously for strongly supercritical flow.

Local correction results using the SMV procedure with the Euler solver for the same case are presented in Fig. 16 for C_{p_m} and in Fig. 17 for ΔC_p. In Fig. 17, the SMV-TSD results, already presented in Fig. 15, have been added to aid in convenient comparison of the respective results. The vertical symmetry assumption was not made when applying the interface data as boundary conditions. However, the differences between the upper and lower model surfaces are noticeable on the wing only, where they are small and consistent with the measurements shown in Fig. 17a. Compared to the TSD results, the fidelity of the C_{p_m} solutions on the wing is improved significantly in the vicinity of the leading edge and elsewhere upstream of the shock, as can be seen best by comparing the free-air C_{p_m} distributions in Fig. 16a with those of Fig. 14a. The predicted shock wave location is about the same with both flow solvers, but the shock is stronger in the Euler solutions because of the improved C_{p_m} fidelity upstream of the shock, and is seen best in Fig. 17a. The fidelity of the predicted C_{p_m} distributions on the tail and fuselage, particularly near the tail, is improved with the Euler solver. Overall, when the ΔC_p distributions are examined, the Euler results in Fig. 17 are

very similar to the corresponding TSD results, except in the vicinity of the shock waves where the Euler results are significantly better, especially on the wing.

The local correction results found using the Euler solver in the pretest prediction mode with the semi-empirical wall boundary condition representation are almost identical with those from the Euler SMV results shown in Figs. 16 and 17 and will not be shown. The predicted shock location in the tunnel at the 60-percent wing station lies 1 percent of the chord farther aft of the average of the upper and lower surface shock locations in Fig. 16a, whereas on the tail and fuselage the C_{p_m} distributions are in close agreement. The ΔC_p distributions are very close to those in Fig. 17. Overall, then, the pretest predictions for the interference in this example do as well as the posttest WIAC SMV-Euler corrections that use measured interface data. However, the comparison has been limited to a case where the interface $C_{p_I} \approx 0$ upstream. In all three procedures compared here for the nonlifting case, the magnitude of the interference is somewhat underpredicted. That is, the predicted corrections move the Tunnel 1T data in the direction of the Tunnel 4T data, but not by a sufficient amount.

5.4.2 Lifting Cases

The representative lifting case will be examined next. The SMV-TSD local correction results for the $M_E = 0.90$; $\alpha_E = 4$ deg, and $\tau = 3$ percent case are given in Fig. 18 for C_{p_m} and in Fig. 19 for ΔC_p. The overall lift corrections for this example are given in Tables 3 and 4 and in Fig. 20 for all three correction procedures. Table 4 also contains the $\tau = 7$ percent results for this Mach number and angle of attack.

The fidelity of the C_{p_m} distribution calculated on the wing by SMV-TSD, as shown in Fig. 18a, is unsatisfactory as expected from all previous results. The predicted shocks in the tunnel and free air are located too far aft on the wing and are too strong, as also can be seen in Fig. 19a. However, the magnitude of the shift in shock location between tunnel and free air is predicted well. As described previously, the ΔC_p distributions can be integrated over the chord to yield local sectional lift coefficient increments ΔC_ℓ. Such an integration of the measured ΔC_p data in Fig. 19a would give $\Delta C_\ell < 0$, which is consistent with the measured overall model ΔC_L in Tables 3 and 4 and Fig. 20. Conversely, integration of the calculated ΔC_p distribution would give $\Delta C_\ell > 0$, which is consistent with the predicted ΔC_L but is contrary to the measured value. The fidelity of the predicted tail C_{p_m} distribution in Fig. 18b is very poor; in fact, in contrast to the measurements, the predicted tail lift is less than zero. The mismatch at the tail occurs, apparently, because the downwash attributable to the wing lift is overpredicted in the TSD procedure. Nevertheless, the fidelity of the predicted ΔC_p on the tail in Fig. 19b is better than expected. Figures 18c and 19c for C_{p_m} and ΔC_p on the body display the gradient of interference along the body length, with ΔC_p changing sign aft of the wing shock. The test $\alpha_E = 4$ deg was increased to $\alpha_T = 4.6$ deg to match

predicted and measured lift in Tunnel 1T. The resulting ΔC_L shown in Tables 3 and 4 and Fig. 20 corrects the Tunnel 1T data even further beyond the Tunnel 4T data, just as has been found for all of the TSD results.

The WIAC SMV local correction results found using the Euler solver are given in Fig. 21 for the C_{p_m} distributions. In this case, C_{p_m} distributions are presented at all three spanwise wing positions to complement the results at the representative 60-percent station. The distributions of the ΔC_p corrections, but at only the 60-percent wing station and the tail and fuselage stations, are plotted in Fig. 22 along with the SMV-TSD results from Fig. 19. The predicted C_{p_m} distribution fidelity at the wing stations in Figs. 21a-c is fair except for the shock wave locations and strengths, which unfortunately, dominate the entire distributions. This is especially pronounced at the 90-percent wing station where the measured compression is much farther forward and gradual than the predicted strong shocks. The ΔC_p distribution at the 60-percent wing station in Fig. 22a is remarkably similar to the TSD result in the immediate vicinity of the shock, although it is much smoother and more accurate upstream and downstream of the shock. The ΔC_p results for the 40- and 90-percent stations, although not shown, have similar behavior. The ΔC_ℓ correction found by integrating the calculated ΔC_p distribution in Fig. 22a again would be greater than zero, but probably less than for the TSD counterpart, as reflected by the calculated ΔC_L in Tables 3 and 4 and Fig. 20. It is interesting to note that in the nonlifting results in Fig. 17a, the ΔC_p peak is underpredicted, whereas in the lifting case in Fig. 22a, the ΔC_p peak is greatly overpredicted. The predicted tail C_{p_m} distribution in Fig. 21d is far superior to the TSD result in Fig. 18b because the predicted tail lift is greater than zero, as the measurements indicate. The predicted ΔC_p shown in Fig. 22b for the tail is improved from the TSD result. The predicted body C_{p_m} and ΔC_p in Figs. 21e and 22c are qualitatively similar, but quantitatively superior, to the TSD results. Despite the overall improvements in fidelity, the calculated overall model ΔC_L shown in Table 4 and Fig. 20 is similar to its TSD counterpart. The measured lift in Tunnel 1T was matched by reducing α_E from 4 deg to α_T = 3.3 deg in the SMV-Euler procedure. Although the computed ΔC_L increment is smaller, it is still of the wrong sign and so is inadequate, as displayed by the corrected C_L in Table 4 and Fig. 20.

The local correction results found using the Euler solver in the pretest prediction mode are examined next. The C_{p_m} distributions for the tunnel solutions are very close to those in Fig. 21 for the WIAC SMV-Euler solutions and have been presented in Ref. 5. They will not be presented here because the only noticeable difference is wing shock positions of about 2 percent of the chord closer to the free-air shock positions than the SMV-Euler results. The corresponding ΔC_p distributions are presented in Fig. 23 along with the SMV-Euler results from Fig. 22. At the 60-percent wing station, Fig. 23a, the predicted ΔC_p is very close to that in the SMV-Euler case except for the reduced peak value that follows because the shocks are closer together. The ΔC_ℓ correction found by integrating the ΔC_p distribution from this

solution will be reduced in magnitude greatly from both WIAC SMV results because of the lower peak. The reduced magnitude is reflected in the overall predicted model ΔC_L correction which, as shown in Table 4 and Fig. 20, is of the correct sign with respect to the measurements, but is not correct in magnitude. The predicted ΔC_p on the tail, Fig. 23b, is somewhat different in character from the SMV-Euler result, and it is not clear which matches the measurements better. The predicted body ΔC_p, Fig. 23c, matches the measurements better than the WIAC SMV-Euler counterpart near the wing and tail. The measured lift in Tunnel 1T was matched by reducing α_E from 4 deg to $\alpha_T = 3.3$ deg, the same as for the SMV-Euler case; but the ΔC_L increment was unchanged to the accuracy listed in Table 4 and plotted in Fig. 20.

5.4.3 Summary of Strongly Supercritical Flow Results

In summary, nonlifting interference in strongly supercritical flow displays a large longitudinal gradient. Thus, a global correction matching the local surface conditions on the entire configuration may reduce or correct for the interference on part of the model, but increase it elsewhere. The effect of wall interference is observed principally in the location of the shock waves on the various model surfaces. The SMV-TSD, SMV-Euler, and pretest-Euler procedures all underpredicted the measured ΔC_p in the vicinity of the shock waves.

In the lifting cases, the SMV-TSD local and global corrections at the test α_E are totally inadequate for assessing even the sign of the lift or angle-of-attack correction, let alone the magnitude. The flow everywhere upstream of the shock waves on the suction surfaces of the wing and tail is not resolved well, and the shocks are located too far aft and are too strong. Adjusting α_E to α_T to match the tunnel lift aggravates the error. Application of the SMV procedure with an Euler solver does not improve the overall situation significantly, although the wing and tail pressure distributions near the leading edge and upstream of the shock wave are resolved much better. Pretest predictions of the flow in the tunnel with an Euler solver do show an improvement in the overall lift correction, but the correction still is not satisfactory. Adjustment from α_E to α_T reduces the error in the SMV-Euler procedure and has negligible effect in the pretest Euler procedure. In all three procedures, the calculations overpredict ΔC_p in the vicinity of the shock waves in contrast to the nonlifting results.

The Euler solver, in both operational procedures, eliminates the approximations in leading edge region resolution and basic formulation that are inherent in the AEDC and TUNCOR TSD solvers. However, the fundamental correction capability has not been improved by the inviscid Euler solver for the strongly supercritical cases. Moreover, the various correction procedures give lift corrections that are so different in magnitude that assessment of the degree of interference present cannot be evaluated reliably for the existing data base. Therefore, benchmark thin-layer Navier-Stokes solutions are being obtained to determine whether proper

accounting for the viscous effects will provide accurate WIAC or pretest corrections in the strongly supercritical flow regime.

5.5 INTERFACE RESULTS

It is now useful to turn attention from the model surface to the interface. Interface data in the adaptive wall experiments in Tunnel 1T were obtained at pipe positions, θ_p, of 15, 45, 65, 85, 95, 115, 135, and 165 deg where θ_p is defined in Fig. 2. For the lifting cases, the data at 15, 85, 95, and 165 deg characterize the flow field near the plane of symmetry just above the lower wall, just below and above the wing tip near the side wall, and near the plane of symmetry just below the upper wall, respectively.

Interface distributions C_{p_I} and $\partial v_n/\partial x$ are presented in Figs. 24 and 25, respectively, for the pretest predictions of the flow in the tunnel using the Euler solver at $M_E = 0.90$, $\alpha_E = 4$ deg, and $\tau = 3$ percent. The C_{p_I} distribution fidelity is fair overall. It has been discussed already that the measured lift in Tunnel 1T was overpredicted for $\alpha_E = 4$ deg and had to be reduced to $\alpha_T = 3.3$ deg. This effect can be observed as well in Figs. 24a and d because the predicted C_{p_I} lies below the experimental data in the vicinity of the wing ($x \approx 8.0$) at $\theta_p = 15$ deg and above it at $\theta_p = 165$ deg, indicating too much induced velocity that can be attributed to lift. The same behavior is not obvious at $\theta_p = 85$ and 95 deg in Figs. 24b and c since the peak C_{p_I} is greatly underpredicted compared to the measurements. Since the critical value of C_{p_I} is approximately -0.19 at $M_E = 0.90$, the measured flow is supercritical at the pipe at $\theta_p = 95$ deg. In the nonlifting case at this Mach number, the measured flow is supercritical at the pipe at $\theta_p = 85$ and 95 deg, so the induced velocity attributable to the lift has resulted in the flow becoming subcritical at $\theta_p = 85$ deg. The predicted $\partial v_n/\partial x$ distributions in Fig. 25 are also in fair agreement with the measurements, except at $\theta_p = 85$ and 95 deg where the local maxima and minima are not predicted accurately.

The SMV-Euler solutions for the flow in the tunnel in this case have the measured C_{p_I} distributions prescribed at the interface and so the C_{p_I} agree with the measurements that are shown in Fig. 24. The $\partial v_n/\partial x$ results at $\theta_p = 15$ and 165 deg cannot be distinguished from those of Fig. 25, so they are not presented. The $\partial v_n/\partial x$ results at $\theta_p = 85$ and 95 deg are presented in Fig. 26, along with the pretest prediction results that have been plotted already in Fig. 25. Prescribing the measured C_{p_I} has led to predicted $\partial v_n/\partial x$ values of much greater magnitude in the vicinity of the local maxima and minima.

Finally, the free-air predictions of the Euler code for this case are of interest from the adaptive-wall point of view. The final iterative step of the adaptive-wall adjustment procedure gave C_{p_I} distributions that are close to zero far upstream so that meaningful interface

comparisons can be made between predictions and measurements over its entire length. The C_{p_I} distributions are compared in Fig. 27, and the agreement is excellent. The qualitative relationship between predictions and measurements at θ_p = 15 and 165 deg is the same as it is in Fig. 24 before adaptation. The peak C_{p_I} is predicted much better at θ_p = 85 and 95 deg than it is in Fig. 24. The predicted and measured C_{p_I} data at θ_p = 15 and 165 deg, both before and after adaptation, are replotted from Figs. 24 and 27 in Fig. 28. The measured data in Fig. 28 show that there are significant changes in the C_{p_I} distributions before and after adaptation. The predictions reflect the changes very well. The $\partial v_n/\partial x$ fidelity shown in Fig. 29 is better than it is in Fig. 25 before adaptation. The changes in the measured $\partial v_n/\partial x$ data during adaptation are not as large as they are for C_{p_I}. This is a manifestation of the adaptive-wall experience that in the high subsonic Mach number range, relatively small changes in interface v_n (and so in $\partial v_n/\partial x$) correspond to amplified changes in C_{p_I}.

6.0 CONCLUDING REMARKS

Extensive local and global wall interference correction calculations have been performed with a single-measured-interface variable, transonic small disturbance solver (SMV-TSD) procedure over a wide range of Mach number, angle-of-attack, and wall porosity conditions for the AEDC wall-interference model. The experimental program was conducted in Tunnel 1T where the model has a 2.5-percent solid blockage ratio. The model was also tested in Tunnel 4T to obtain interference-free reference data. Selected benchmark local interference calculations have been obtained with an Euler solver in both SMV and pretest prediction procedures. The quality of the corrections is dependent upon the degree of supercritical flow over the model. The quality of the results for the AEDC model are different for subcritical and mildly supercritical flow (test Mach number, $M_E \leq 0.80$) and strongly supercritical flow ($M_E \geq 0.90$). The dividing Mach number between the two categories is not clearly defined because there are no interference-free reference data in the M_E range from 0.80 to 0.90.

For nonlifting flows, a longitudinal gradient of interference exists along the model. In subcritical and mildly supercritical flows, the interference can be corrected locally with reasonable confidence using the SMV-TSD procedure. In strongly supercritical flows, the gradient effects are larger, and the interference cannot be corrected with reasonable confidence by the SMV-TSD procedure. The two Euler solver procedures gave improved fidelity over SMV-TSD, but still were not entirely satisfactory.

For lifting cases, the longitudinal gradient of interference is present as well. In subcritical and mildly supercritical flows, the SMV-TSD procedure gave a satisfactory assessment of the sign of the measured lift increment caused by interference, ΔC_{L_E}, when the local corrections were calculated at the test angle of attack, α_E. However, the calculated corrections

do not match the magnitude of ΔC_{L_E} adequately over the entire range of test conditions. Adjusting α_E to values of α_T that match the calculated lift in the tunnel to the measured lift made the correction magnitudes worse. In strongly supercritical flows, all three local correction procedures are inadequate for even assessing the sign of ΔC_{L_E}. Global corrections did not give a better interpretation of the data. The SMV-Euler procedure was clearly superior to SMV-TSD in the overall fidelity of the calculated ΔC_{L_E} for the Euler solvers.

Viscous effects, particularly the shock wave/boundary-layer interaction, must be taken into account to resolve the inadequacies that have been encountered with the inviscid solvers. An efficient way to do this is to obtain thin-layer Navier-Stokes solutions within the framework of both the SMV and pretest procedures using existing computational tools. These viscous solutions will be considered as benchmarks and will be interpreted within the context of the results presented herein and reported. It should not be implied that the full thin-layer Navier-Stokes capability will be required for adequate treatment of the viscous effects in wall interference procedures. Decisions as to the level of viscous approximation that is necessary will be made on the basis of the benchmark results.

REFERENCES

1. Whoric, J. M. and Hobbs, R. W. "Hierarchy of Uncertainty Sources in Transonic Wind Tunnel Testing." Paper Presented at the AGARD Fluid Dynamics Panel Symposium on Aerodynamic Data Accuracy and Quality, Requirements, and Capabilities in Wind Tunnel Testing, Naples, Italy, September-October 1987.

2. Kraft, E. M., Ritter, A., and Laster, M. L. "Advances at AEDC in Treating Transonic Wind Tunnel Wall Interference." Paper Presented at 15th Congress, International Council of the Aeronautical Sciences, London, United Kingdom, September 1986.

3. Parker, R. L., Jr. and Erickson, J. C., Jr. "Development of a Three-Dimensional Adaptive Wall Test Section with Perforated Wall." AGARD CP-335, May 1982.

4. Parker, R. L., Jr. and Erickson, J. C., Jr. "Status of Three-Dimensional Adaptive-Wall Test Section Development at AEDC." AIAA Paper 84-0624, Presented at the AIAA 13th Aerodynamic Testing Conference, San Diego, CA, March 5-7, 1984.

5. Donegan, T. L., Benek, J. A., and Erickson, J. C., Jr. "Calculation of Transonic Wall Interference." AIAA Paper No. 87-1432, Presented at the AIAA 19th Fluid Dynamics, Plasma Dynamics, and Laser Conference, Honolulu, HI, June 8-10, 1987.

6. Newman, P. A. and Barnwell, R. W., Editors. "Wind Tunnel Wall Interference Assessment/Correction." NASA CP-2319, January 1983.

7. Nenni, J. P., Erickson, J. C., Jr., and Wittliff, C. E. "Measurement of Small Normal Velocity Components in Subsonic Flows by Use of a Static Pipe." *AIAA Journal*, Vol. 20, No. 8, August 1982, pp. 1077-1083.

8. Erickson, J. C., Jr., Wittliff, C. E., and Daughtry, D. C. "Further Investigations of Adaptive-Wall Wind Tunnels." AEDC-TR-80-34 (AD-A091774), October 1980.

9. Smith, J. "Measured Boundary Condition Methods for 2D Flow." AGARD CP-335, May 1982.

10. Kemp, W. B., Jr. "TWINTN4: A Program for Transonic Four Wall Interference Assessment in Two-Dimensional Wind Tunnels." NASA-CR-3777, 1984.

11. Murman, E. M. "A Correction Method for Transonic Wind Tunnel Wall Interference." AIAA Paper No. 79-1533, Presented at the AIAA 12th Fluid and Plasma Dynamics Conference, Williamsburg, VA, July 24-26, 1979.

12. Rizk, M. H. and Murman, E. M. "Wind Tunnel Wall Interference Corrections for Aircraft Models in the Transonic Regime." *Journal of Aircraft*, Vol. 21, No. 1, January 1984, pp. 54-61.

13. Rizk, M. H. "Improvements in Code TUNCOR for Calculating Wall Interference Corrections in the Transonic Regime." AEDC-TR-86-6 (AD-A166766), March 1986.

14. Lo, C. F. "Tunnel Interference Assessment by Boundary Measurements." *AIAA Journal*, Vol. 16, No. 4, April 1978, pp. 411-413.

15. Kraft, E. M. and Dahm, W. J. A. "Direct Assessment of Wall Interference in a Two-Dimensional Subsonic Wind Tunnel." AIAA Paper No. 82-0187, Presented at the AIAA 20th Aerospace Sciences Meeting, Orlando, Florida, January 11-14, 1982.

16. Lo, C. F. and Sickles, W. L. "Two-Measured Variable Method for Wall Interference Assessment/Correction." Presented at the Transonic Symposium, NASA Langley Research Center, Hampton, VA, April 19-21, 1988.

17. Murman, E. M., Bailey, F. R., and Johnson, M. L. "TSFOIL-A Computer Code for Two-Dimensional Transonic Calculations, Including Wind Tunnel Wall Effects and Wave Drag Evaluation." NASA SP-347, March 1975, pp. 769-788.

18. Benek, J. A. "Chimera: A Grid-Embedding Technique." AEDC-TR-85-64 (AD-A167466), April 1986.

19. Rizk, M. H. and Lovell, D. "Two-Dimensional Transonic Wind Tunnel Wall Interference Corrections Based on the Euler Equations." AIAA Paper No. 86-0124, Presented at the AIAA 24th Aerospace Sciences Meeting, Reno, NV, January 6-9, 1986.

20. Whitfield, D. L. "Integral Solution of Compressible Turbulent Boundary Layers Using Improved Velocity Profiles." AEDC-TR-78-42 (AD-A062946), December 1978.

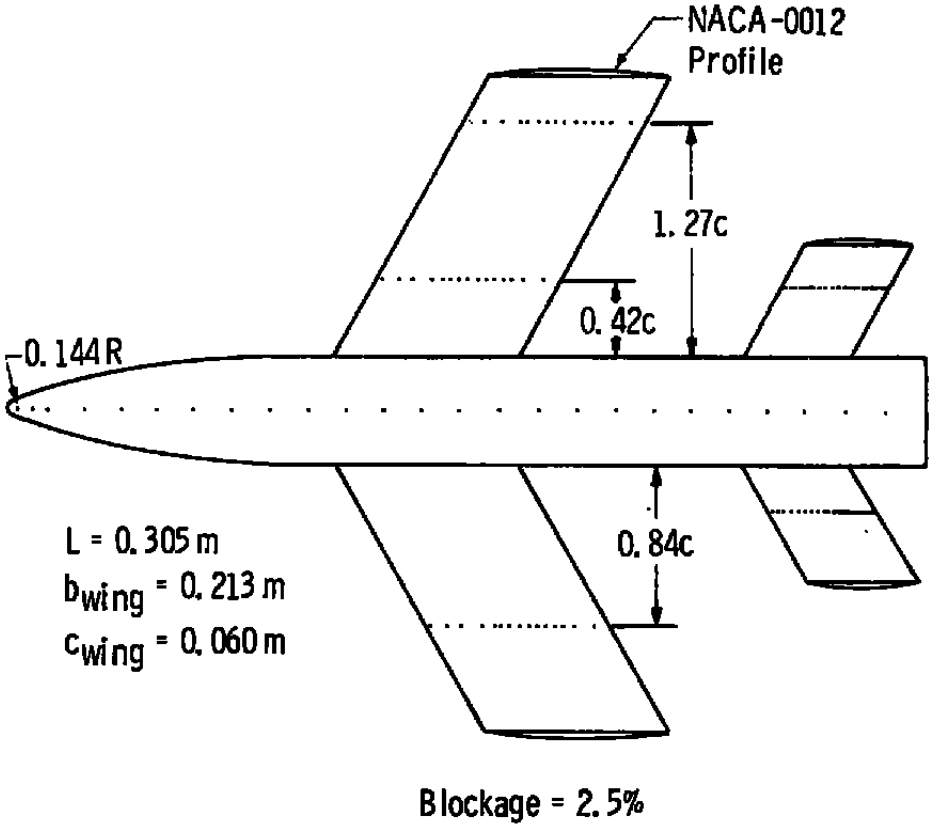

Figure 1. Three-dimensional experimental model.

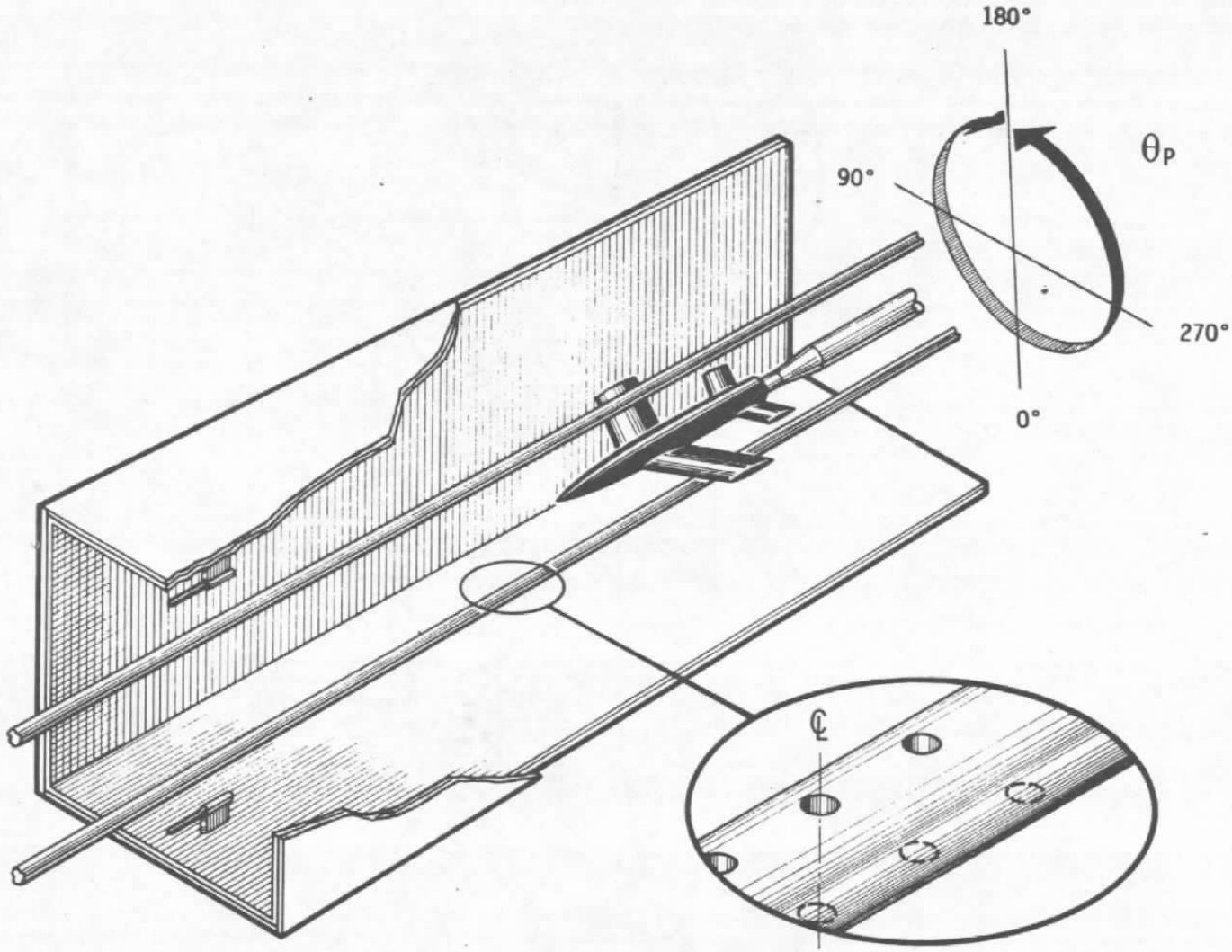

Figure 2. Aerodynamic Wind Tunnel (1T) interface measurement system.

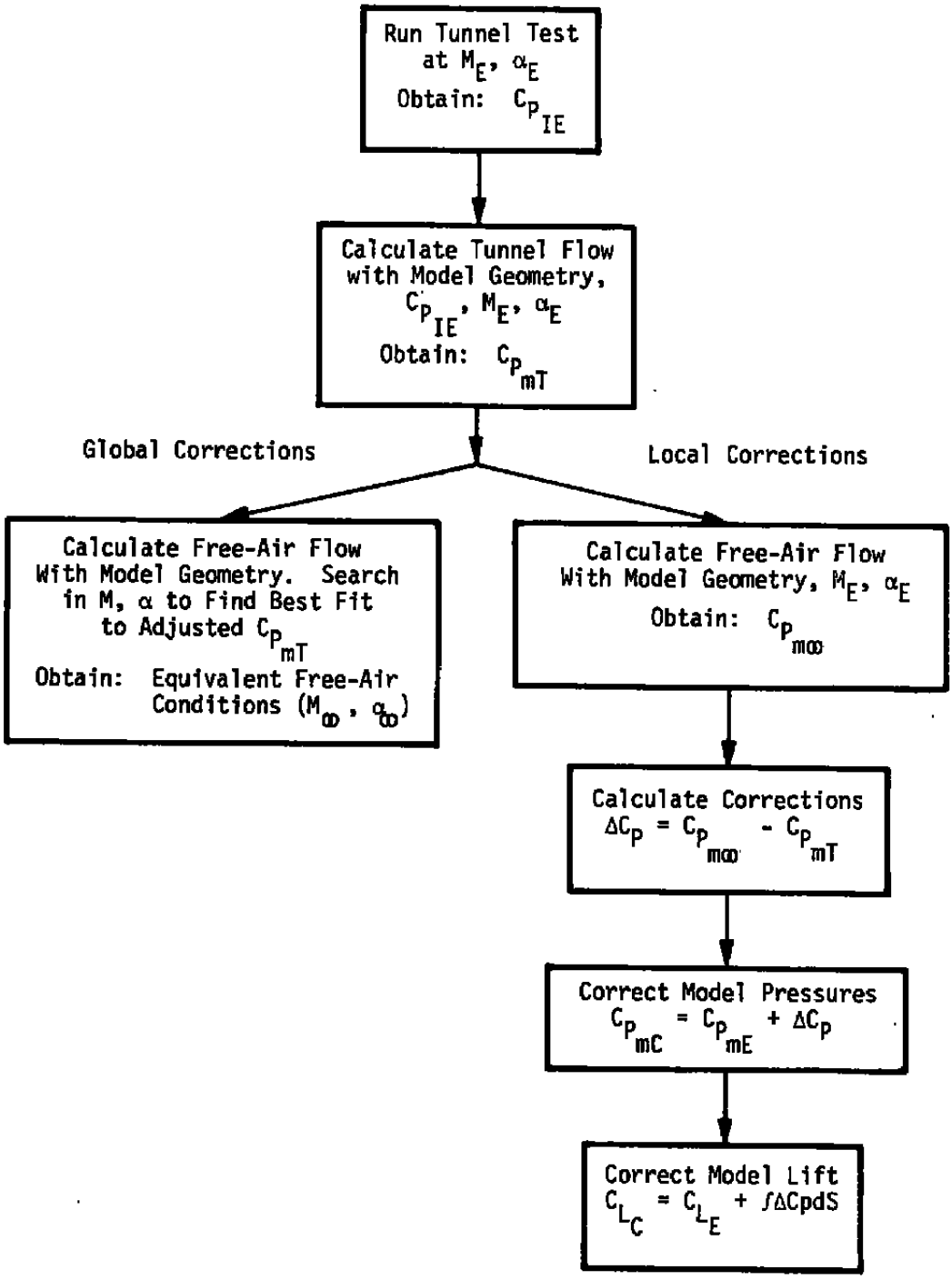

Figure 3. AEDC single-measured-variable procedure.

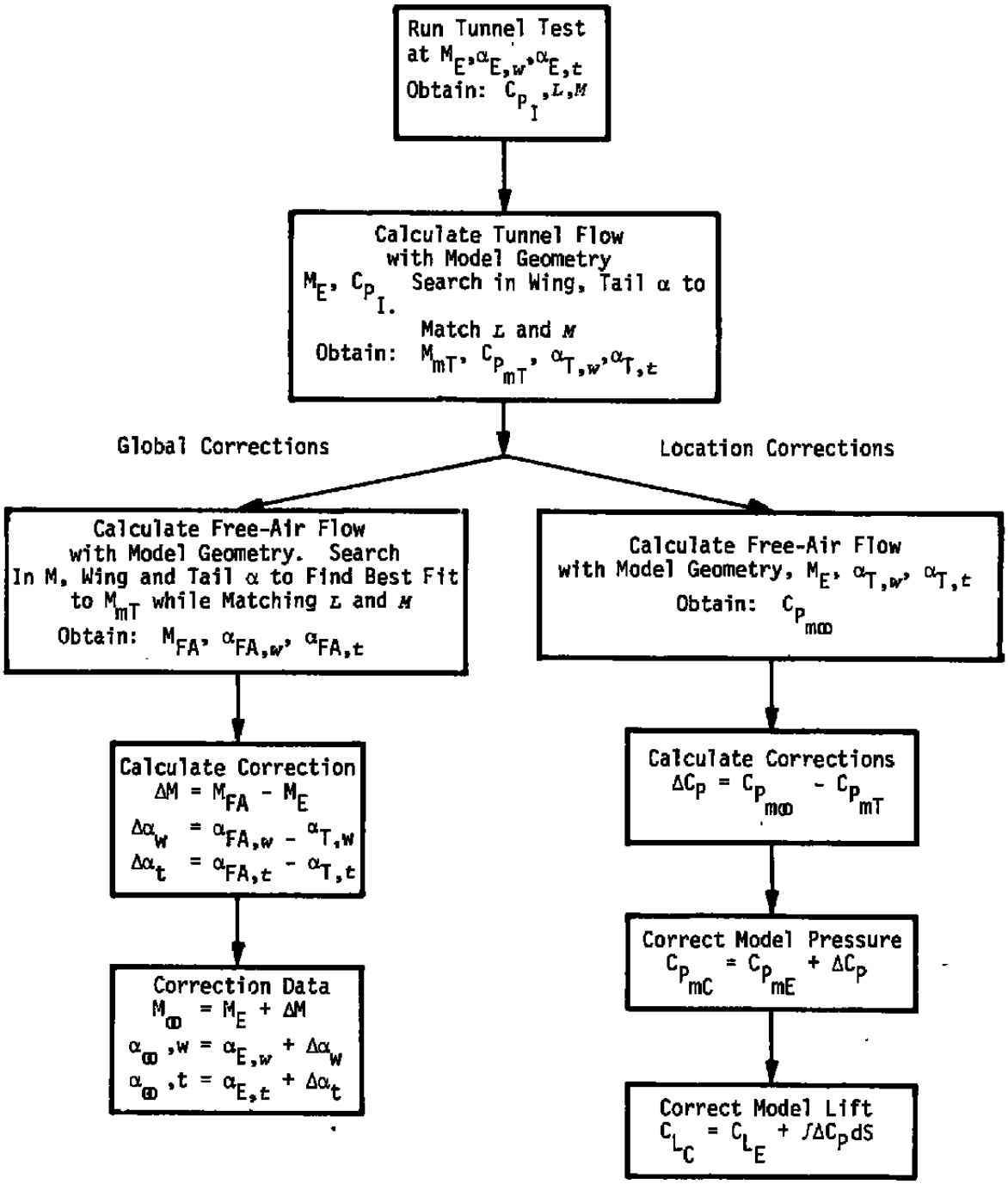

Figure 4. TUNCOR single-measured-variable procedure.

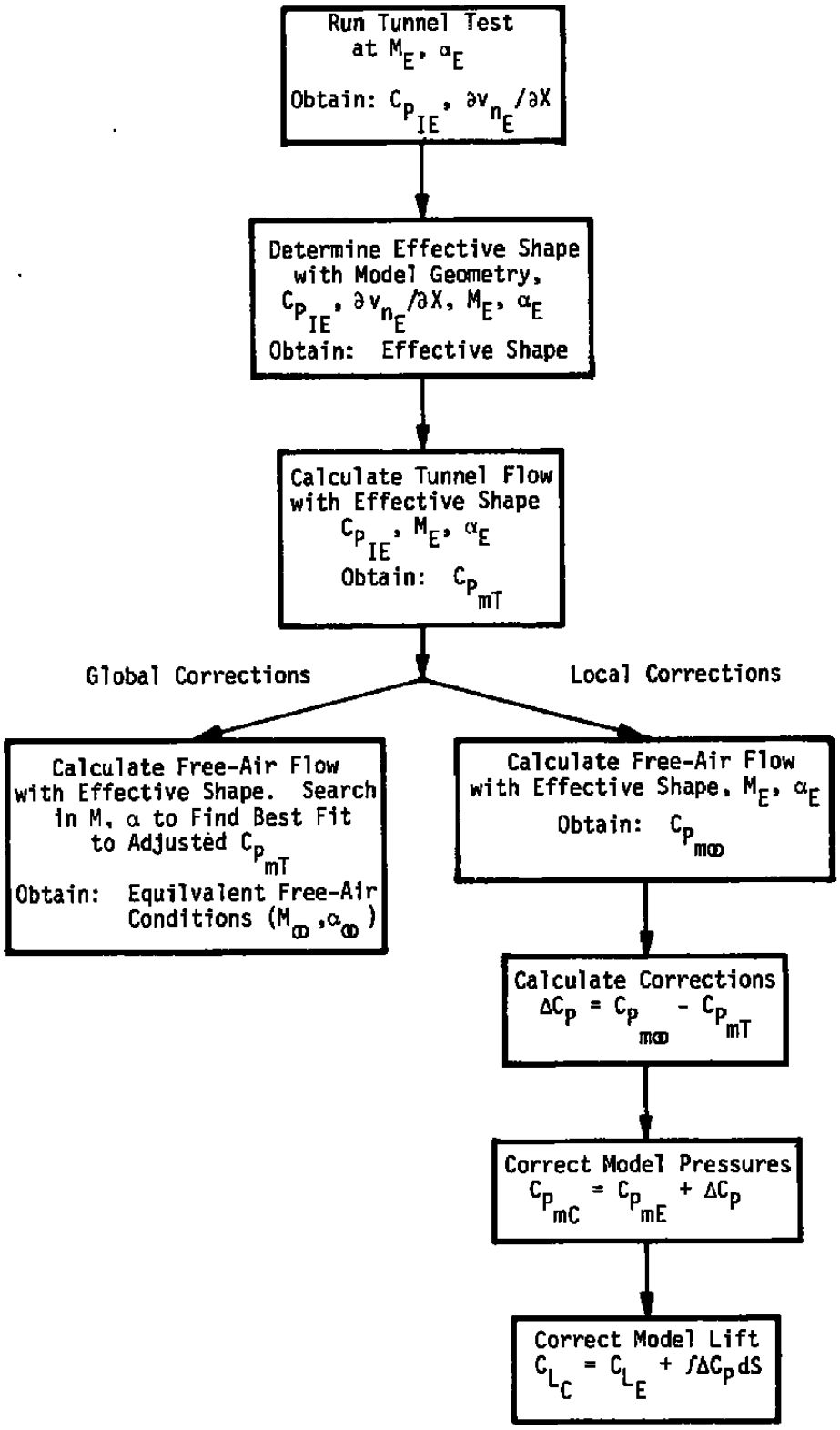

Figure 5. AEDC two-measured-variable procedure.

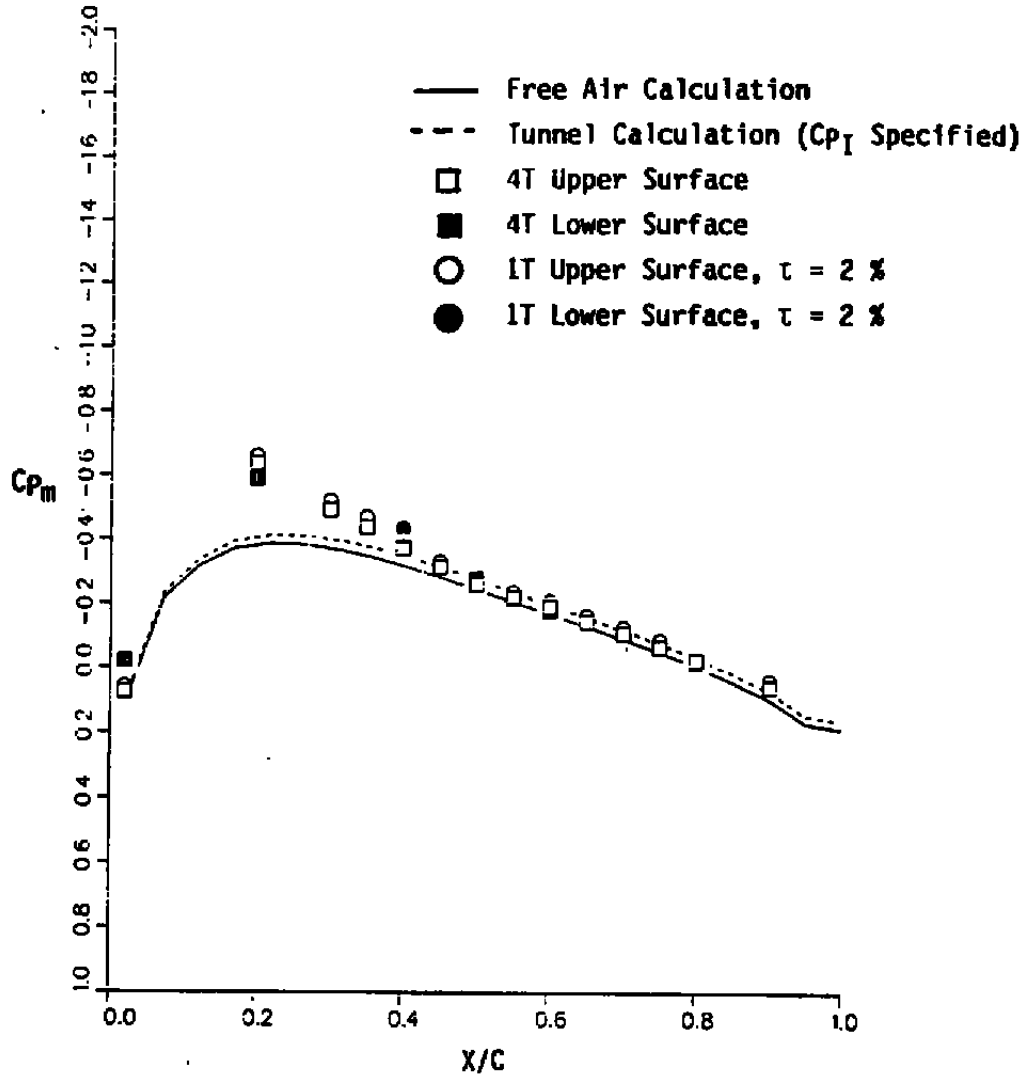

a. 60-percent wing semispan

Figure 6. Model pressures measured and calculated using the SMV-TSD Code, M_E = 0.80 and α_E = 0 deg.

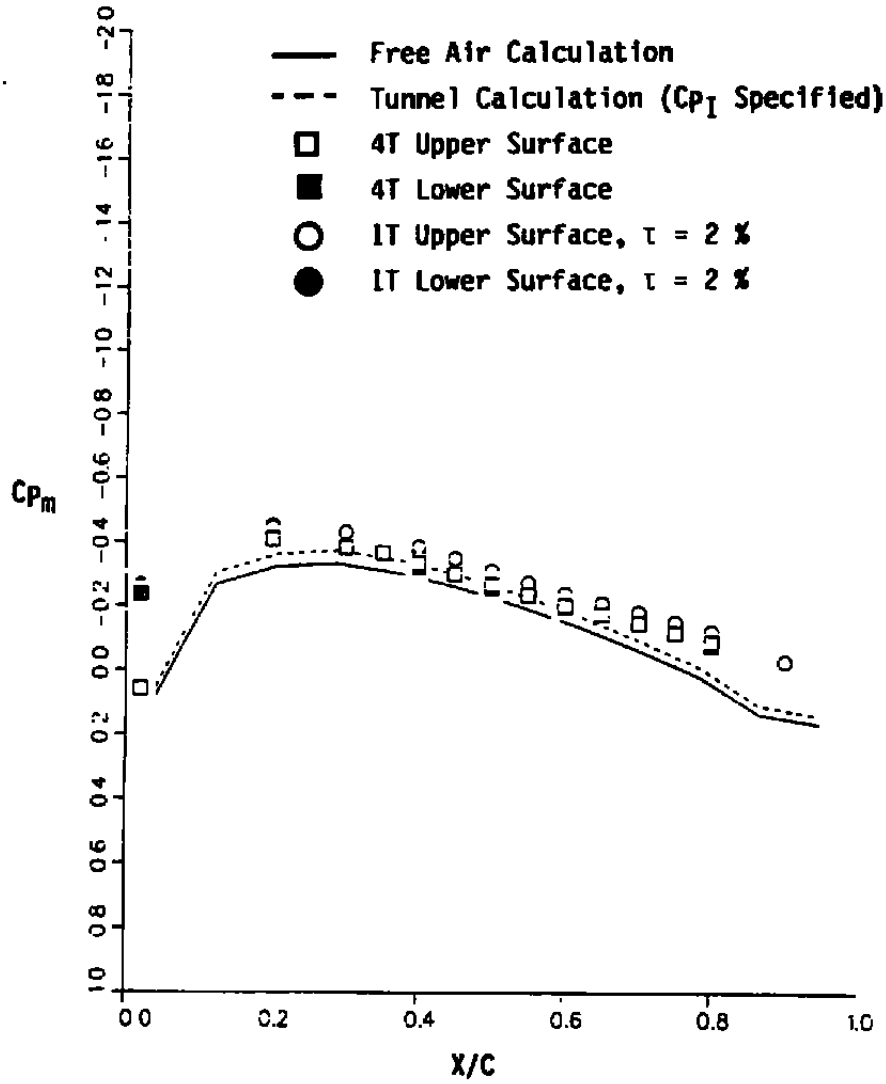

b. 60-percent tail semispan
Figure 6. Continued.

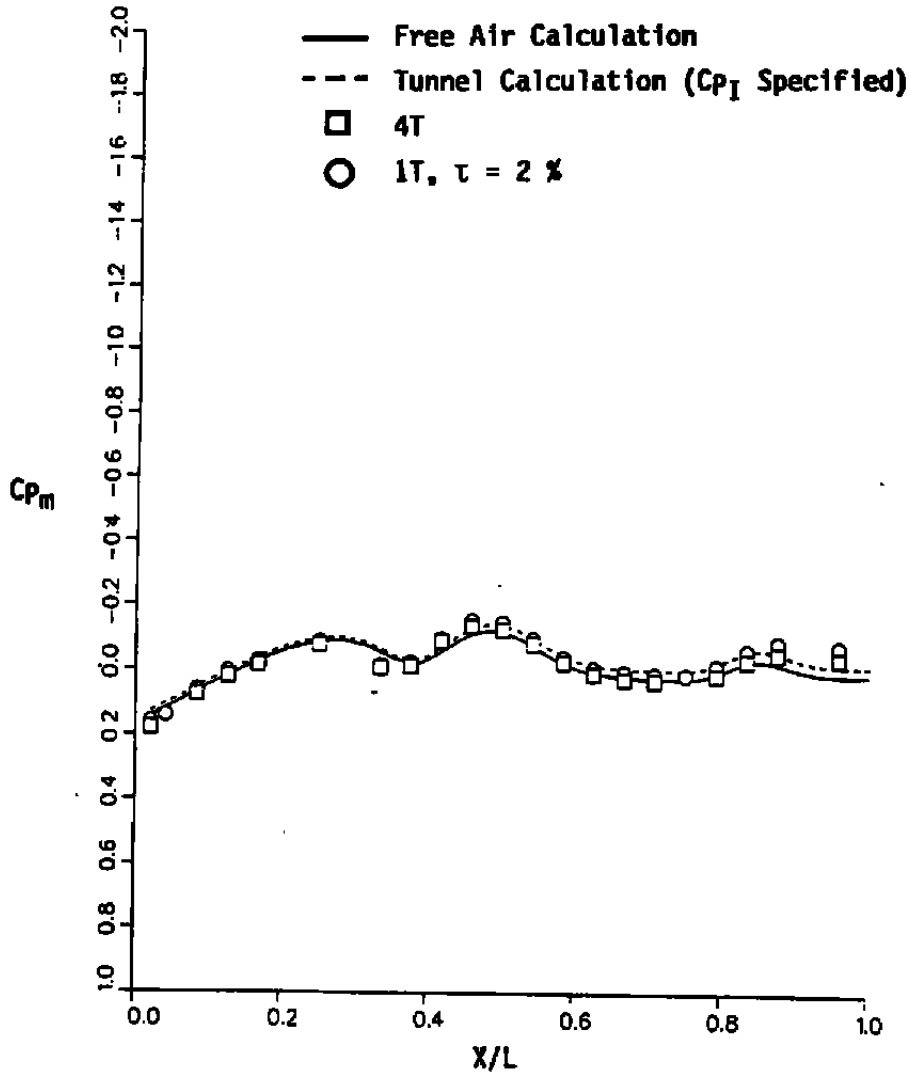

c. Fuselage top
Figure 6. Concluded.

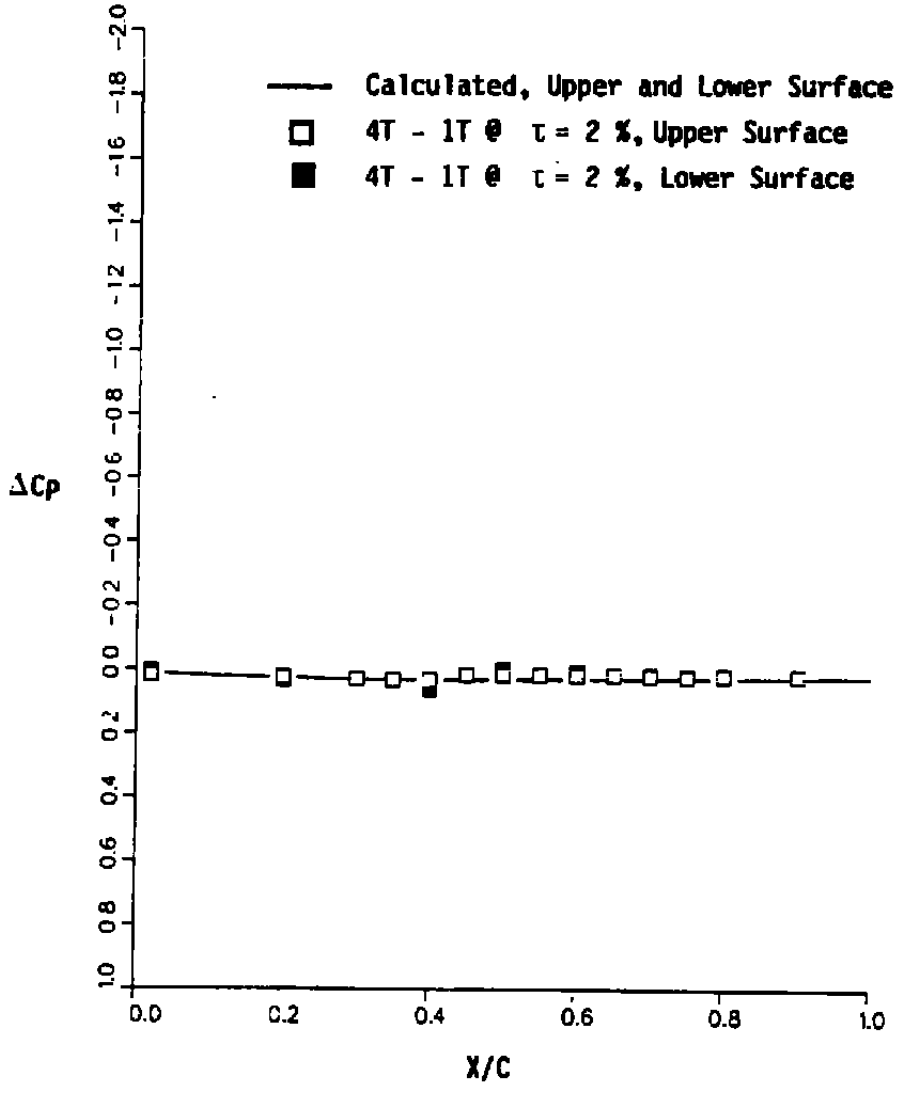

a. 60-percent wing semispan

Figure 7. Model local corrections measured and calculated using the SMV-TSD Code, M_E = 0.80 and α_E = 0 deg.

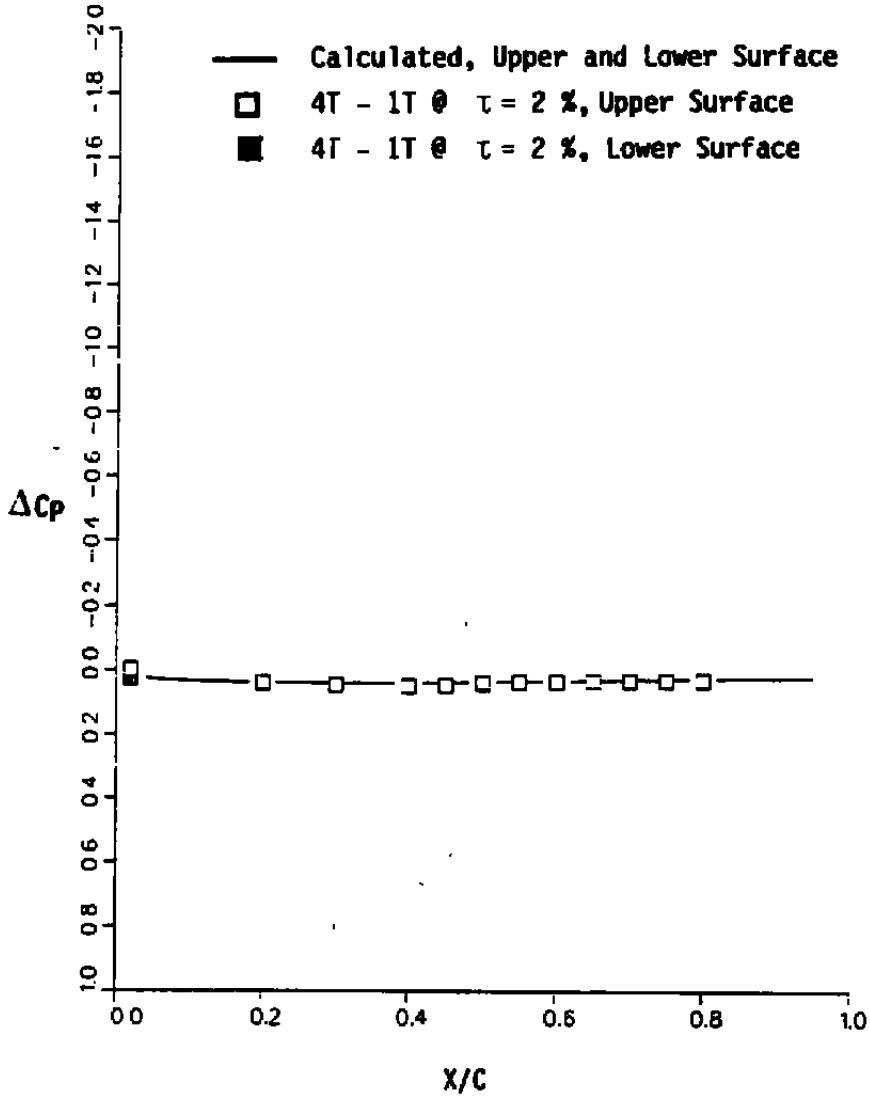

b. 60-percent tail semispan
Figure 7. Continued.

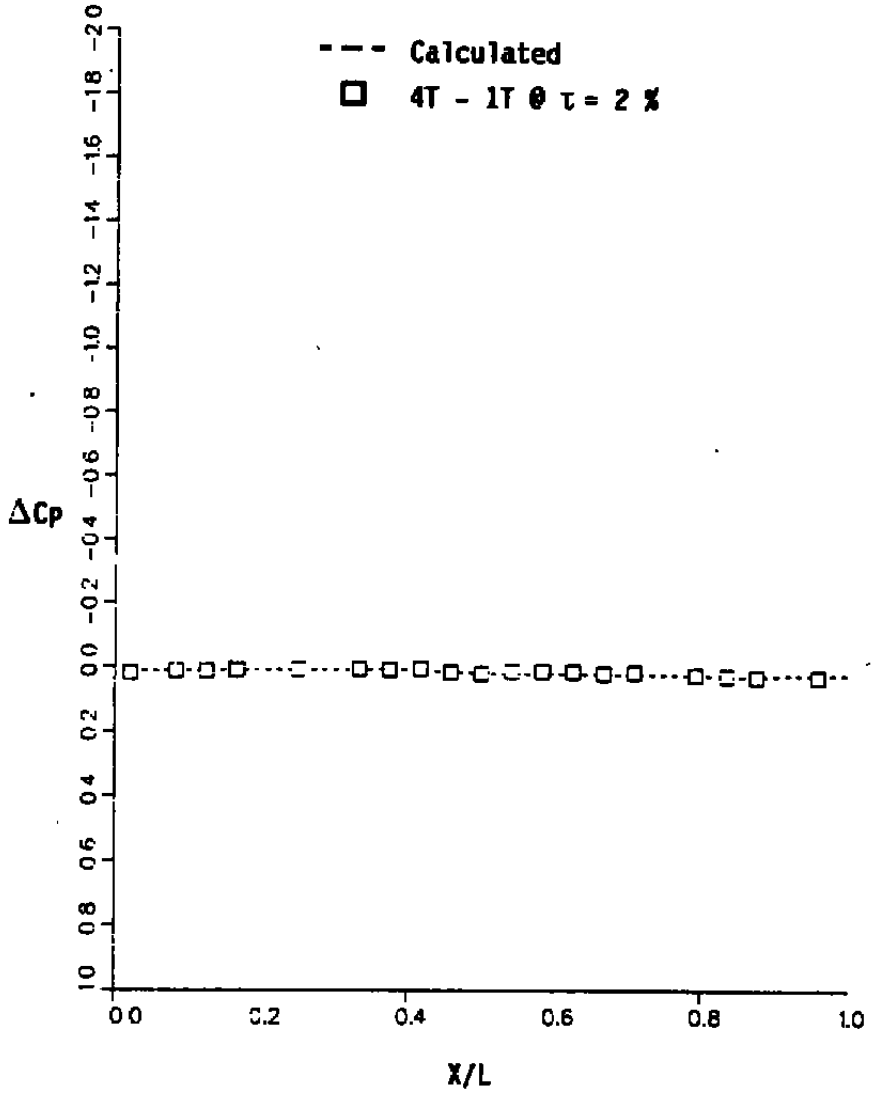

c. Fuselage top
Figure 7. Concluded.

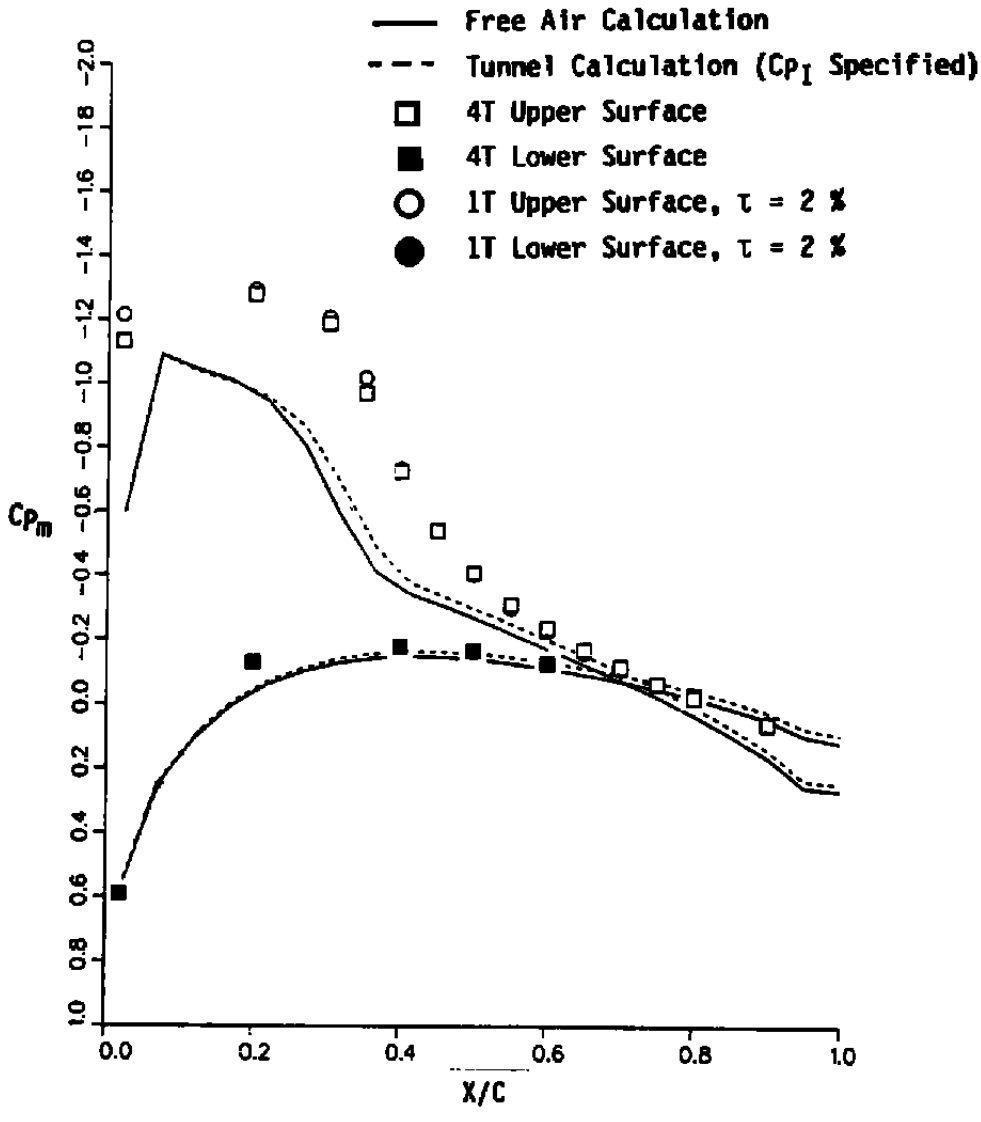

a. 60-percent wing semispan

Figure 8. Model pressure measured and calculated using the SMV-TSD Code, M_E = 0.80 and α_E = 6 deg.

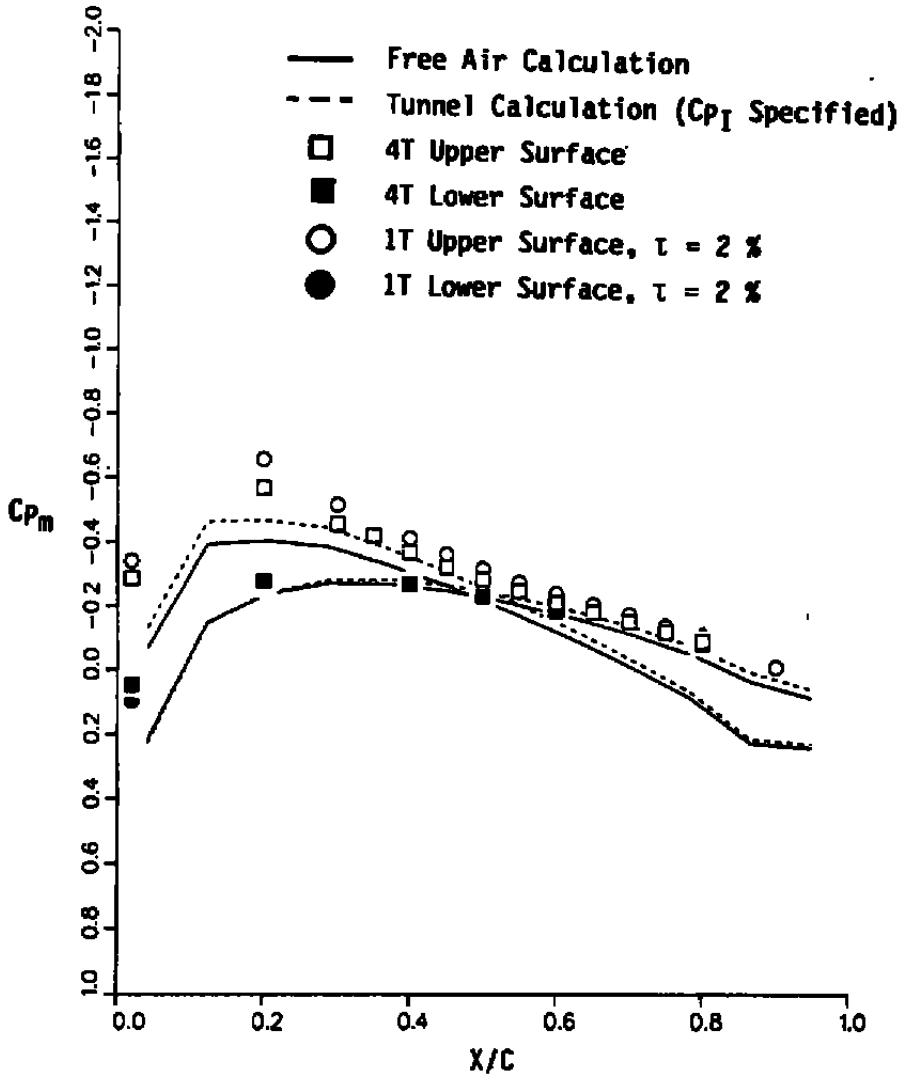

b. 60-percent tail semispan
Figure 8. Continued.

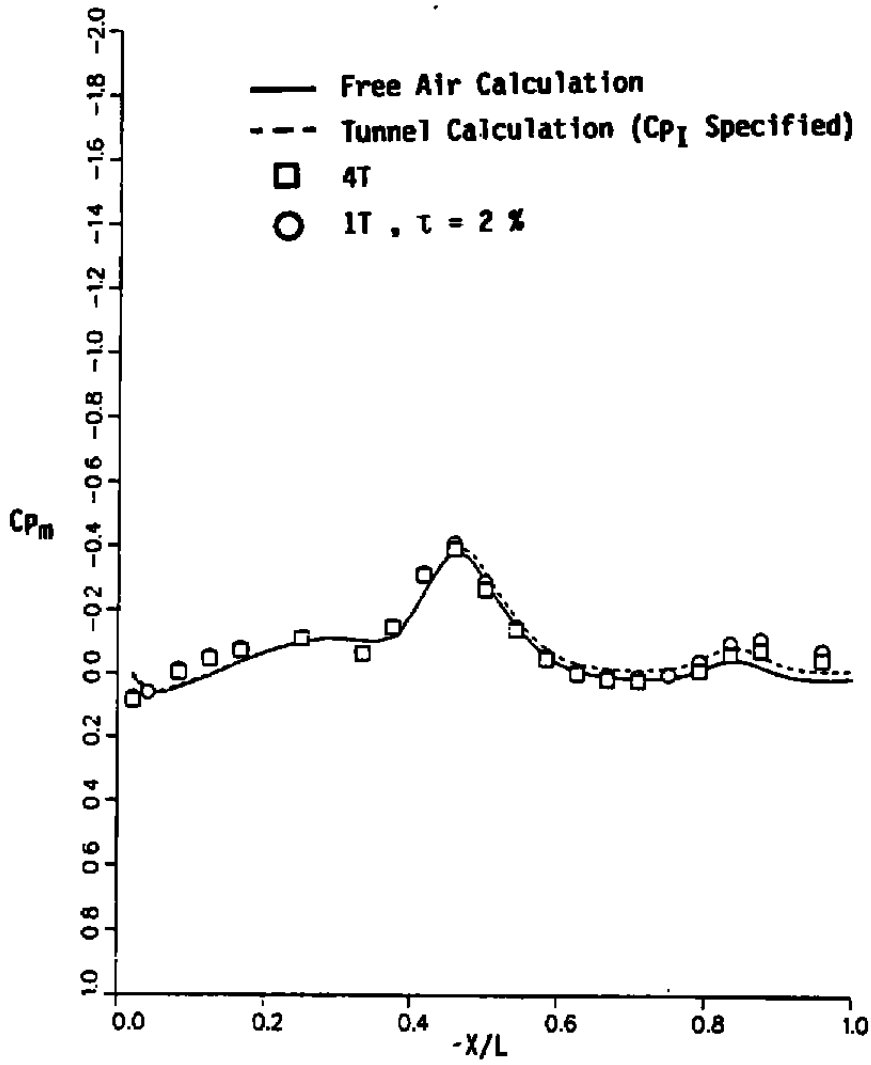

c. Fuselage top
Figure 8. Concluded.

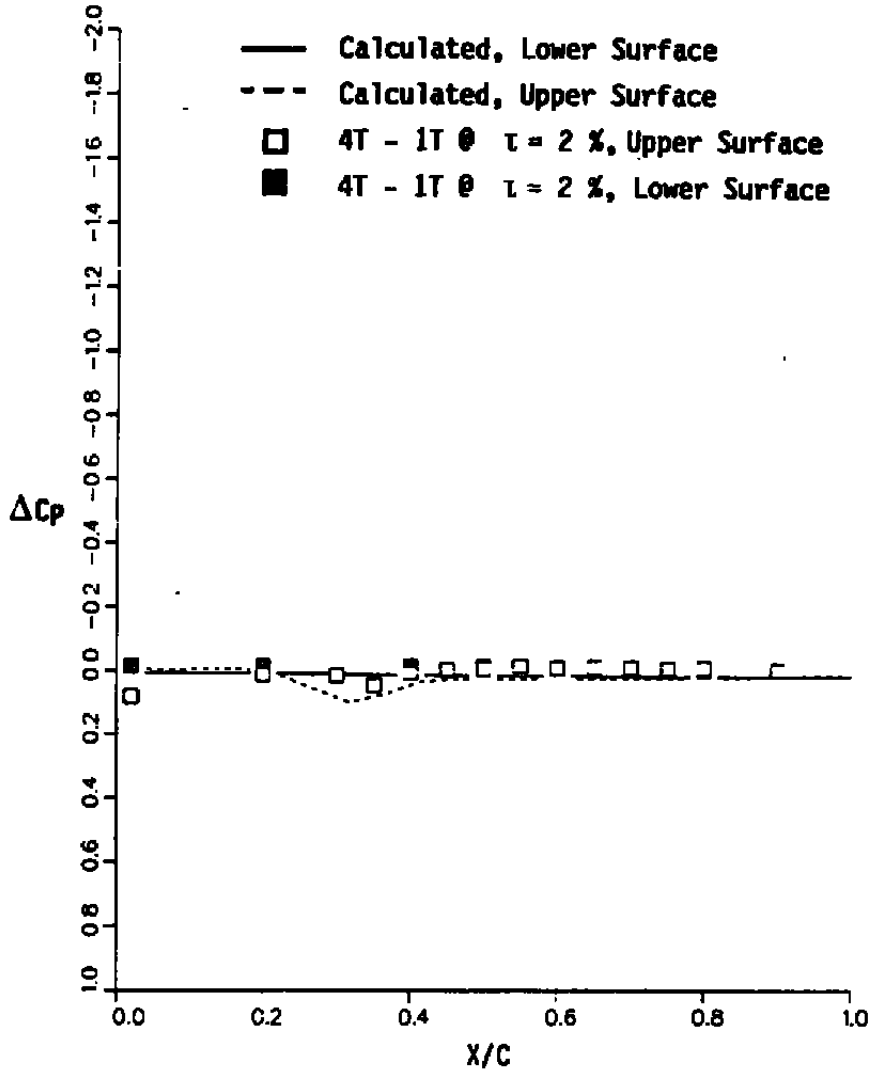

a. 60-percent wing semispan

Figure 9. Model local corrections measured and calculated using the SMV-TSD Code, M_E = 0.80 and α_E = 6 deg.

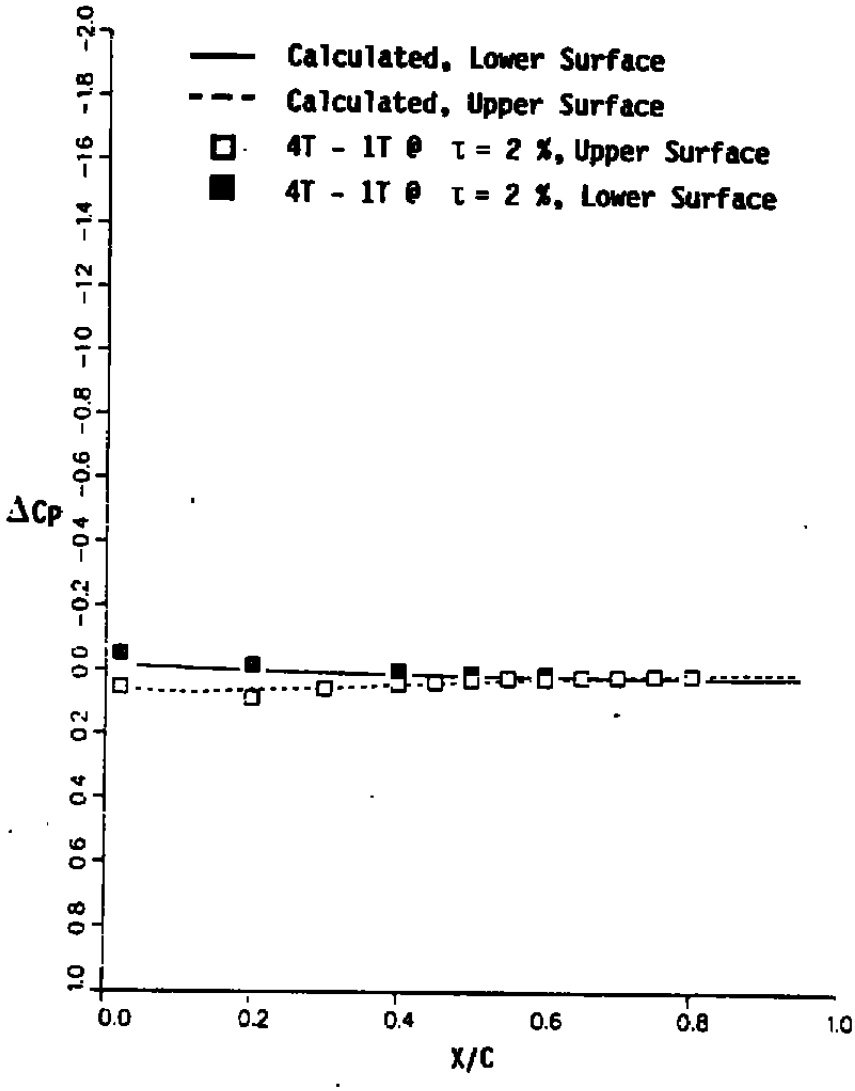

b. 60-percent tail semispan
Figure 9. Continued.

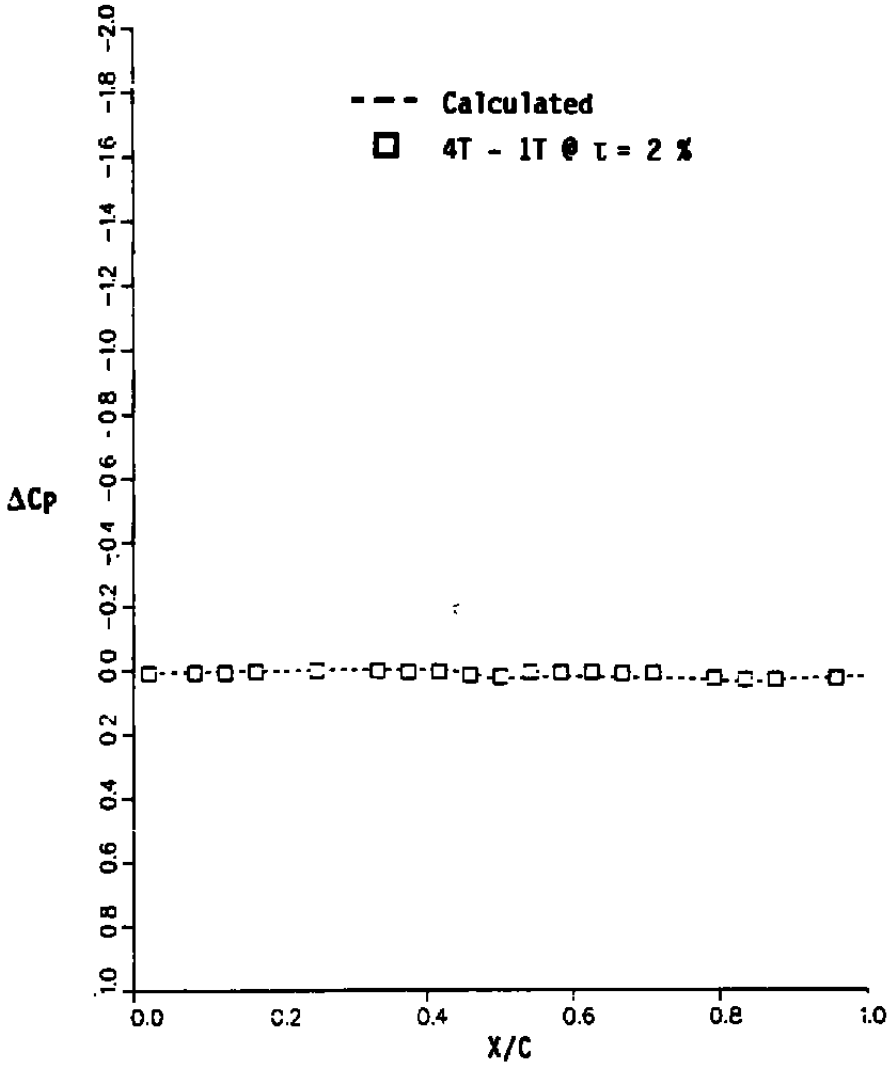

c. Fuselage top
Figure 9. Concluded.

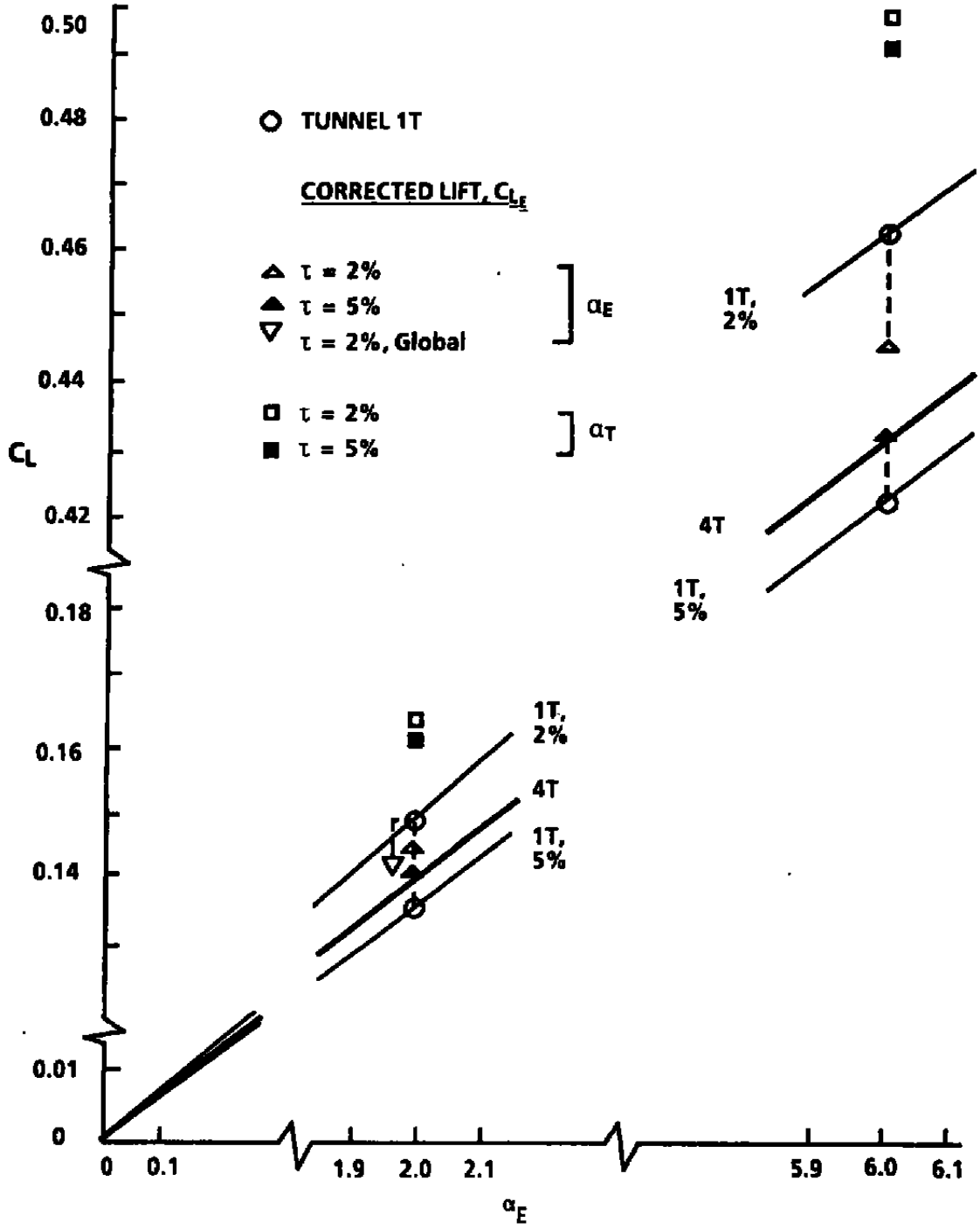

Figure 10. Corrected lift coefficient at α_E and α_T using the SMV-TSD Code for $M_E = 0.80$.

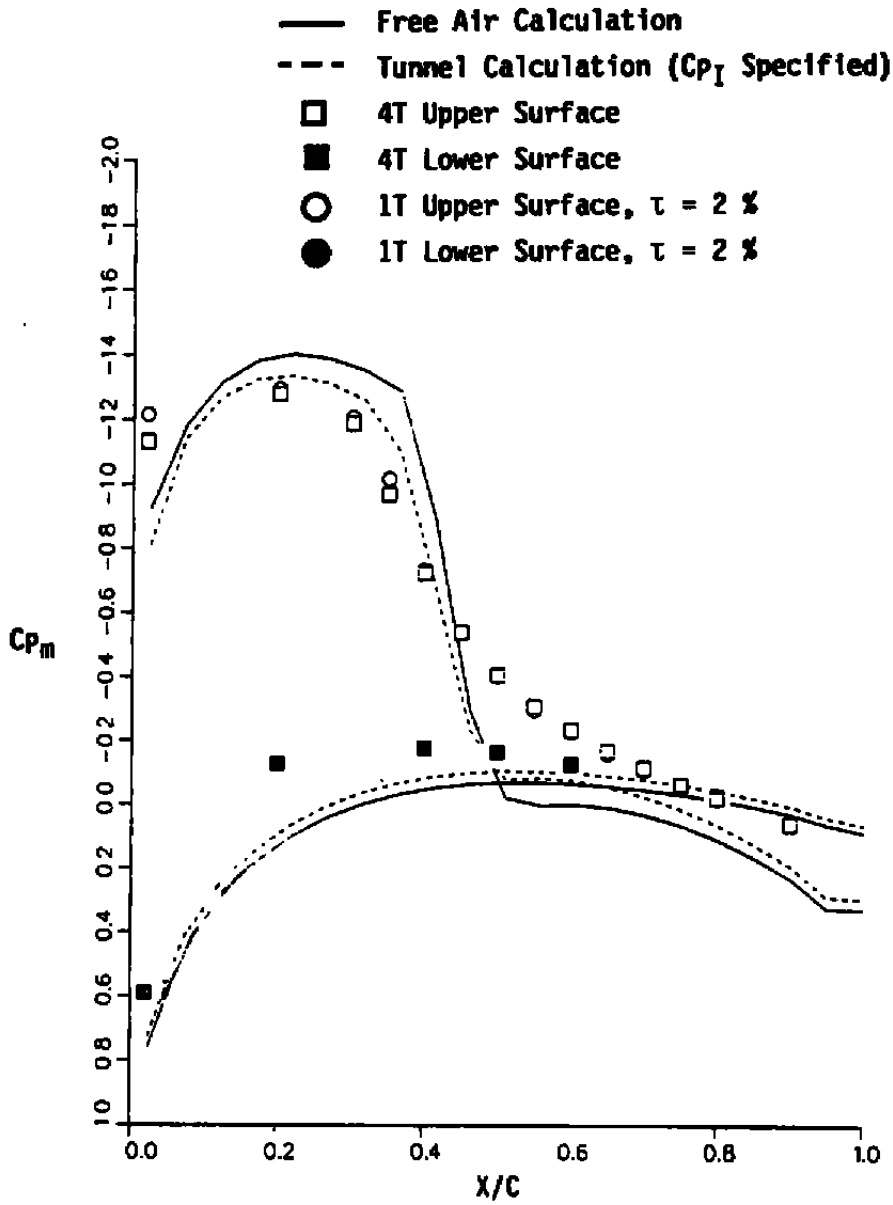

Figure 11. Model pressures measured and calculated using the SMV-TSD Code while matching measured lift, 60-percent wing semispan, M_E = 0.80, and α_T = 9.5 deg.

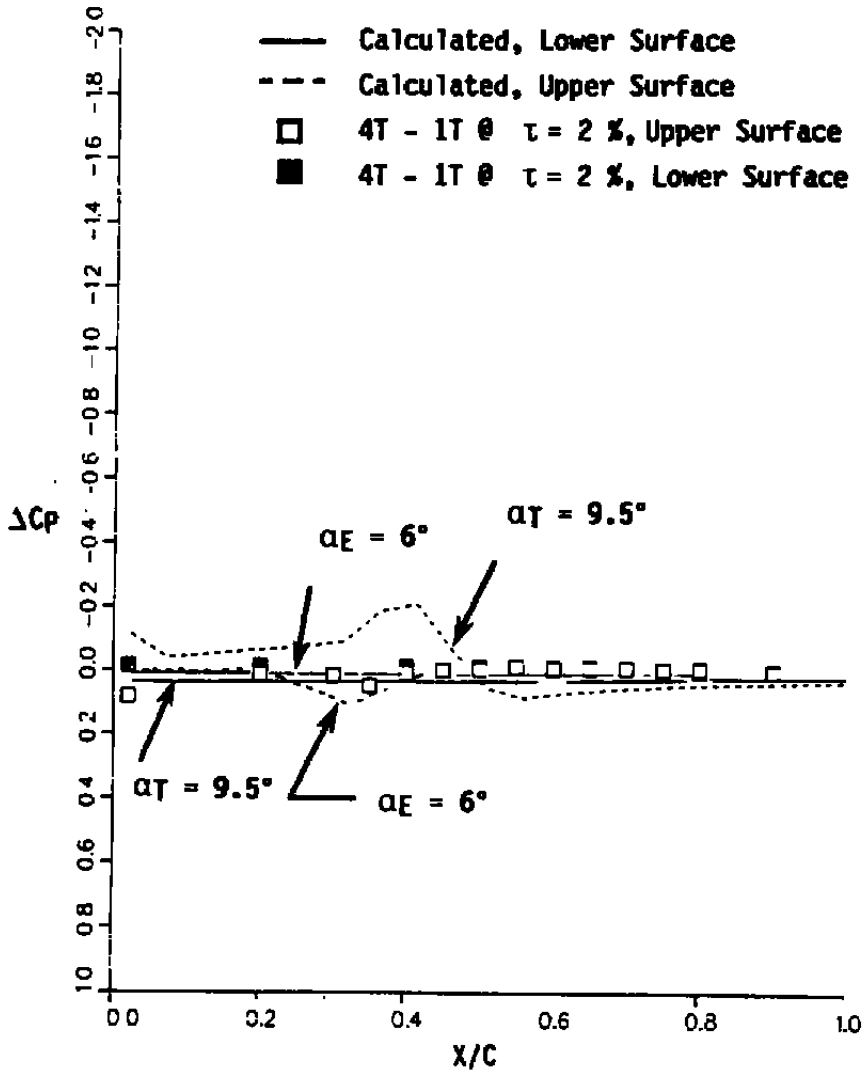

Figure 12. Model local corrections measured and calculated using the SMV-TSD Code while matching measured lift, 60-percent wing semispan, M_E = 0.80, α_E = 6 deg, and α_T = 9.5 deg.

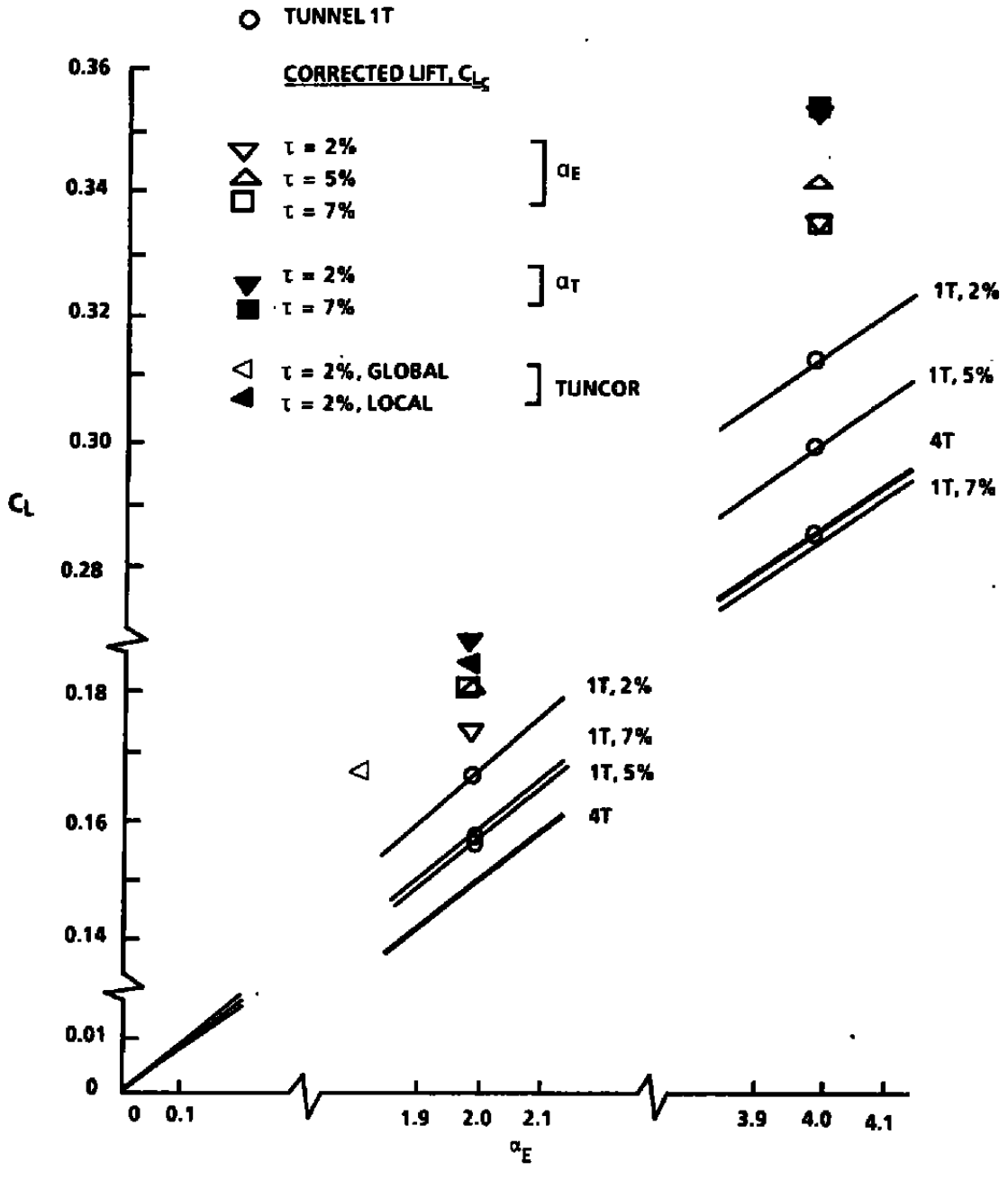

Figure 13. Corrected lift coefficient at α_E and α_T using the SMV-TSD and SMV-TUNCOR Codes for M_E = 0.90.

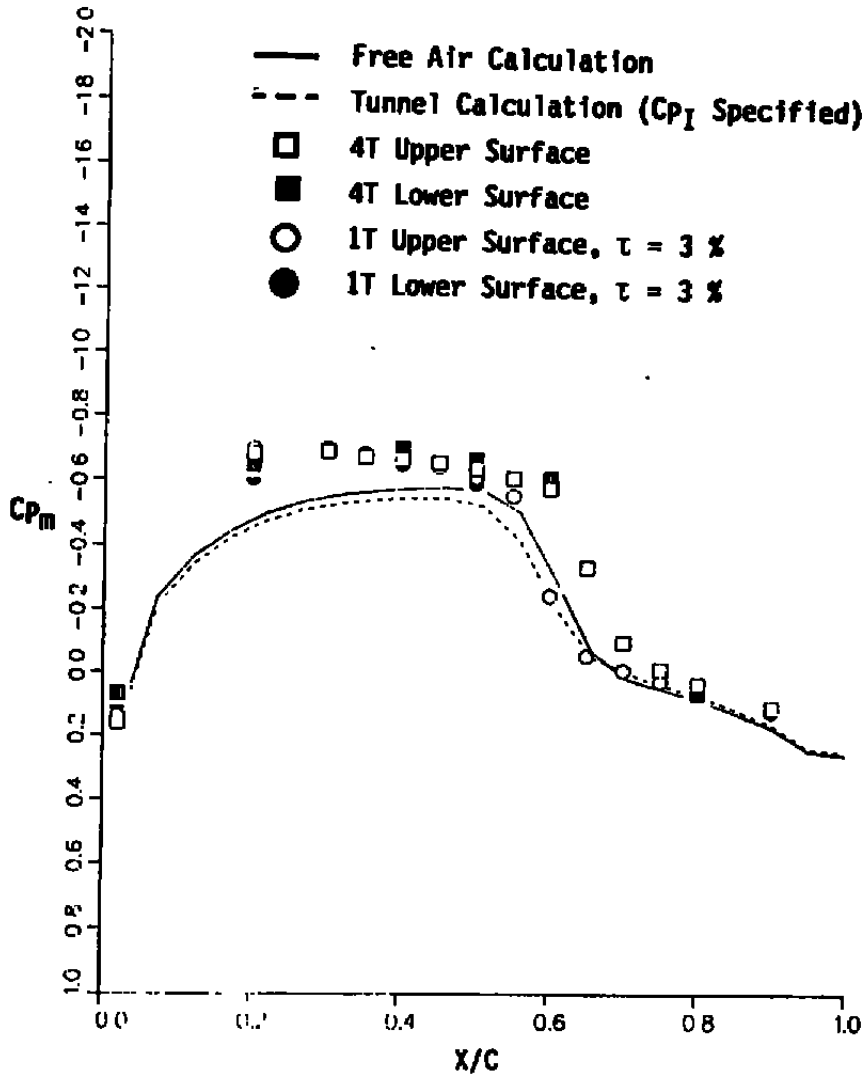

a. 60-percent wing semispan

Figure 14. Model pressures measured and calculated using the SMV-TSD Code, M_E = 0.90 and α_E = 0 deg.

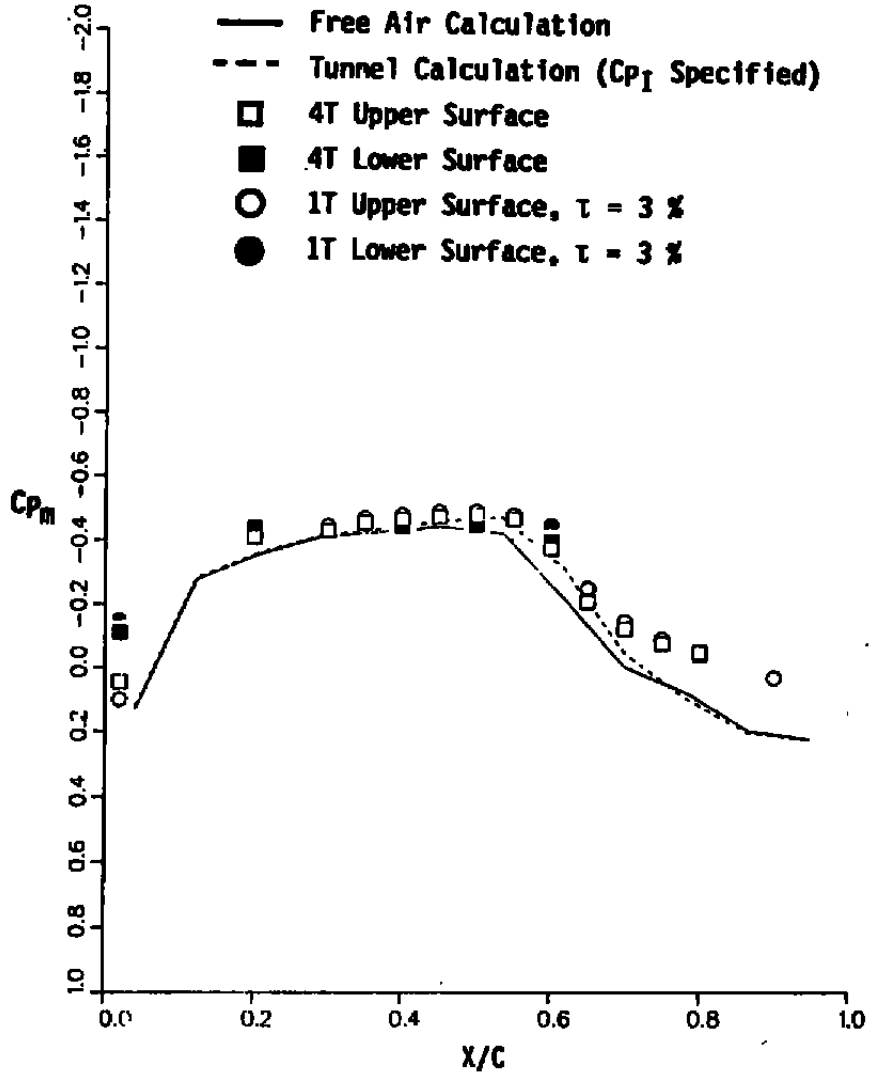

b. 60-percent tail semispan
Figure 14. Continued.

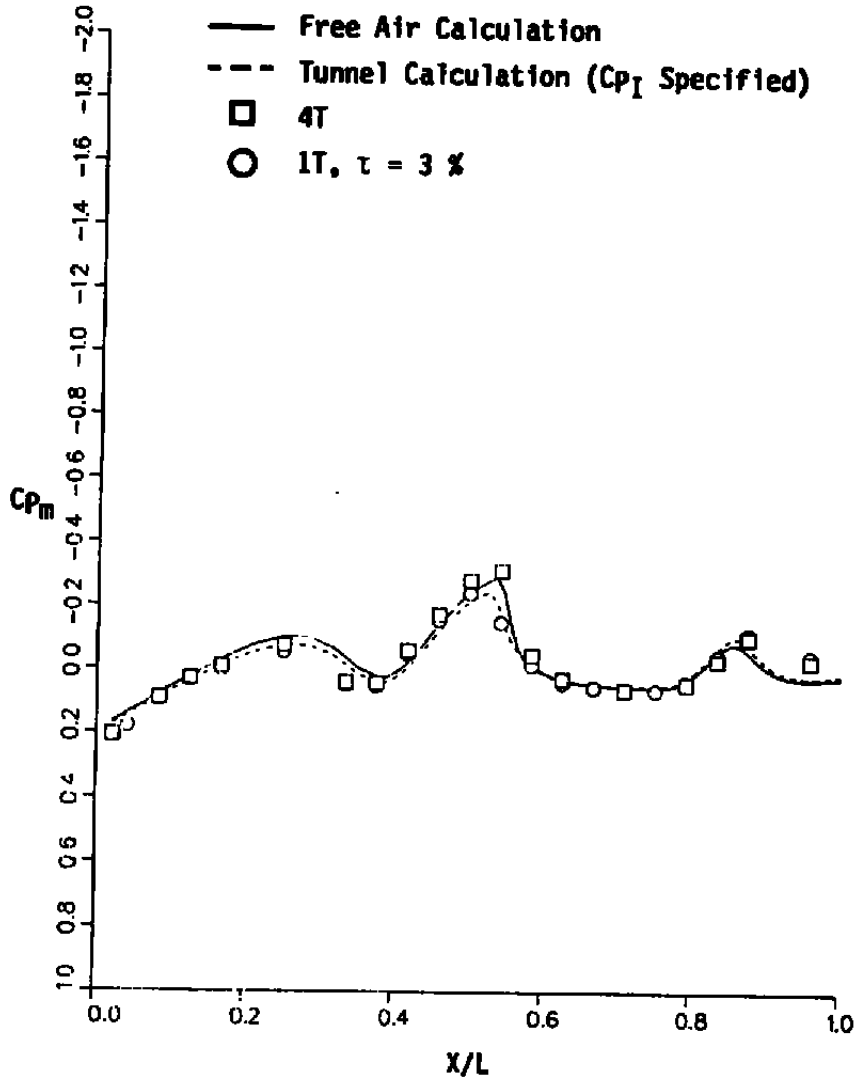

c. Fuselage top
Figure 14. Concluded.

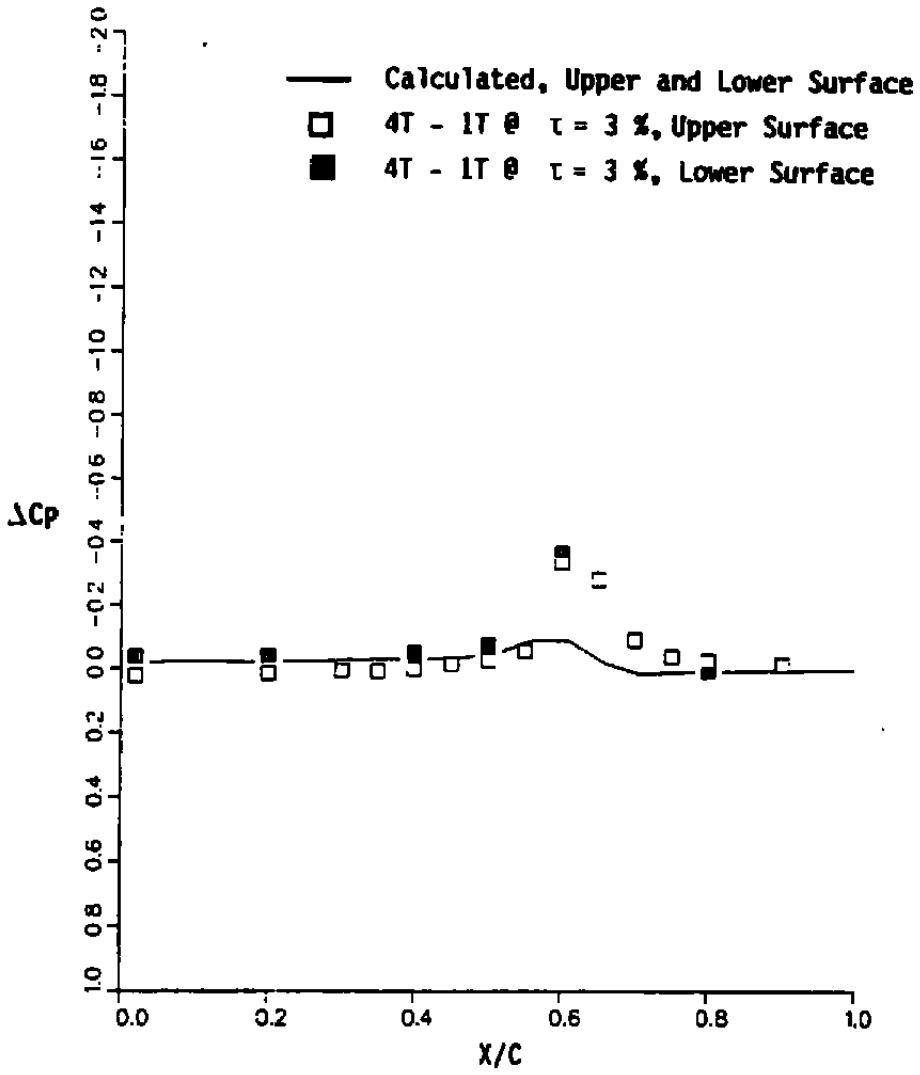

a. 60-percent wing semispan

Figure 15. Model local corrections measured and calculated using the SMV-TSD Code, M_E = 0.90 and α_E = 0 deg.

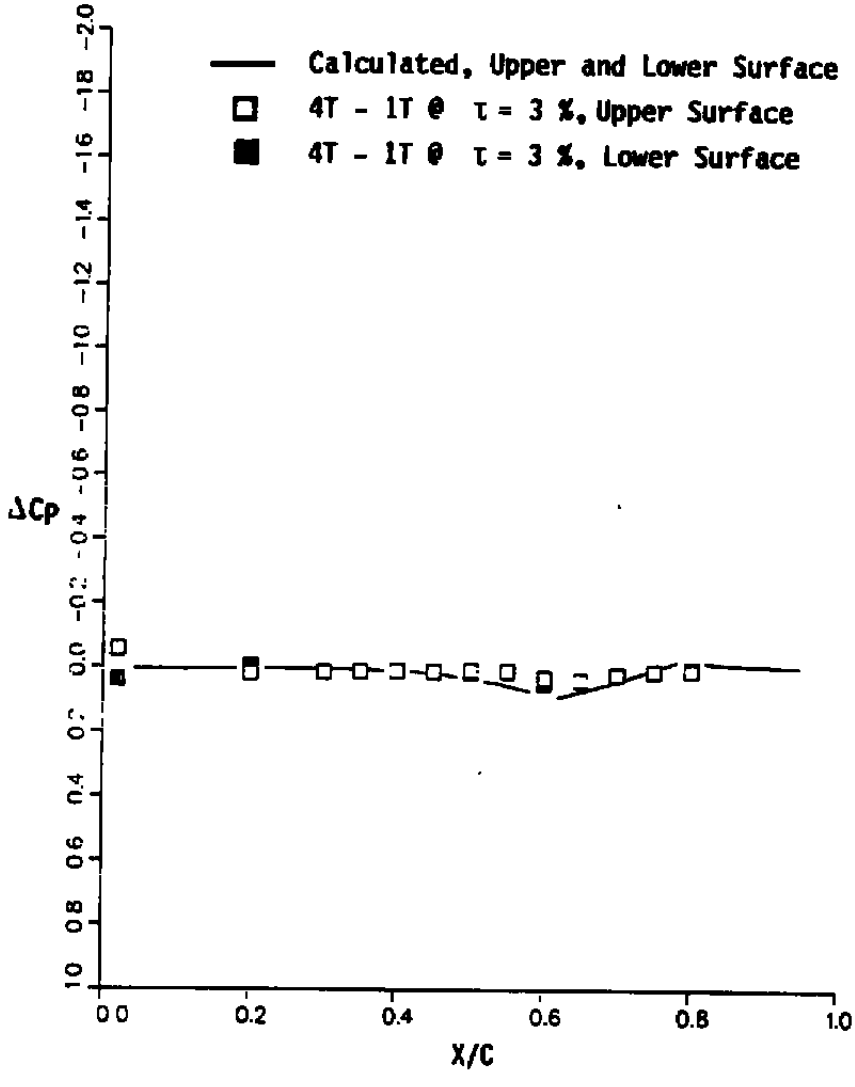

b. 60-percent tail semispan
Figure 15. Continued.

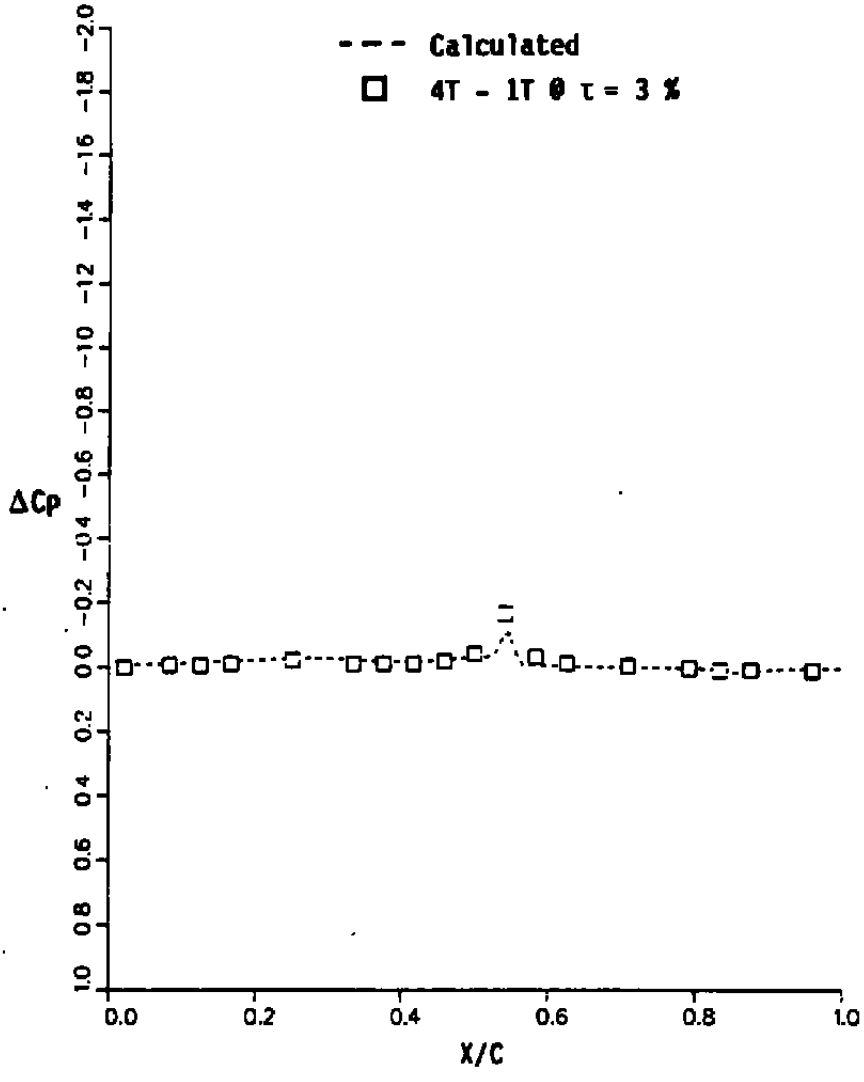

c. Fuselage top
Figure 15. Concluded.

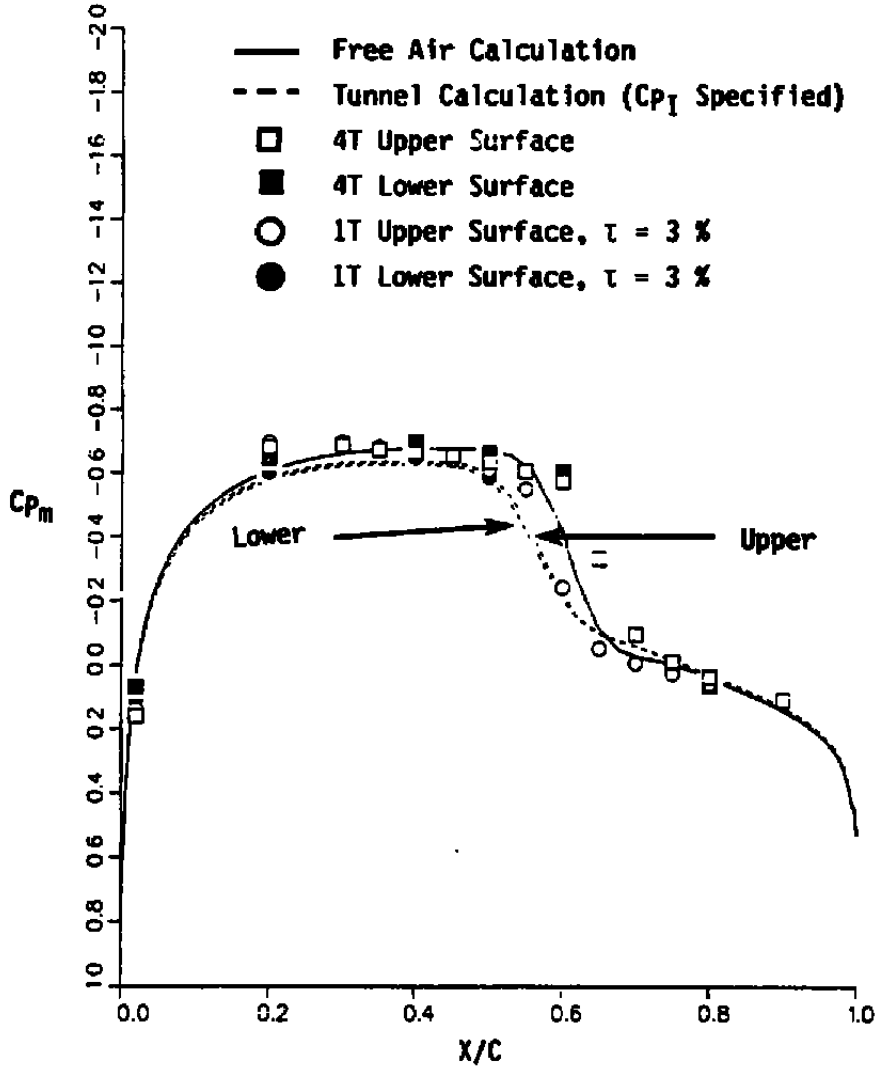

a. 60-percent wing semispan

Figure 16. Model pressures measured and calculated using the SMV-Euler Code, M_E = 0.90 and α_E = 0 deg.

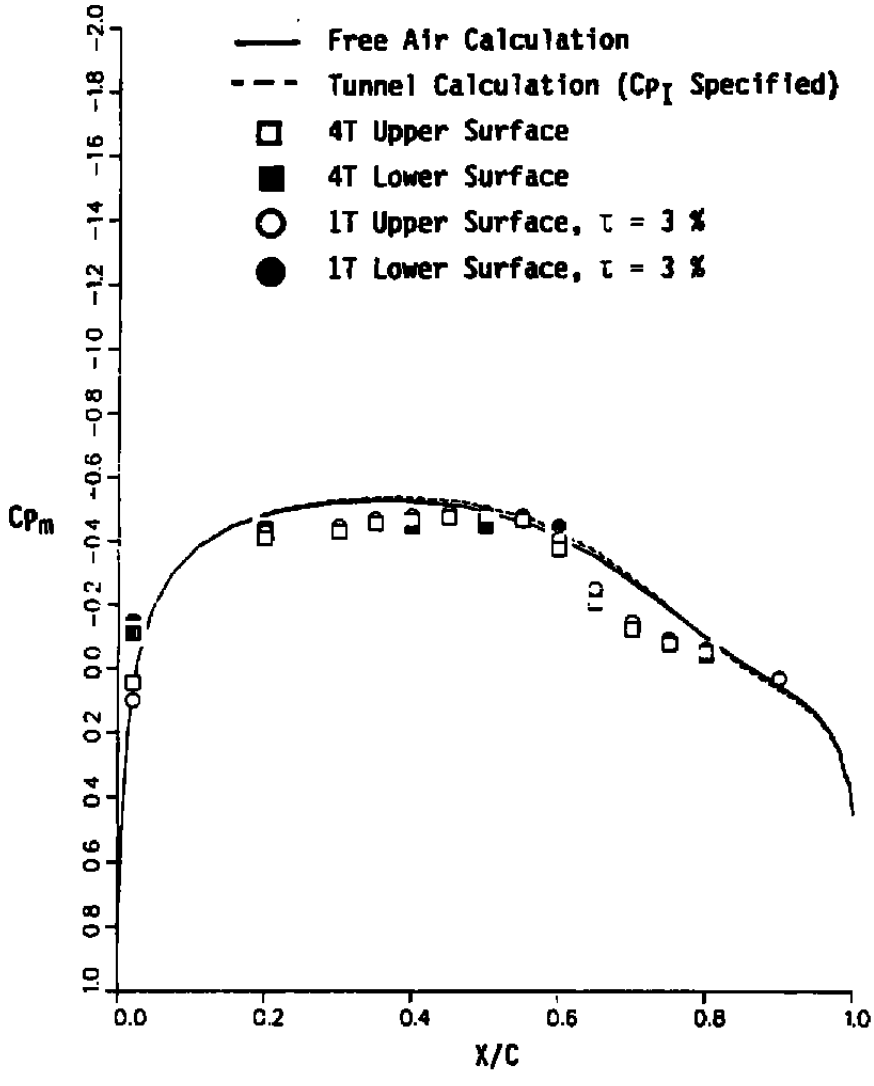

b. 60-percent tail semispan
Figure 16. Continued.

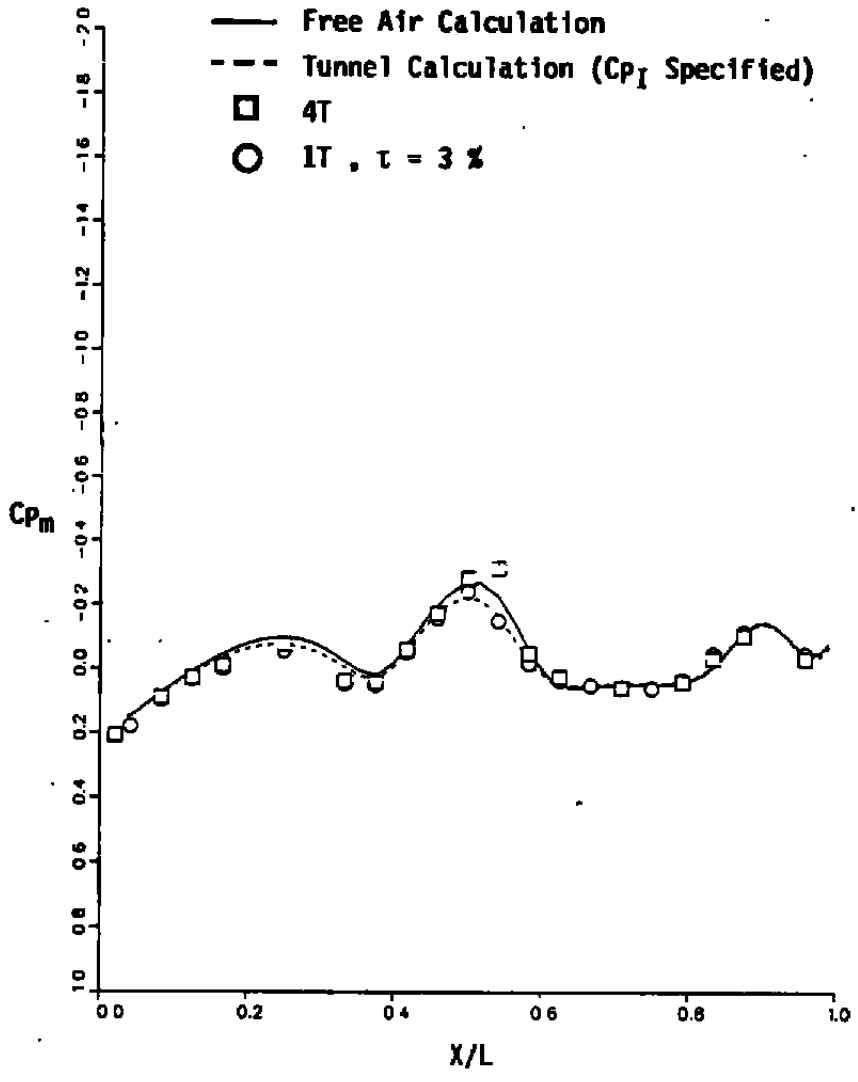

c. Fuselage top
Figure 16. Concluded.

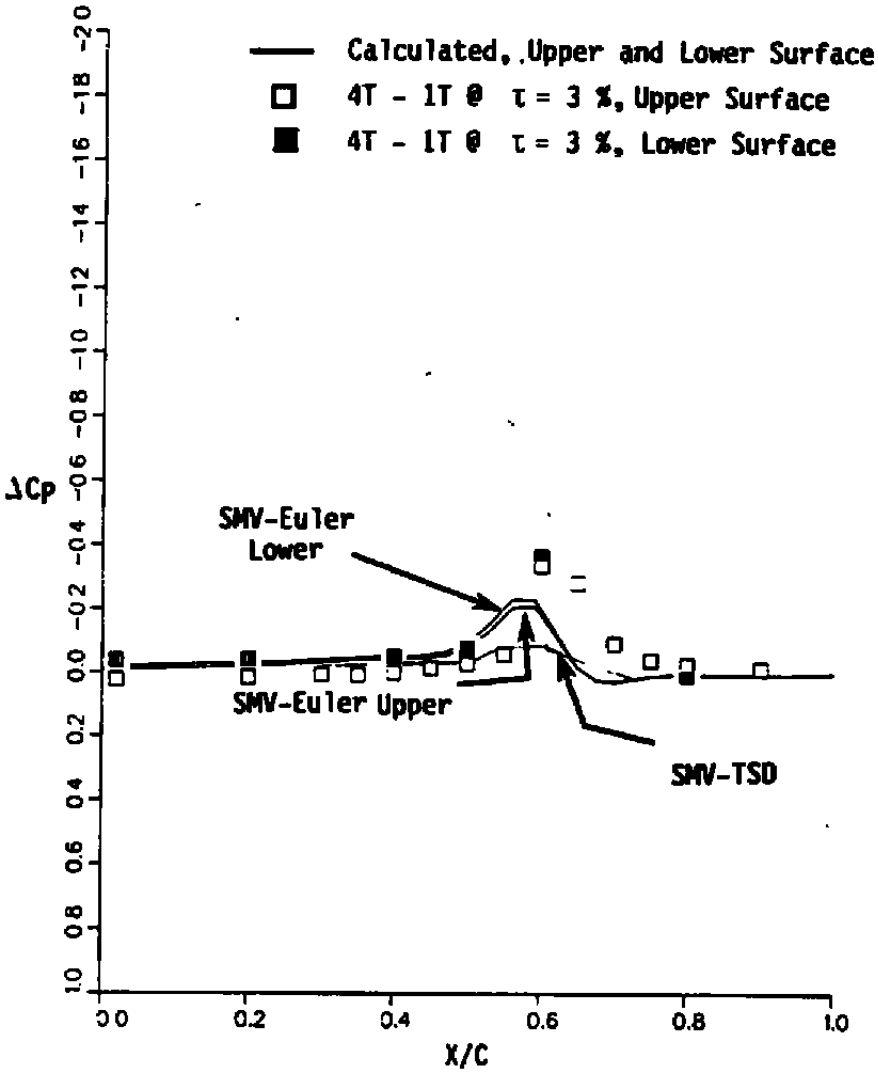

a. 60-percent wing semispan

Figure 17. Model local corrections measured and calculated using the SMV-Euler and SMV-TSD Codes, M_E = 0.90 and α_E = 0 deg.

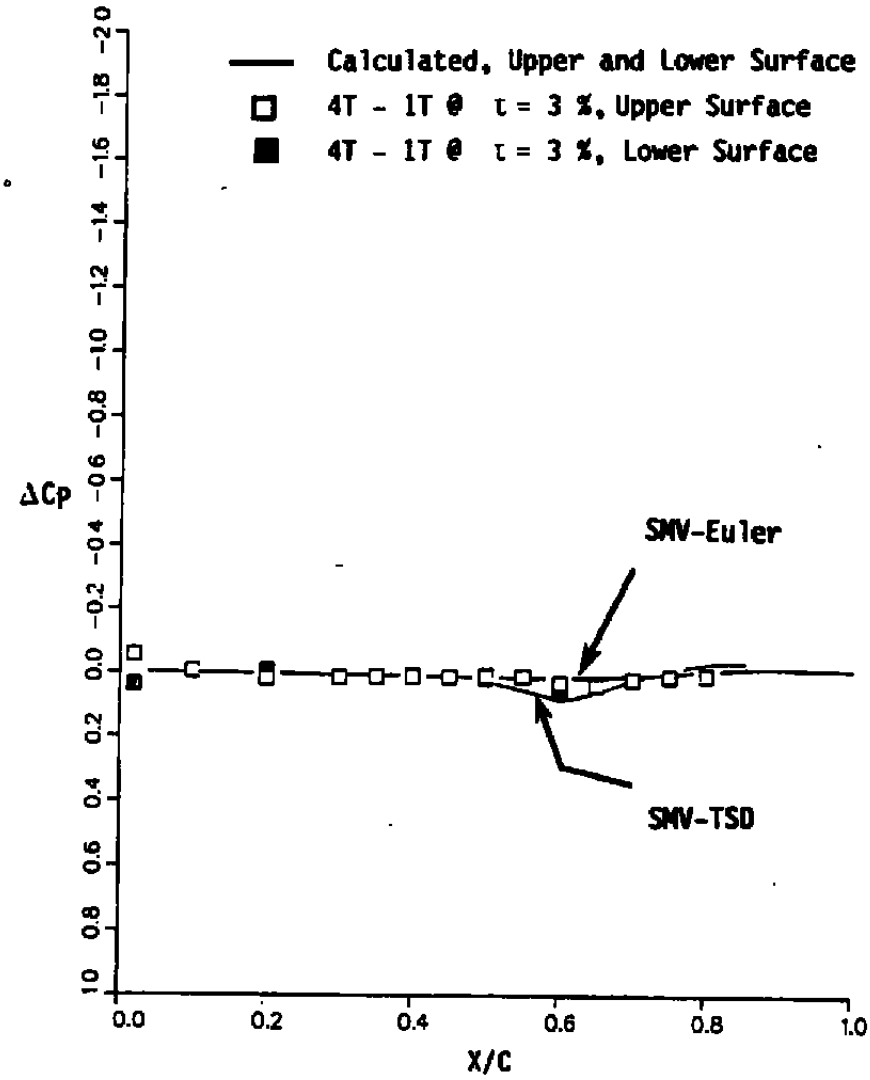

b. 60-percent tail semispan
Figure 17. Continued.

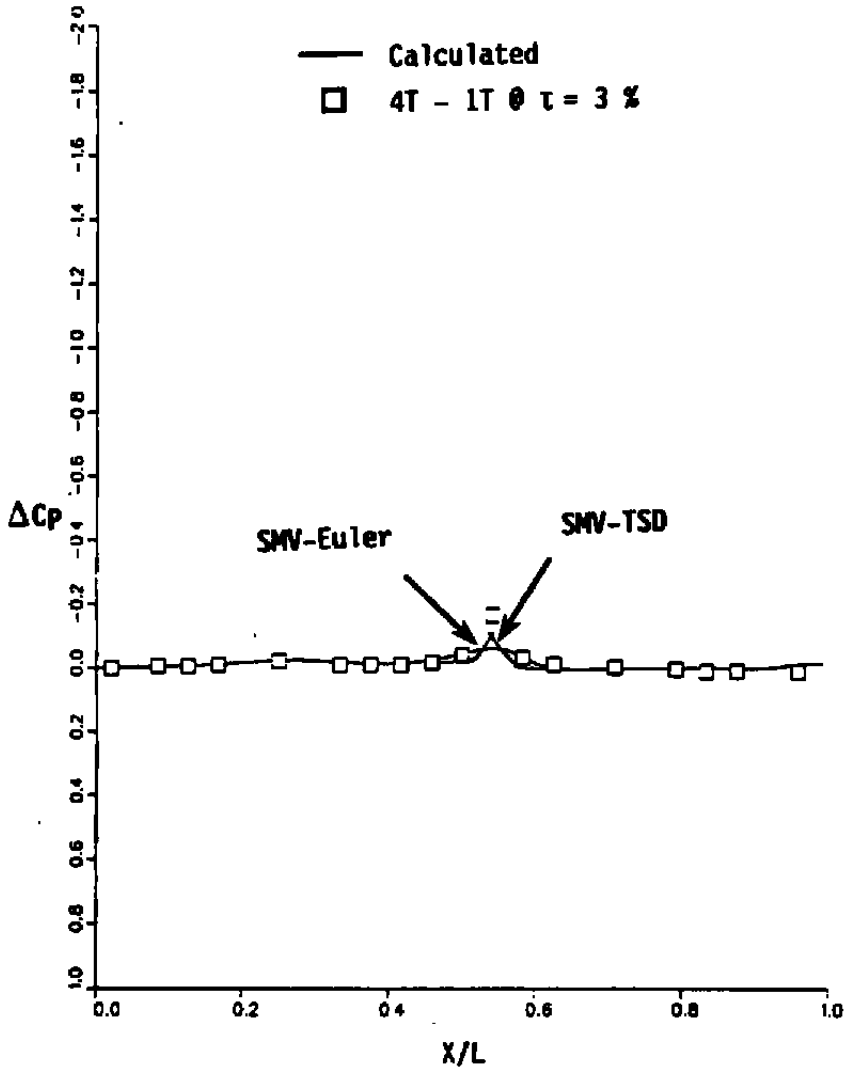

c. Fuselage top
Figure 17. Concluded.

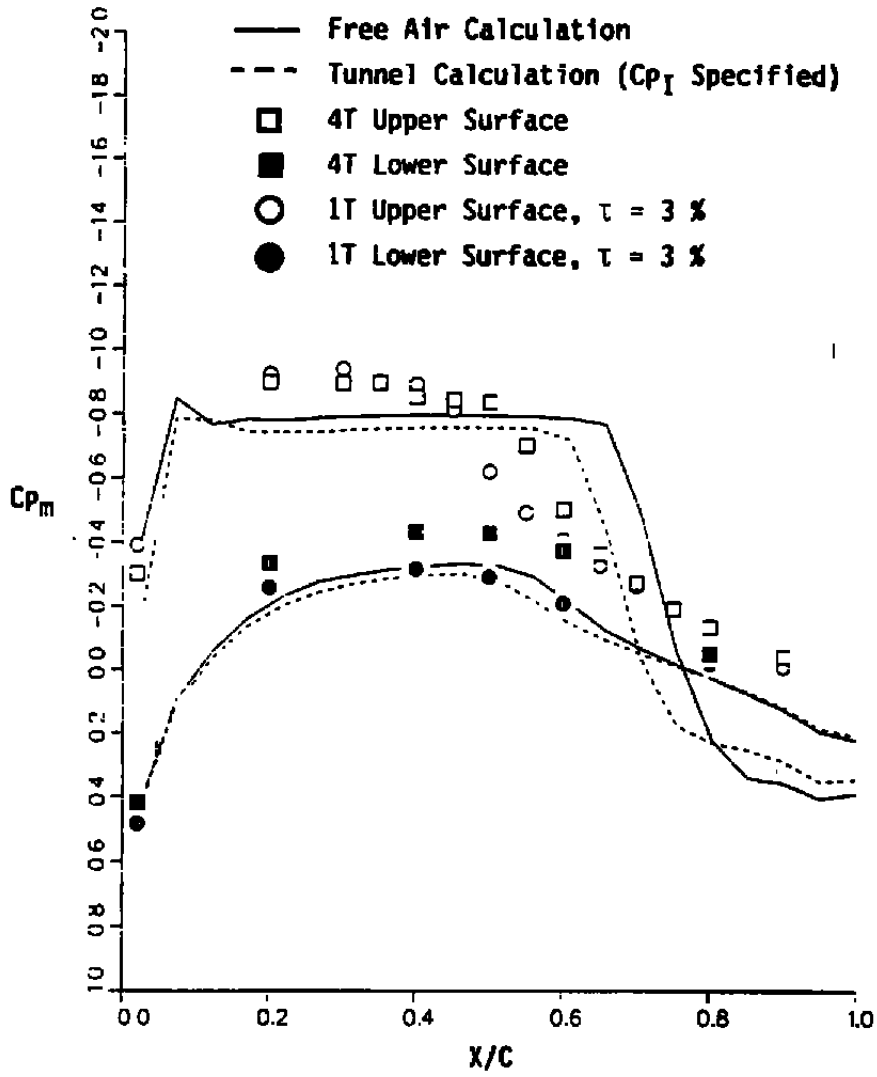

a. 60-percent wing semispan

Figure 18. Model pressures measured and calculated using the SMV-TSD Code, M_E = 0.90 and α_E = 4 deg.

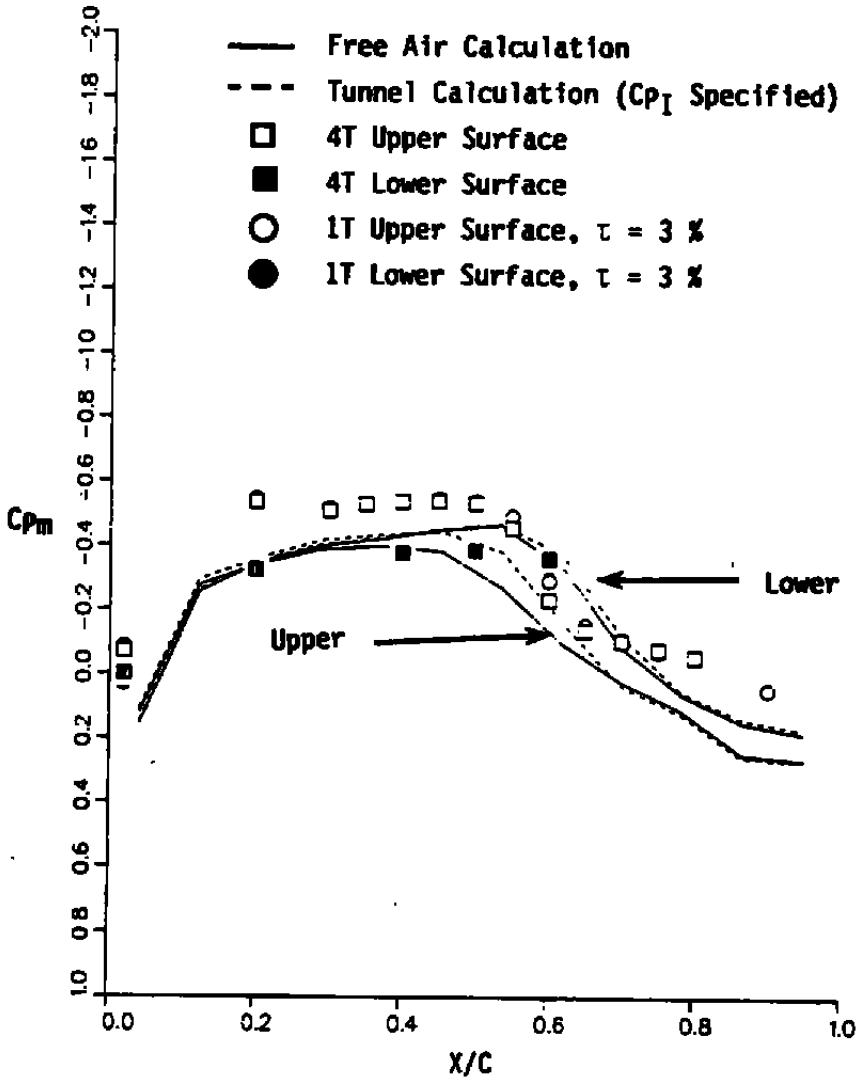

b. 60-percent tail semispan
Figure 18. Continued.

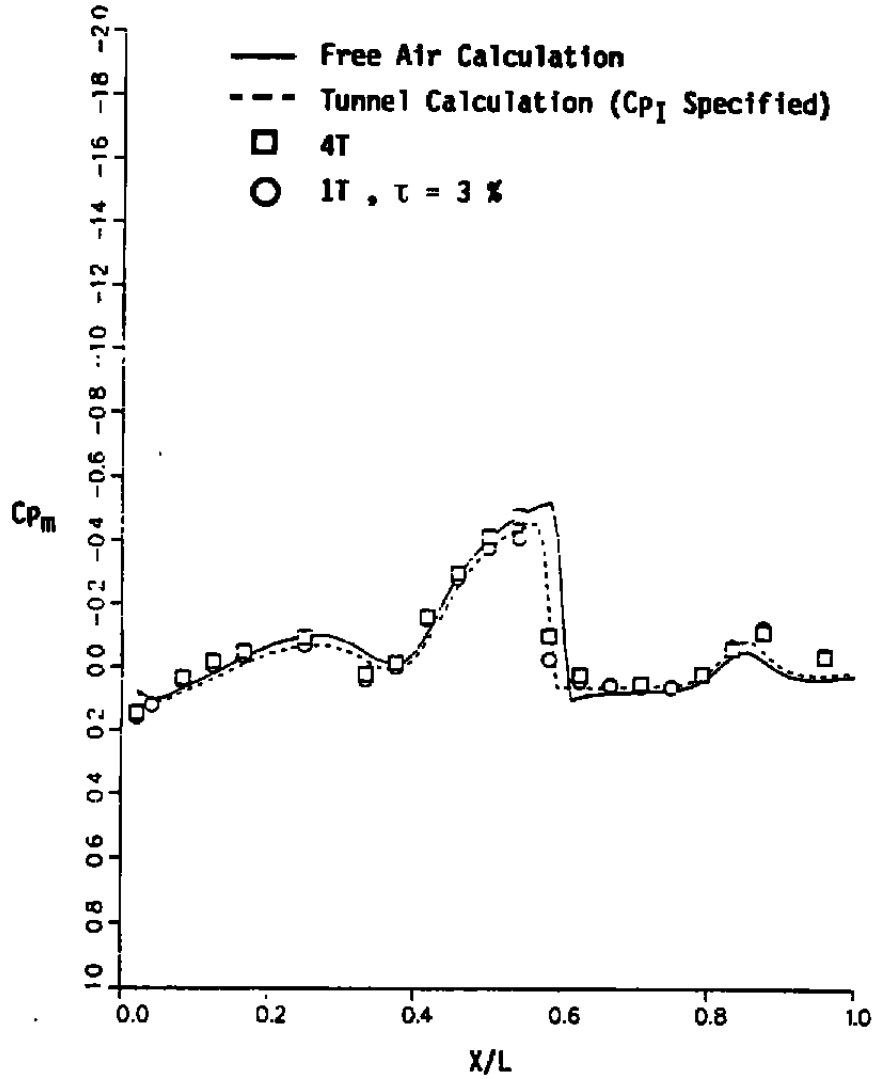

c. Fuselage top
Figure 18. Concluded.

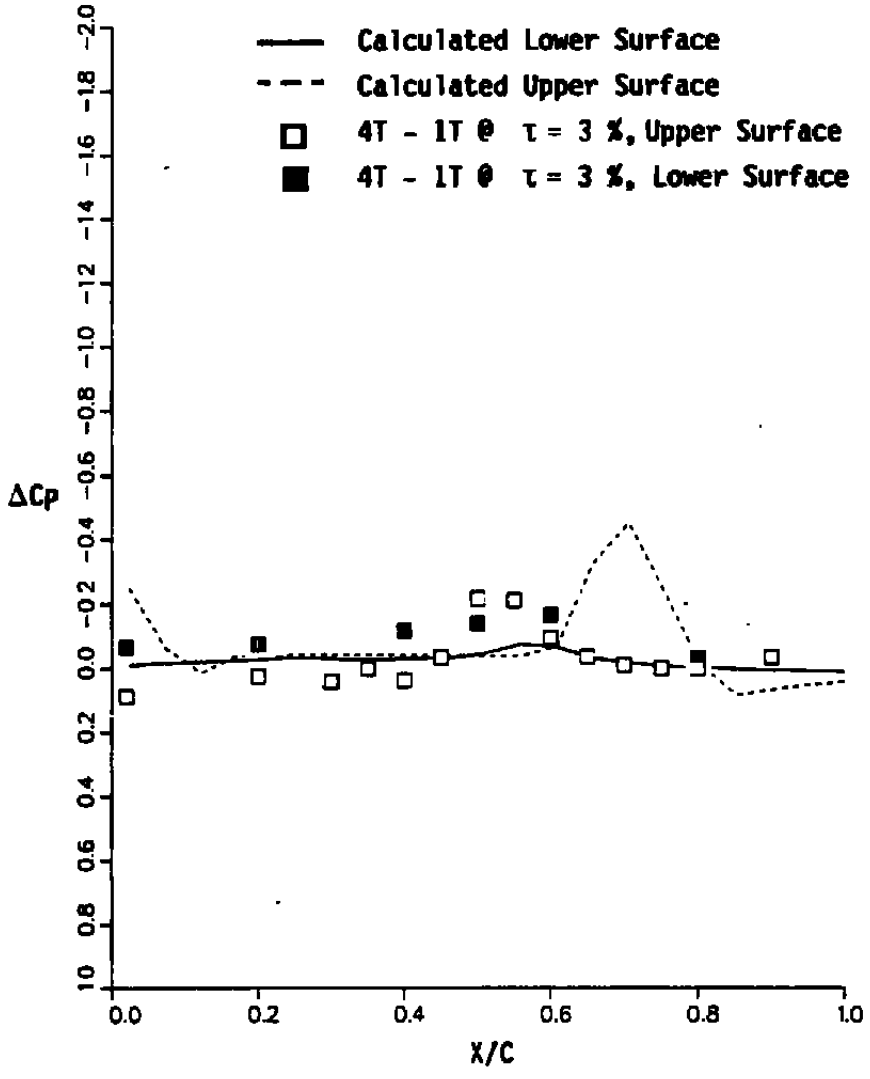

a. 60-percent wing semispan

Figure 19. Model local corrections measured and calculated using the SMV-TSD Code, M_E = 0.90 and α_E = 4 deg.

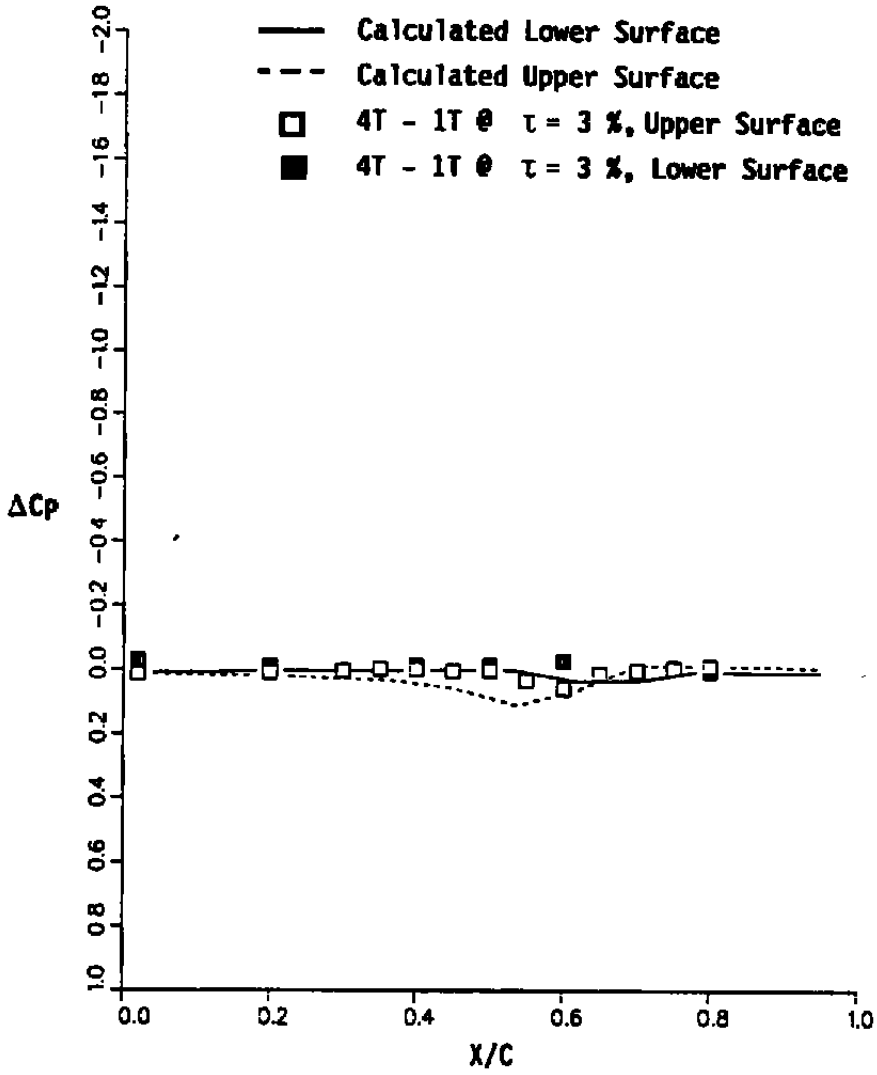

b. 60-percent tail semispan
Figure 19. Continued.

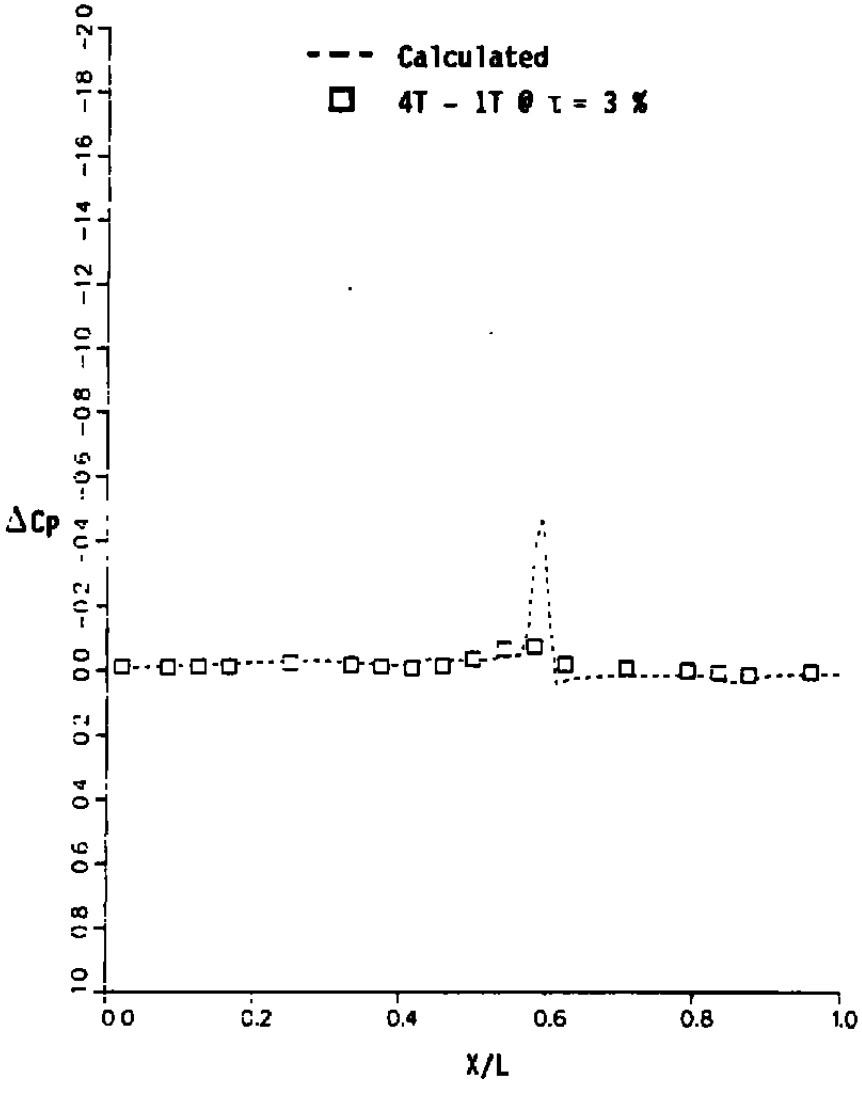

c. Fuselage top
Figure 19. Concluded.

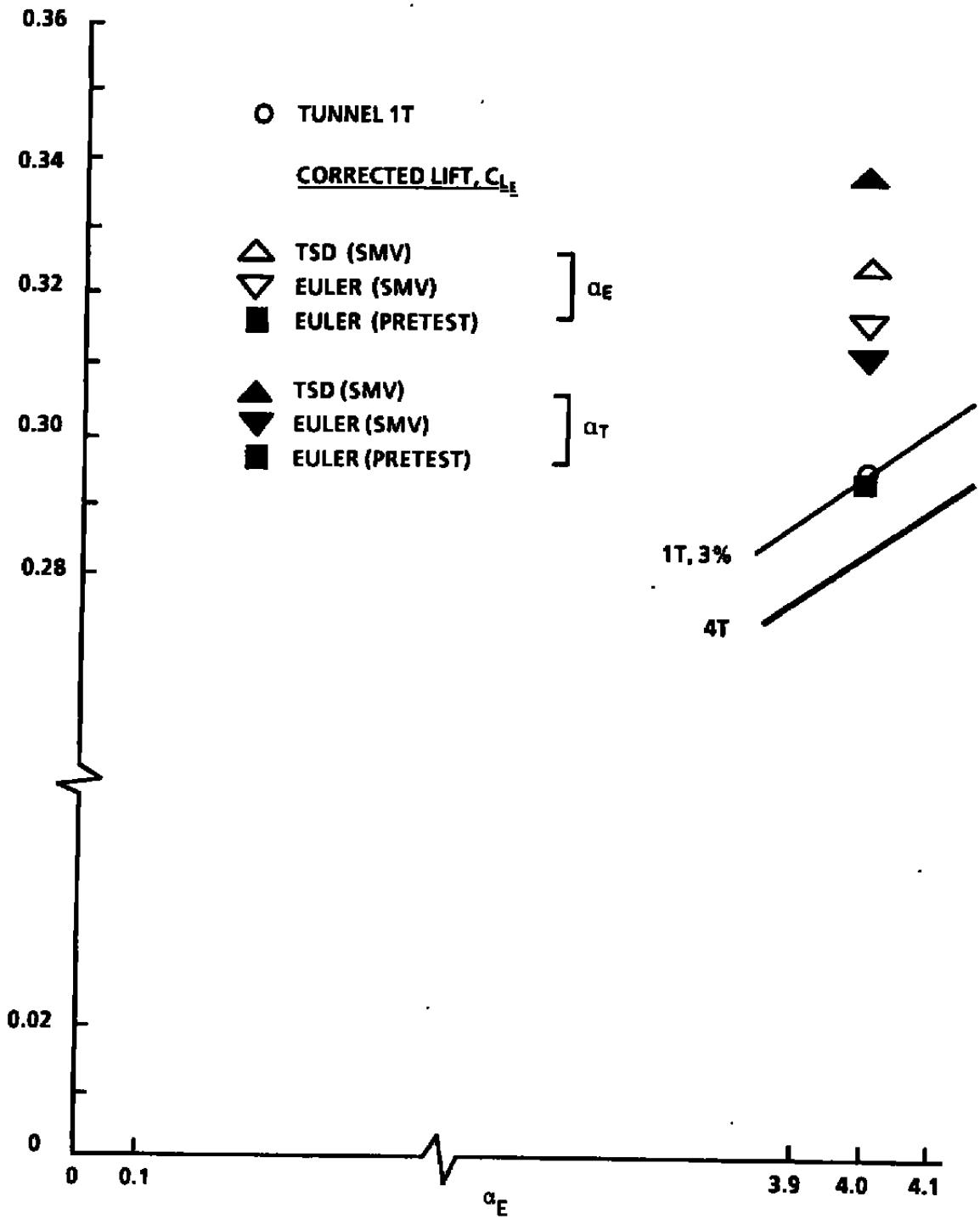

Figure 20. Corrected lift coefficient at α_E and α_T using the SMV-TSD, SMV-Euler, and Pretest-Euler Codes for M_E = 0.90.

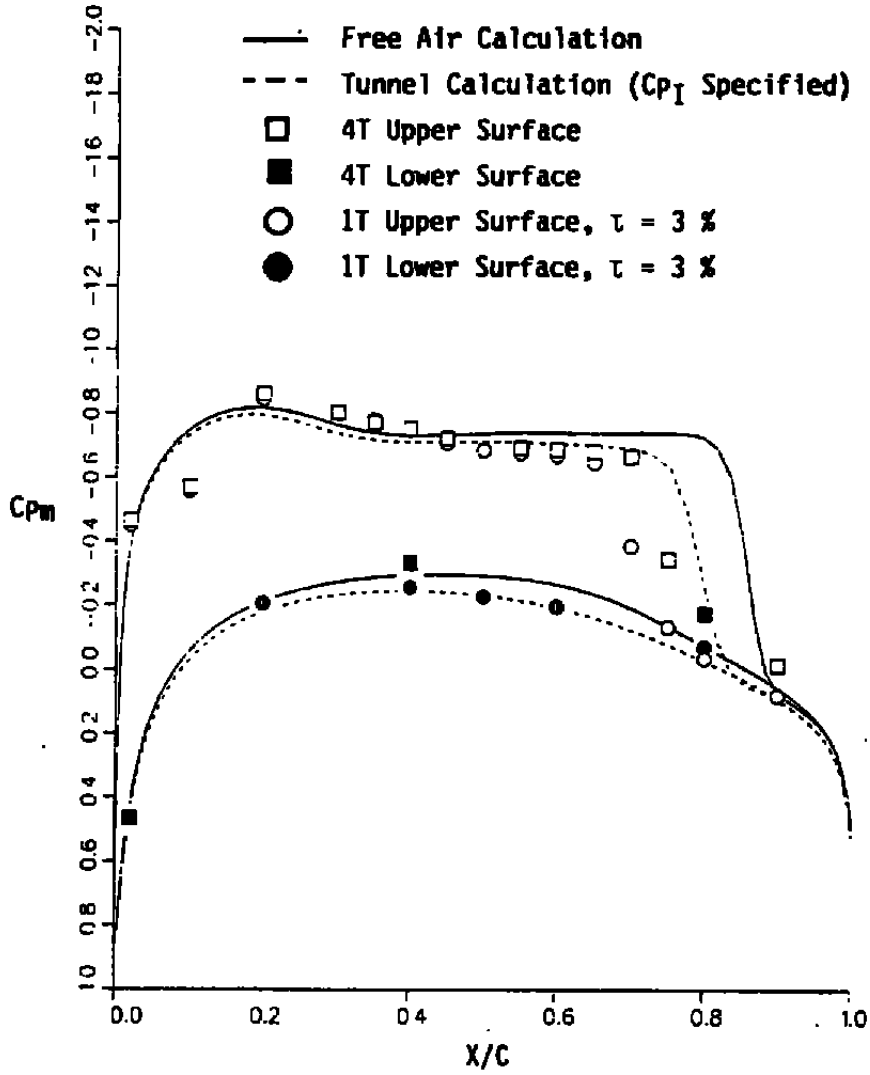

a. −40-percent wing semispan

Figure 21. Model pressures measured and calculated using the SMV-Euler Code, $M_E = 0.90$ and $\alpha_E = 4$ deg.

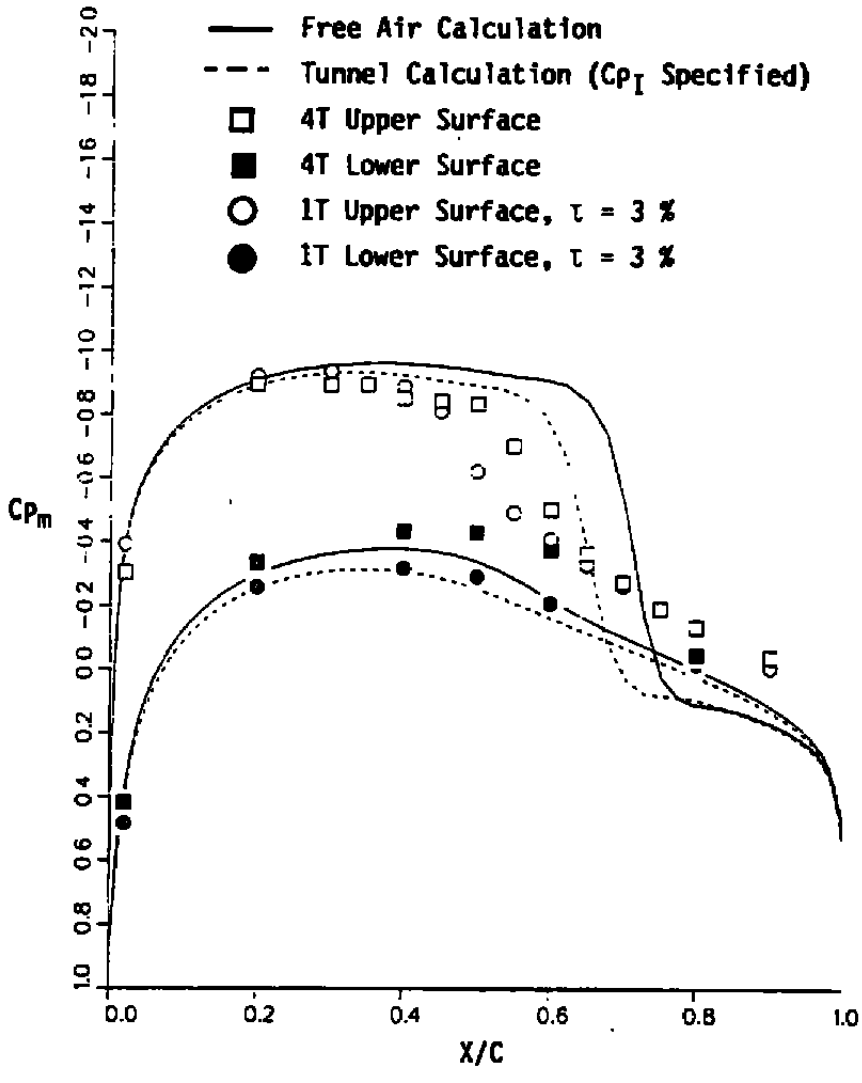

b. 60-percent wing semispan
Figure 21. Continued.

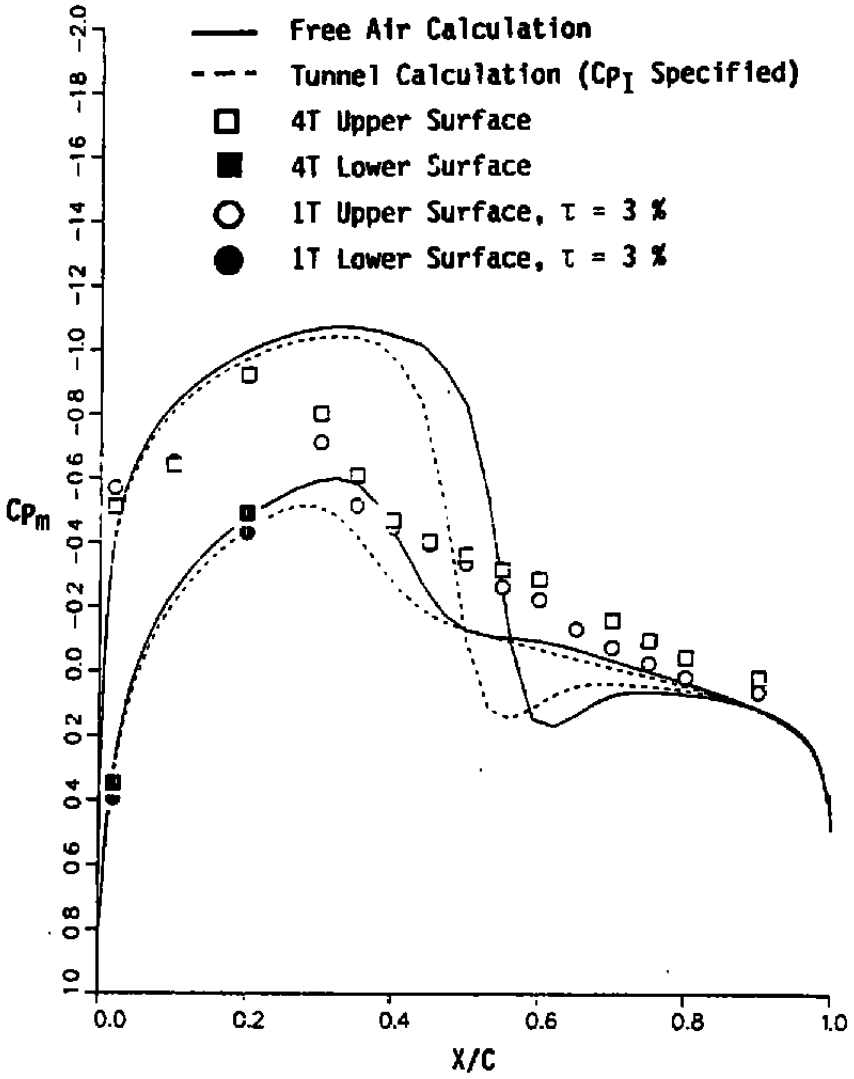

c. −90-percent wing semispan
Figure 21. Continued.

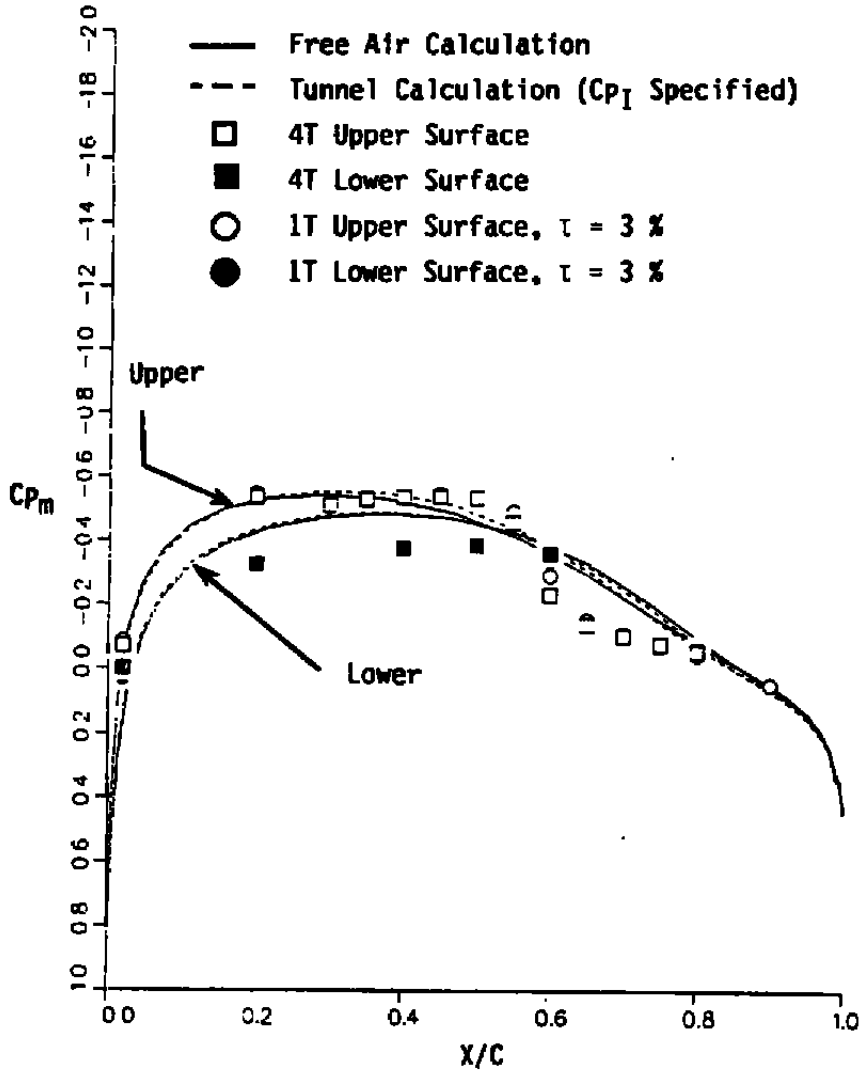

d. 60-percent tail semispan
Figure 21. Continued.

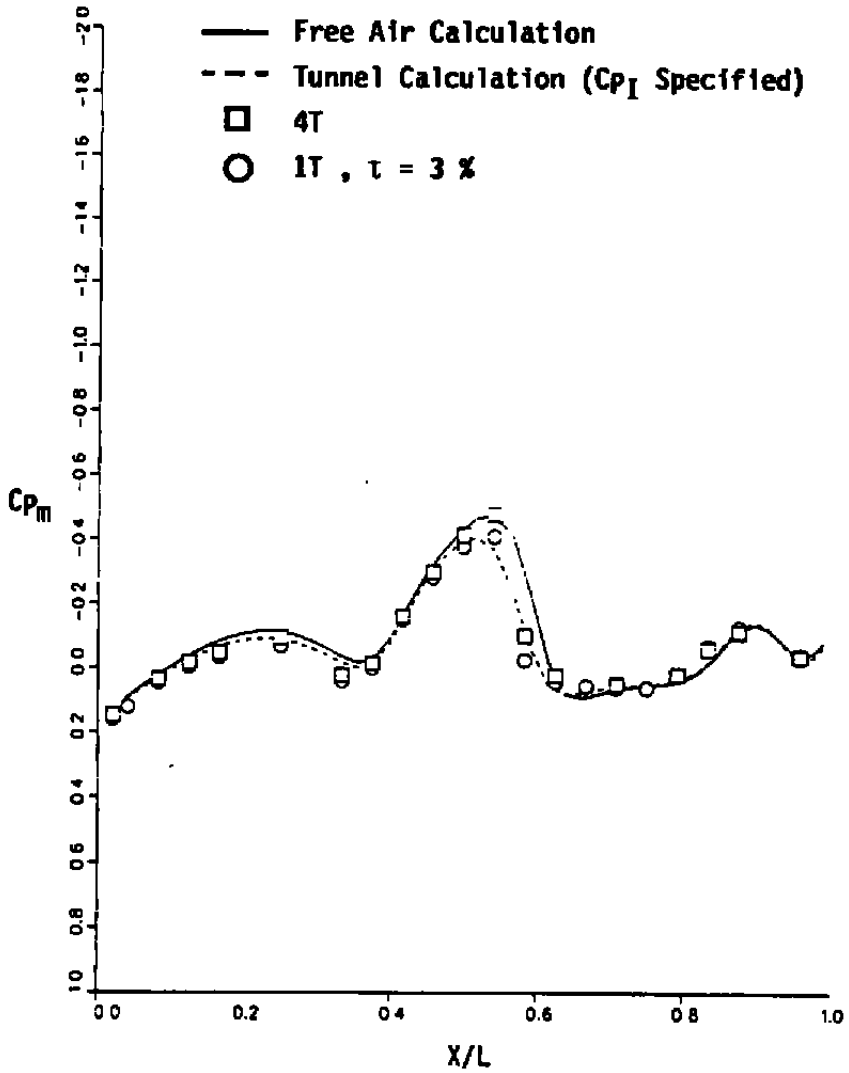

e. Fuselage top
Figure 21. Concluded.

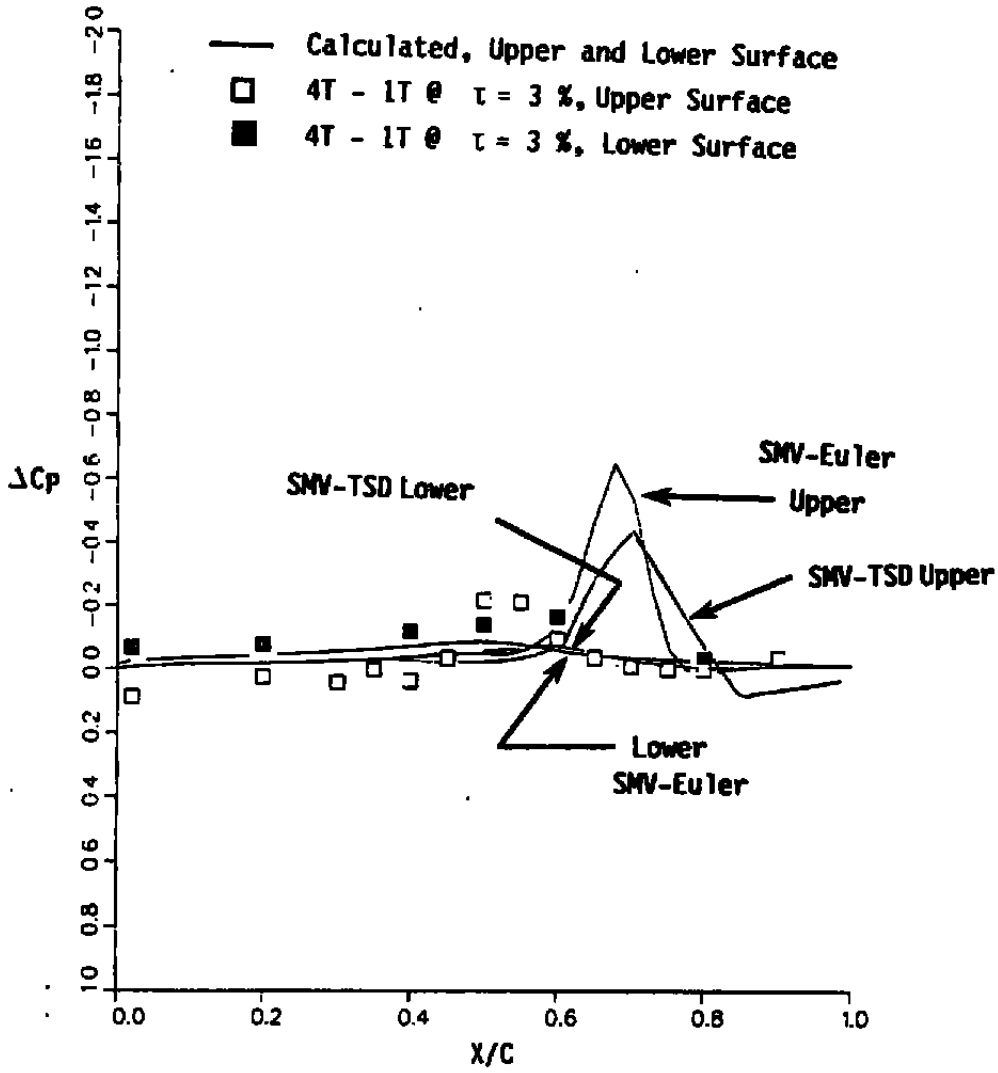

a. 60-percent wing semispan

Figure 22. Model local corrections measured and calculated using the SMV-Euler and SMV-TSD Codes, M_E = 0.90 and α_E = 4 deg.

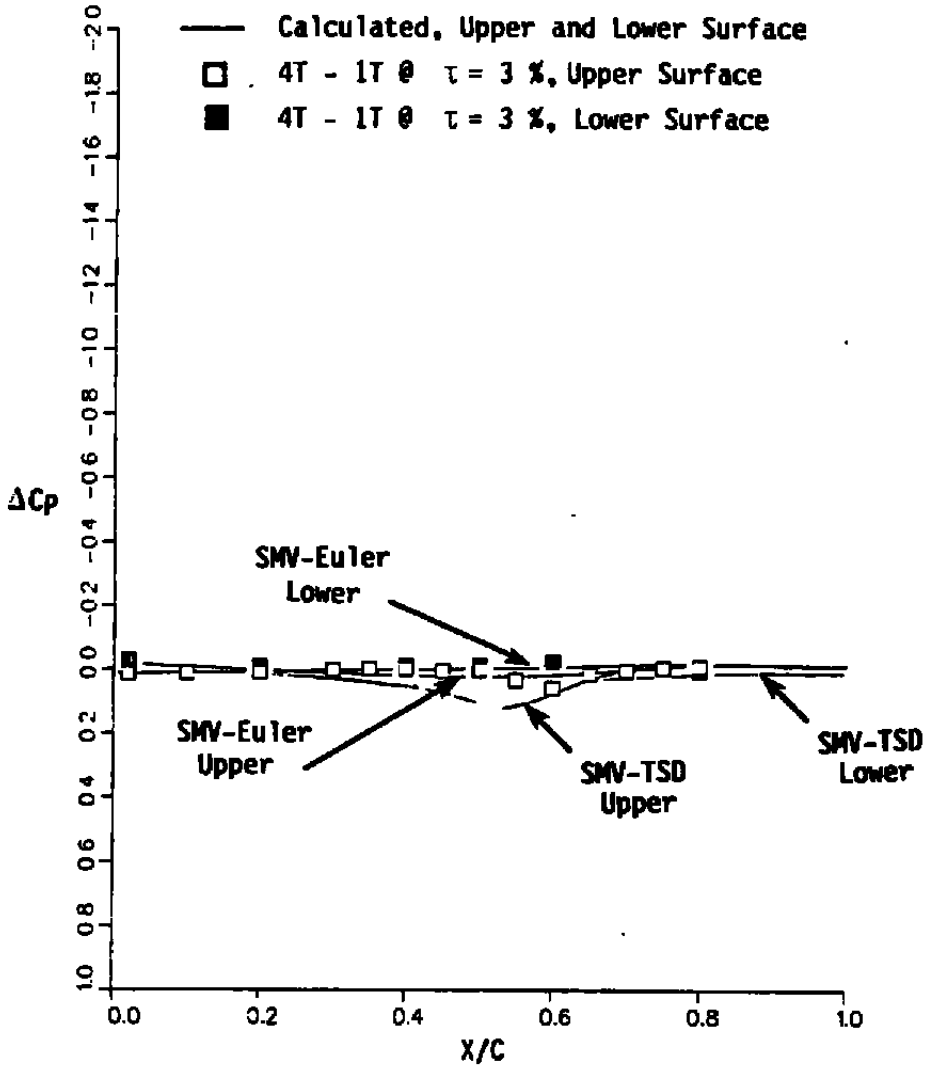

b. 60-percent tail semispan
Figure 22. Continued.

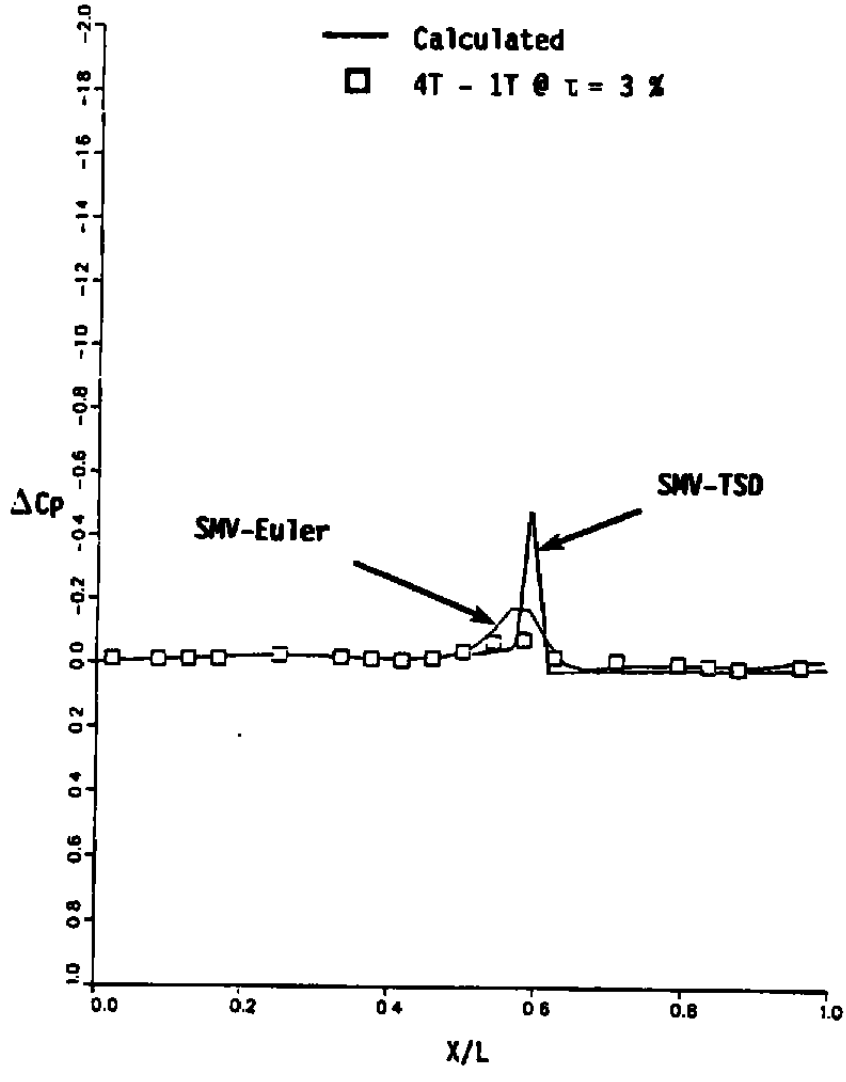

c. Fuselage top
Figure 22. Concluded.

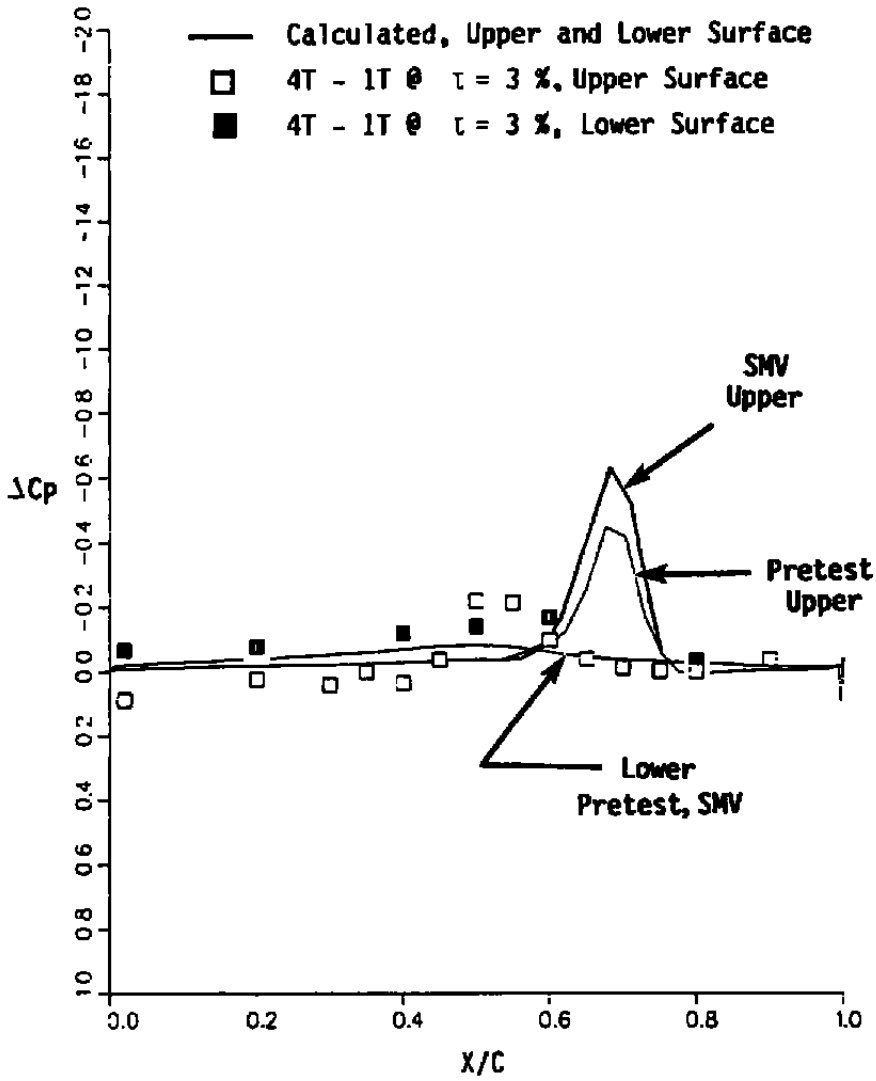

a. 60-percent wing semispan

Figure 23. Model local correctons measured and calculated using the Pretest-Euler and SMV-Euler Codes, M_E = 0.90 and α_E = 4 deg.

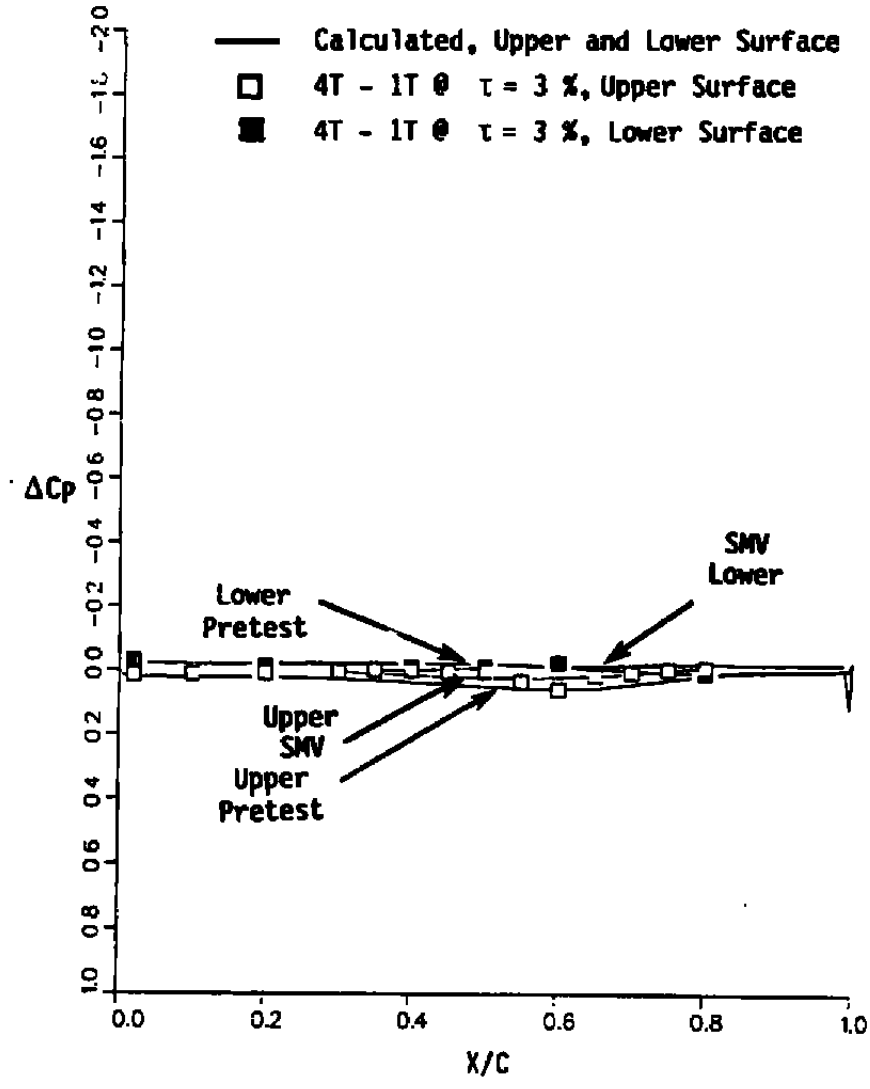

b. 60-percent tail semispan
Figure 23. Continued.

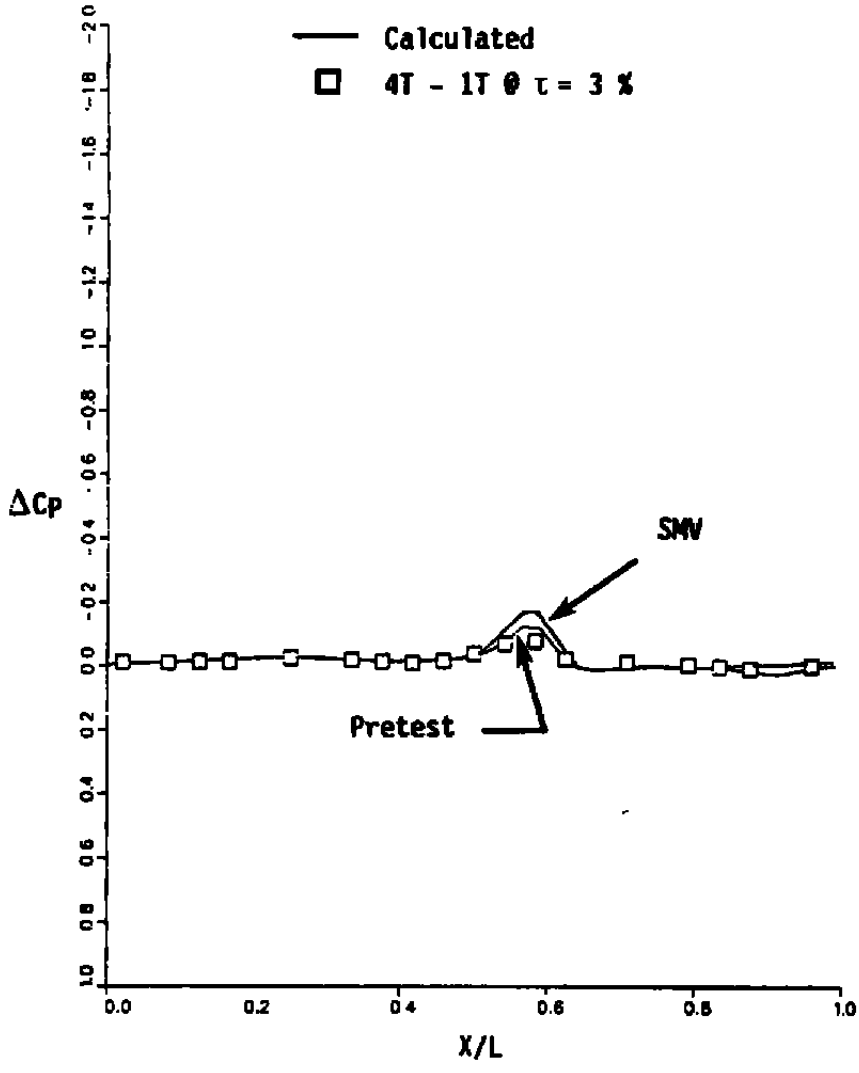

c. Fuselage top
Figure 23. Concluded.

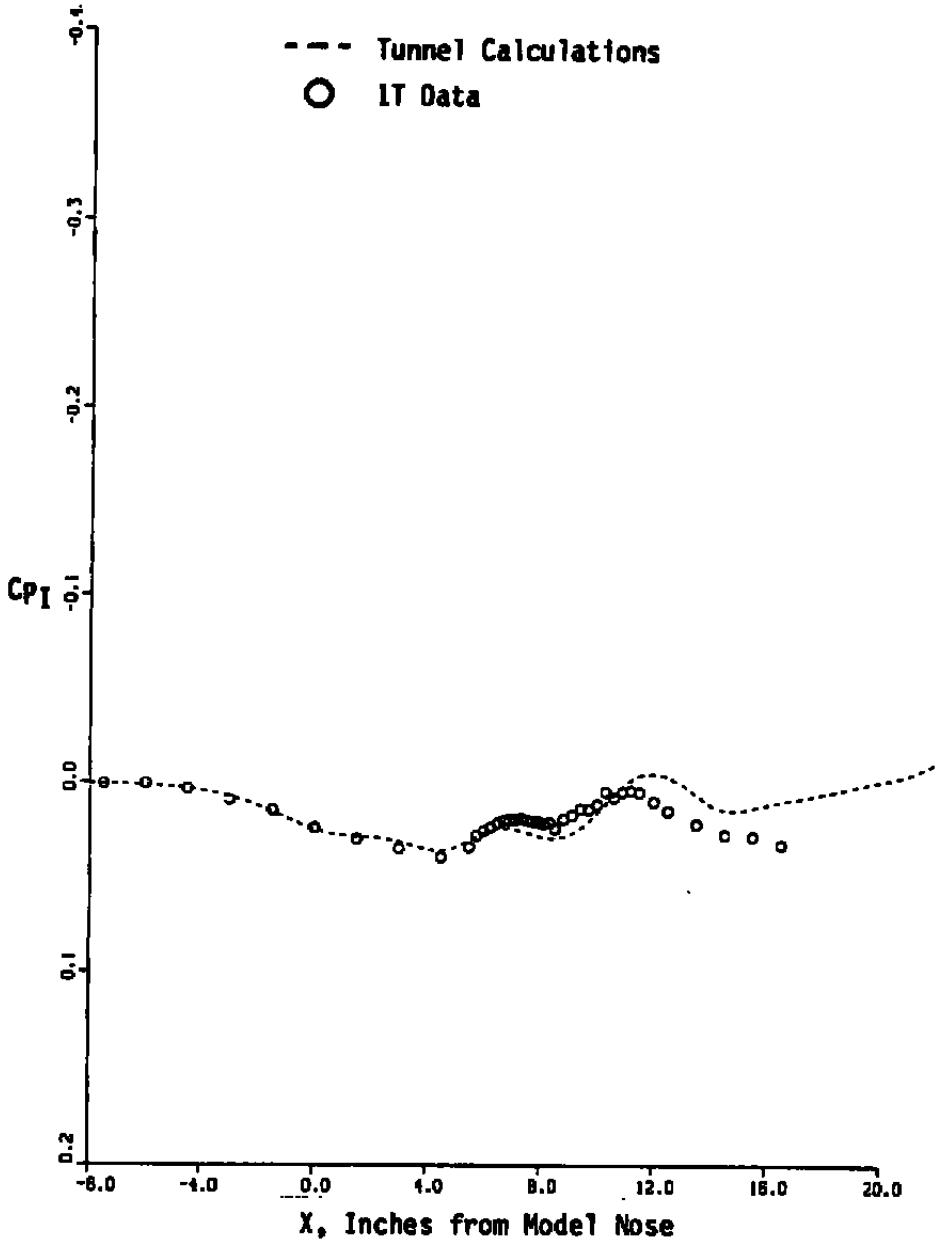

a. θ_p = 15 deg

Figure 24. Interface pressures measured and calculated using the Pretest-Euler Code, M_E = 0.90, α_E = 4 deg, and τ = 3 percent.

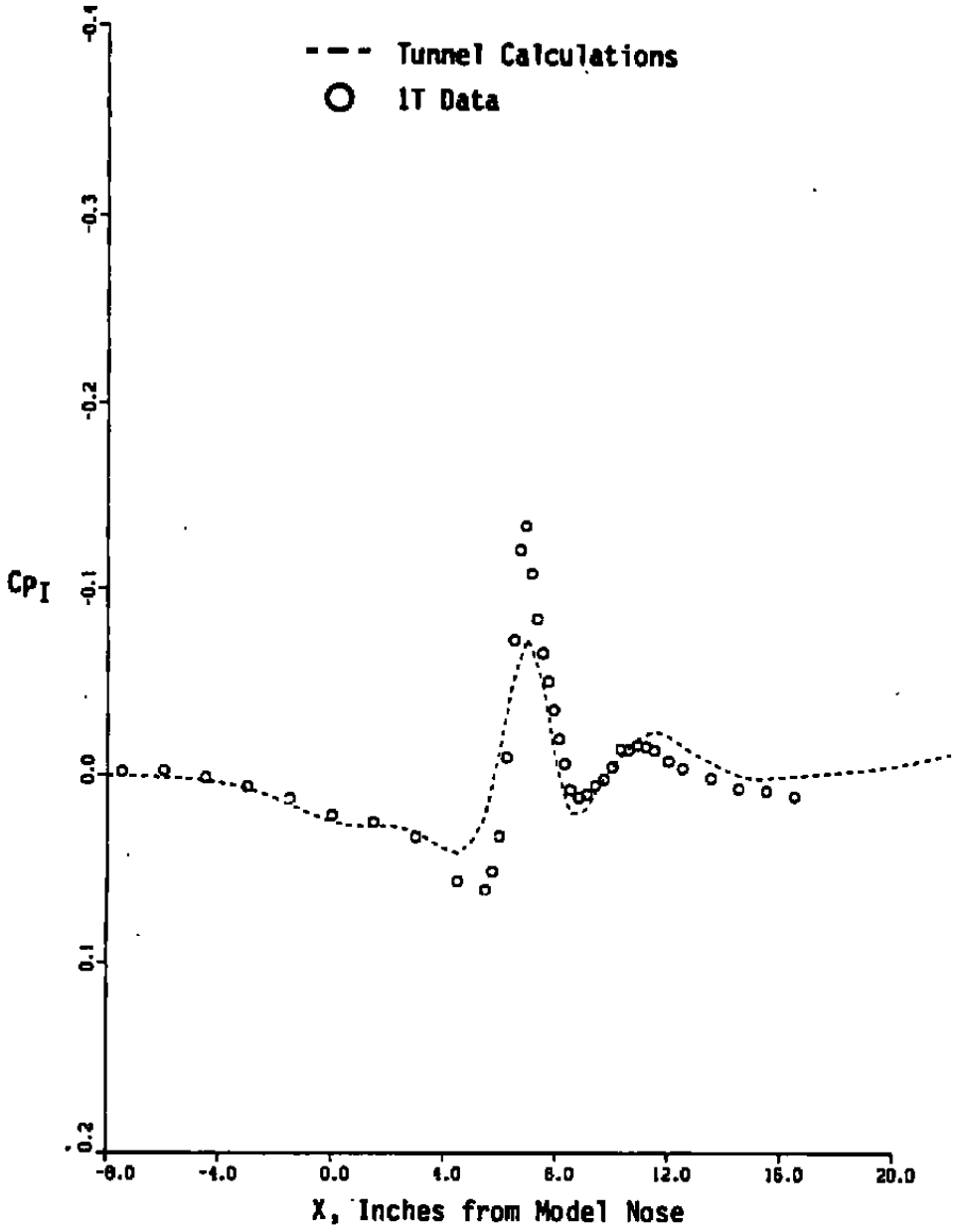

b. θ_p = 85 deg
Figure 24. Continued.

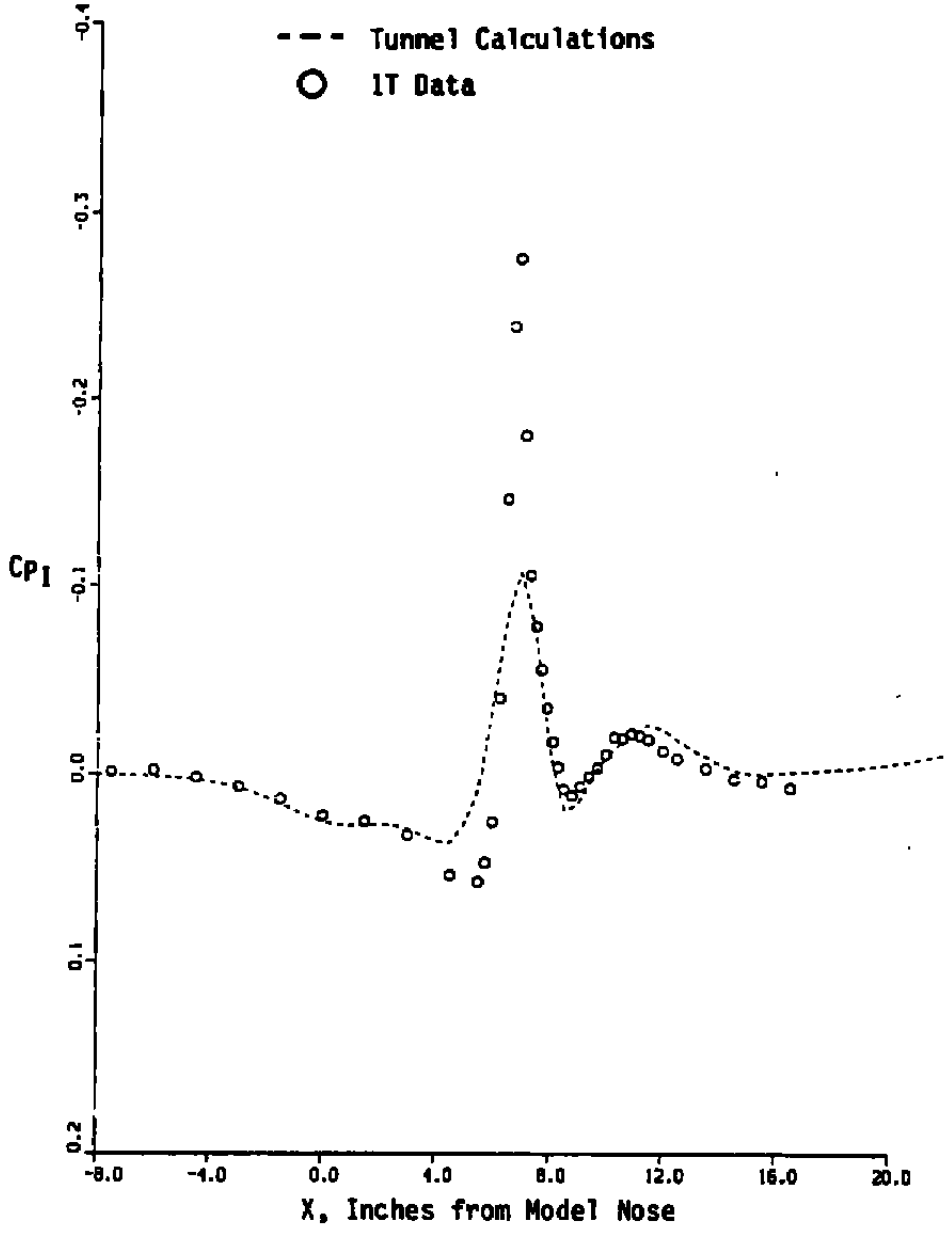

c. θ_p = 95 deg
Figure 24. Continued.

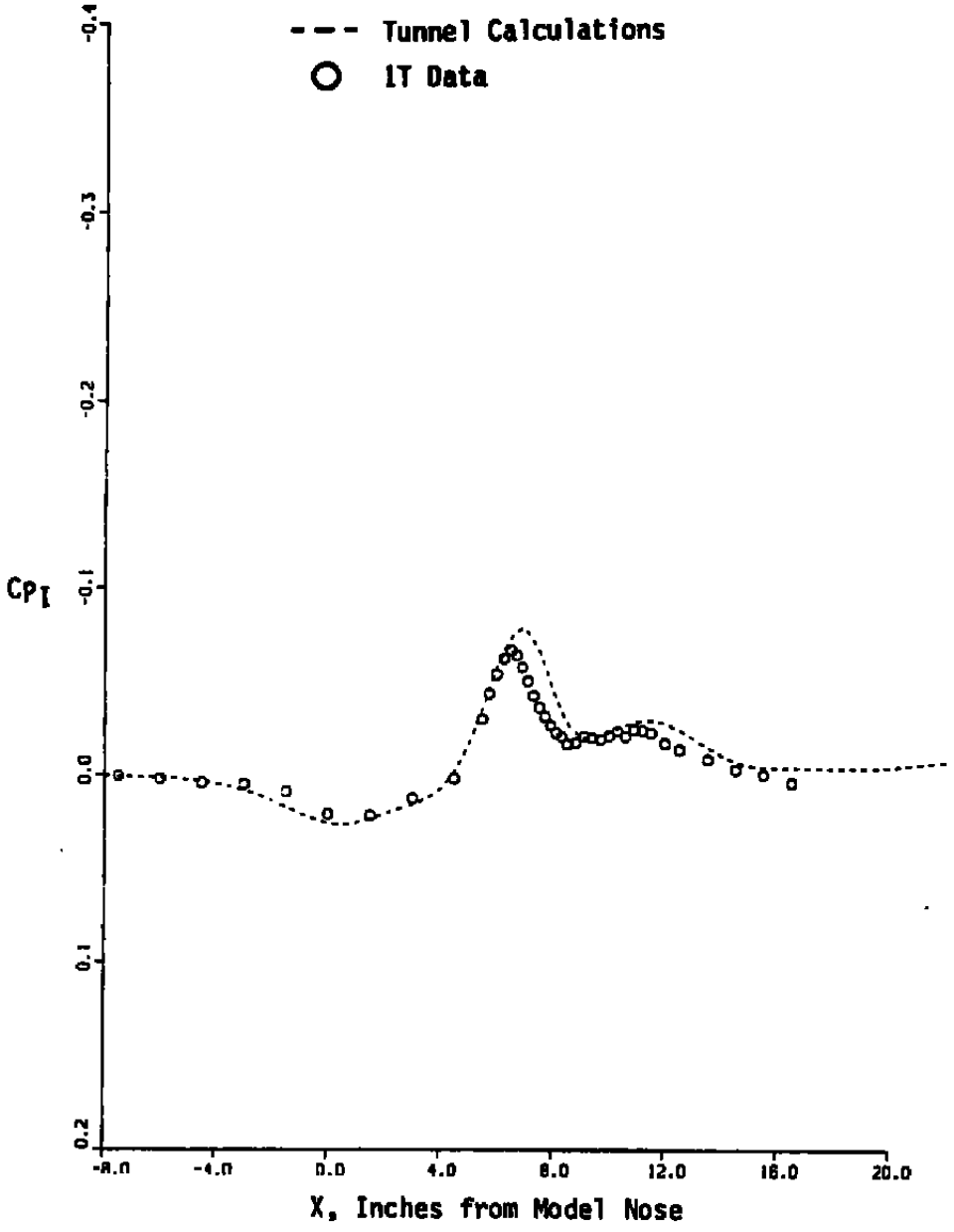

d. θ_p = 165 deg
Figure 24. Concluded.

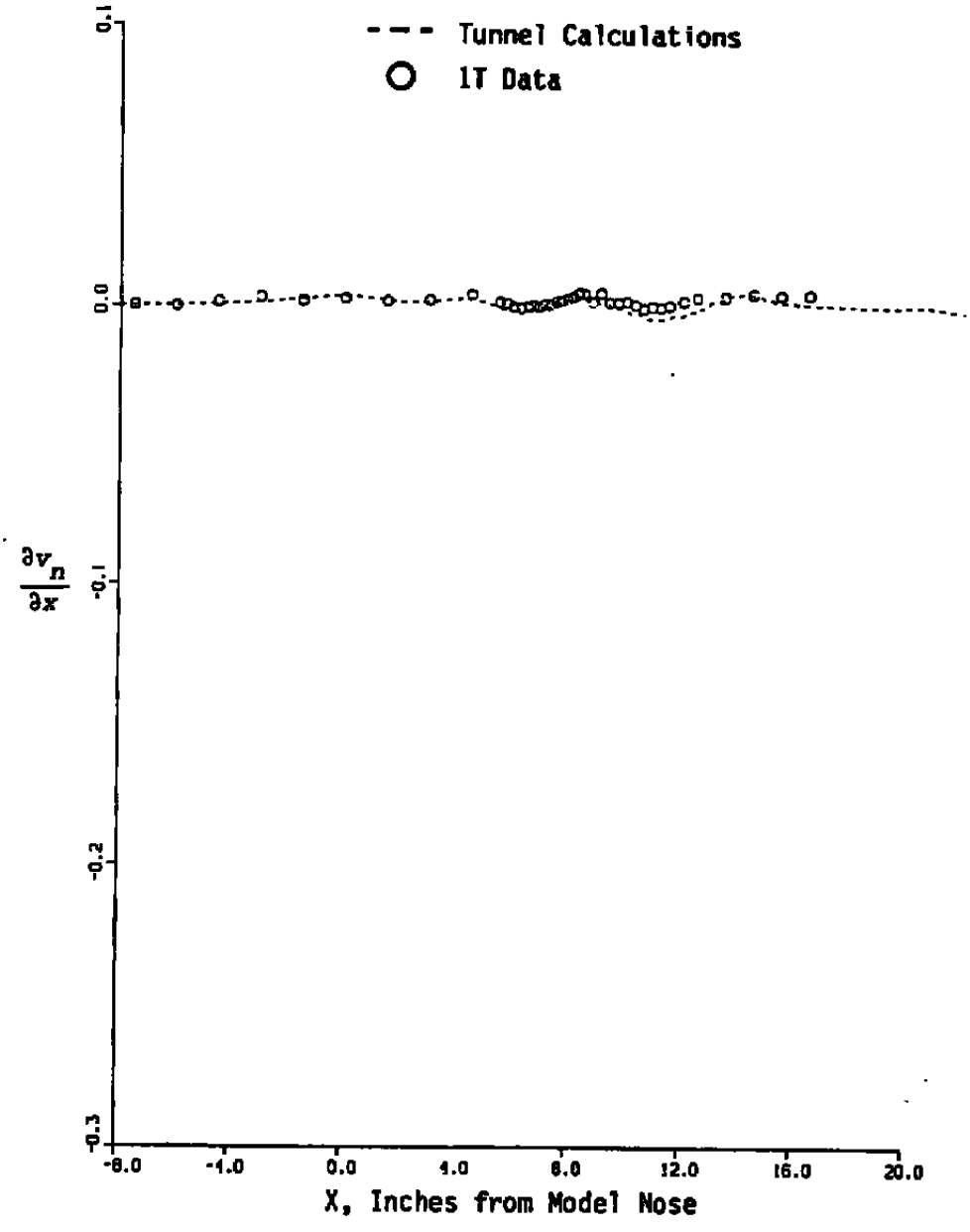

a. θ_p = 15 deg

Figure 25. Interface $\partial v_n/\partial x$ measured and calculated using the Pretest-Euler Code, M_E = 0.90, α_E = 4 deg, and τ = 3 percent.

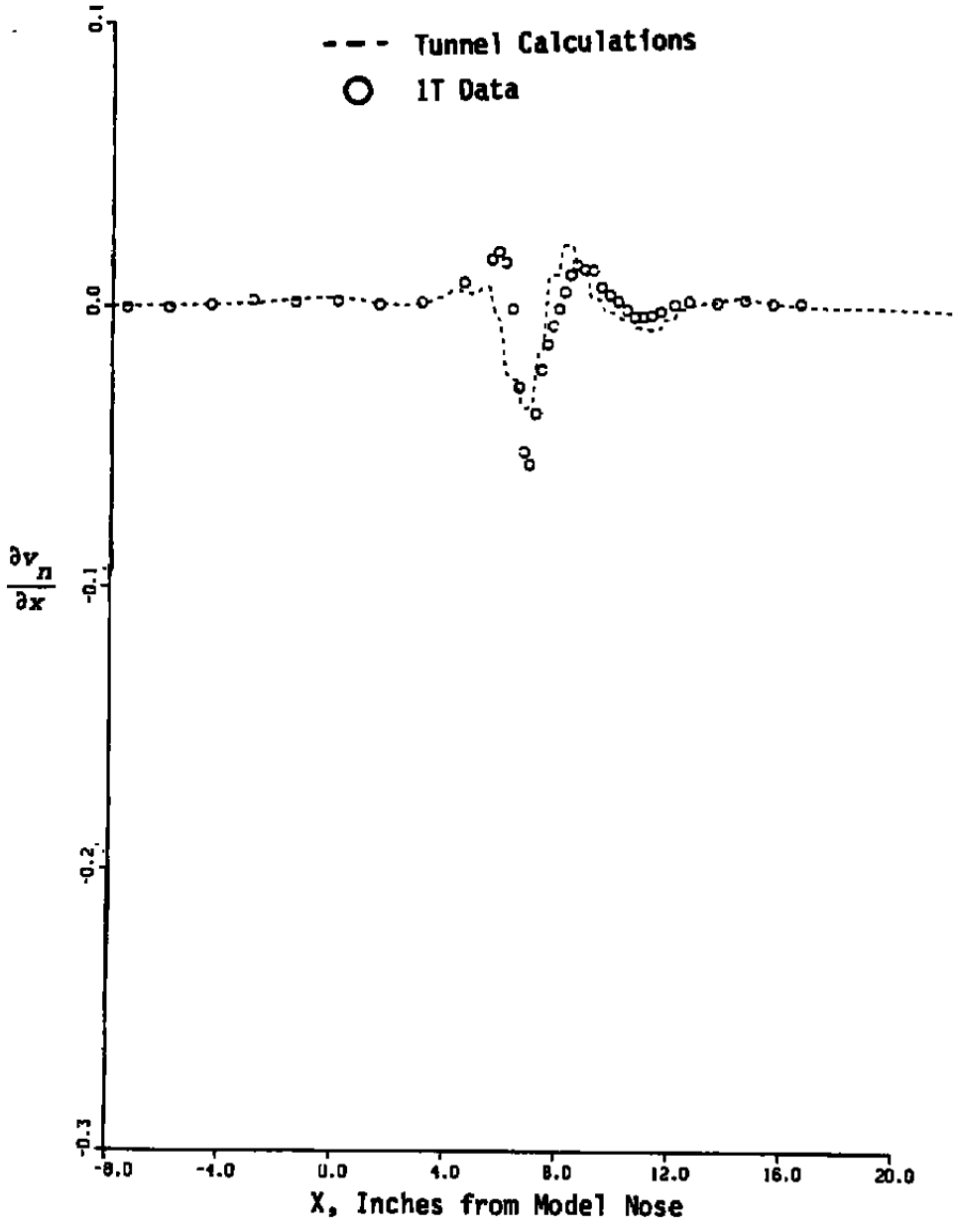

b. θ_p = 85 deg
Figure 25. Continued.

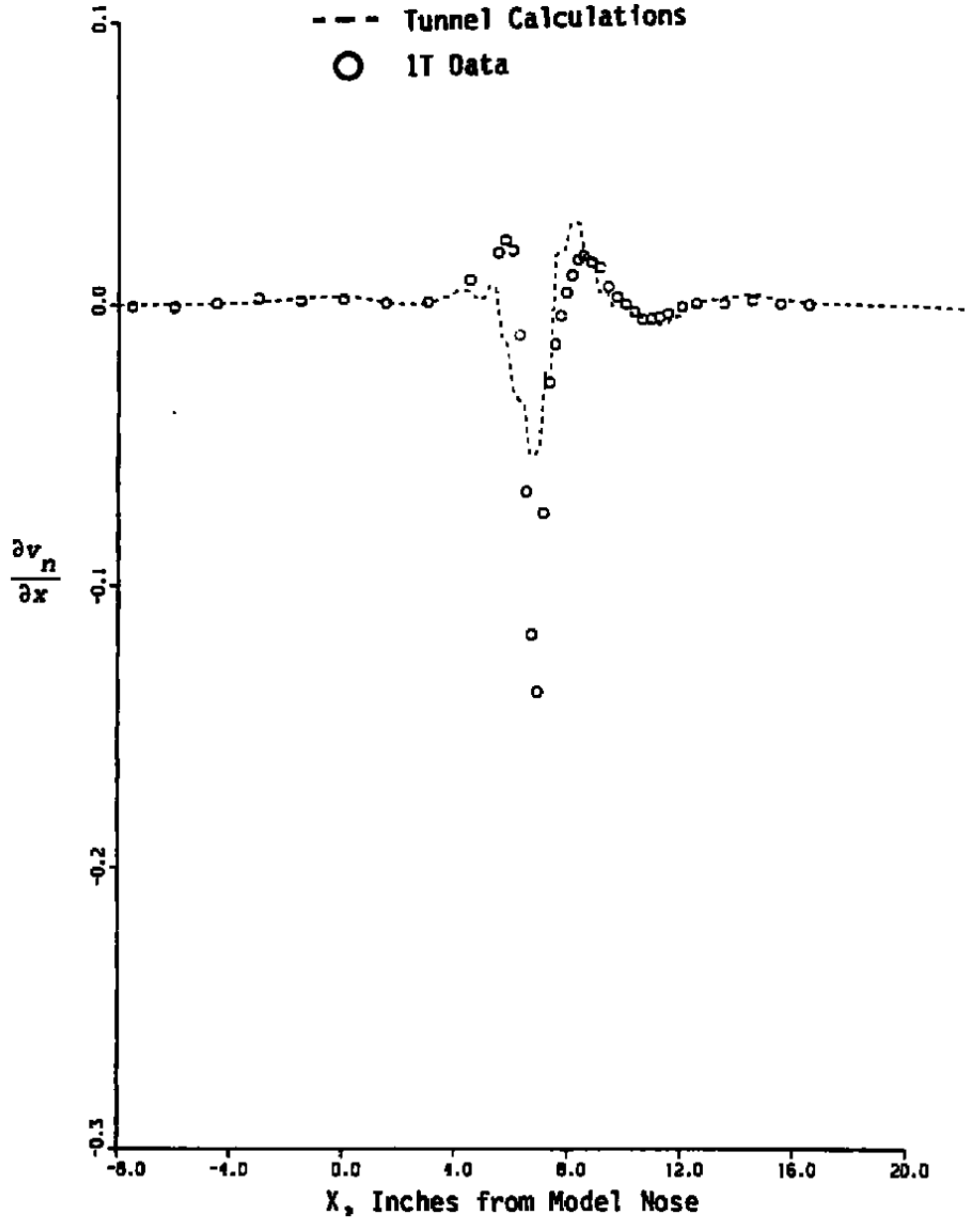

c. θ_p = 95 deg
Figure 25. Continued.

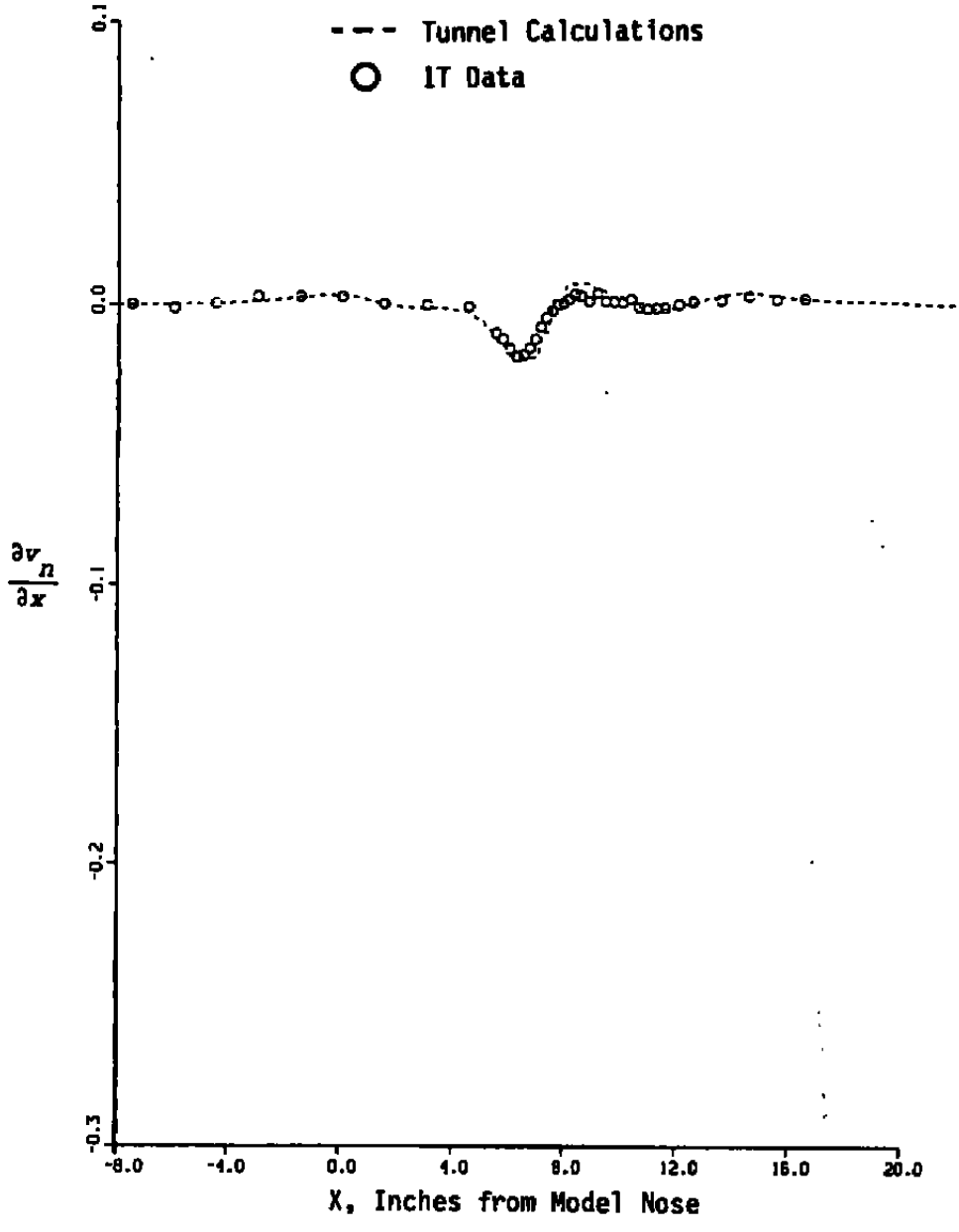

d. θ_p = 165 deg
Figure 25. Concluded.

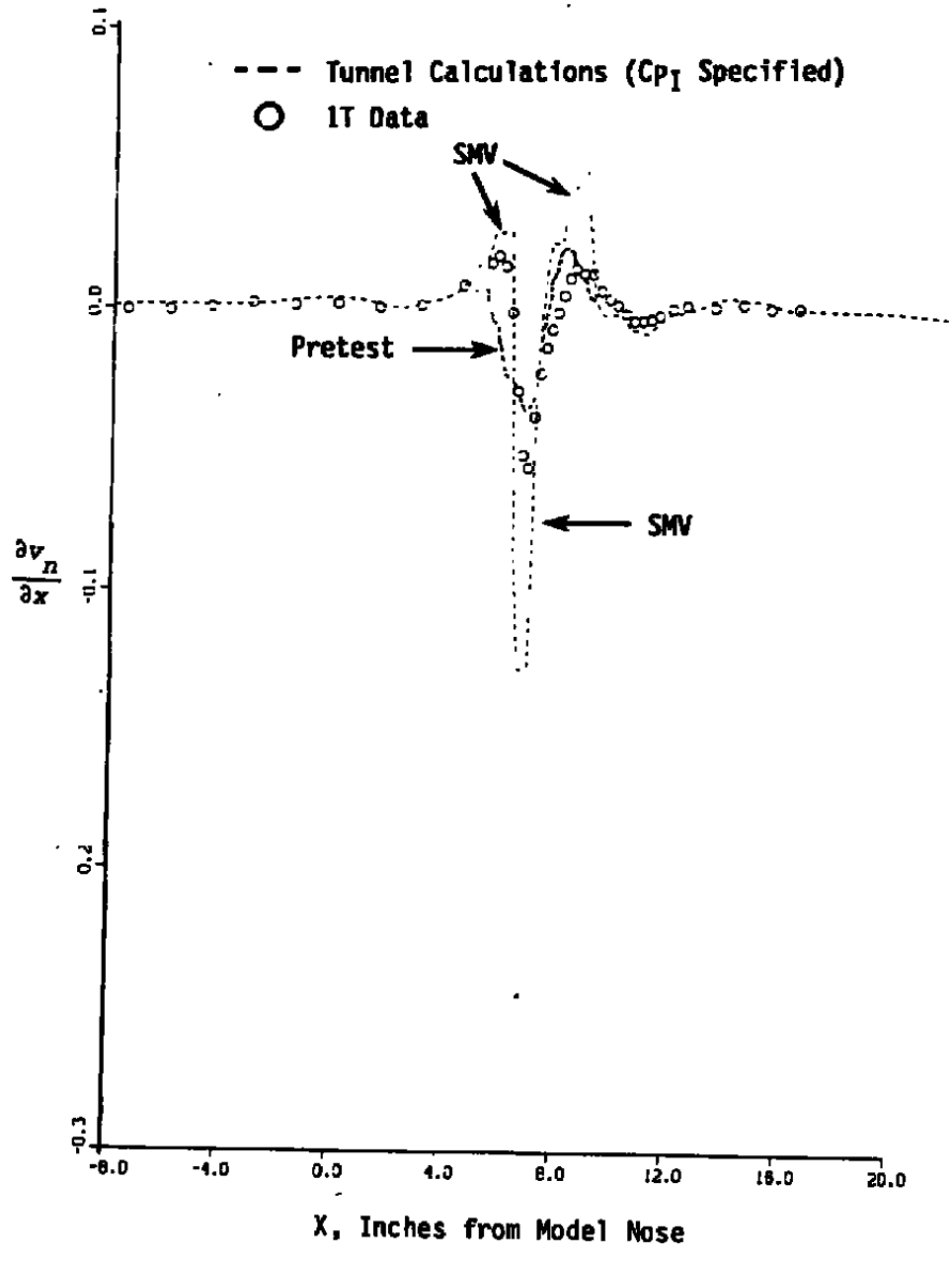

a. θ_p = 85 deg

Figure 26. Interface $\partial v_n/\partial x$ measured and calculated using the SMV-Euler and Pretest-Euler Codes, M_E = 0.90, α_E = 4 deg, and τ = 3 percent.

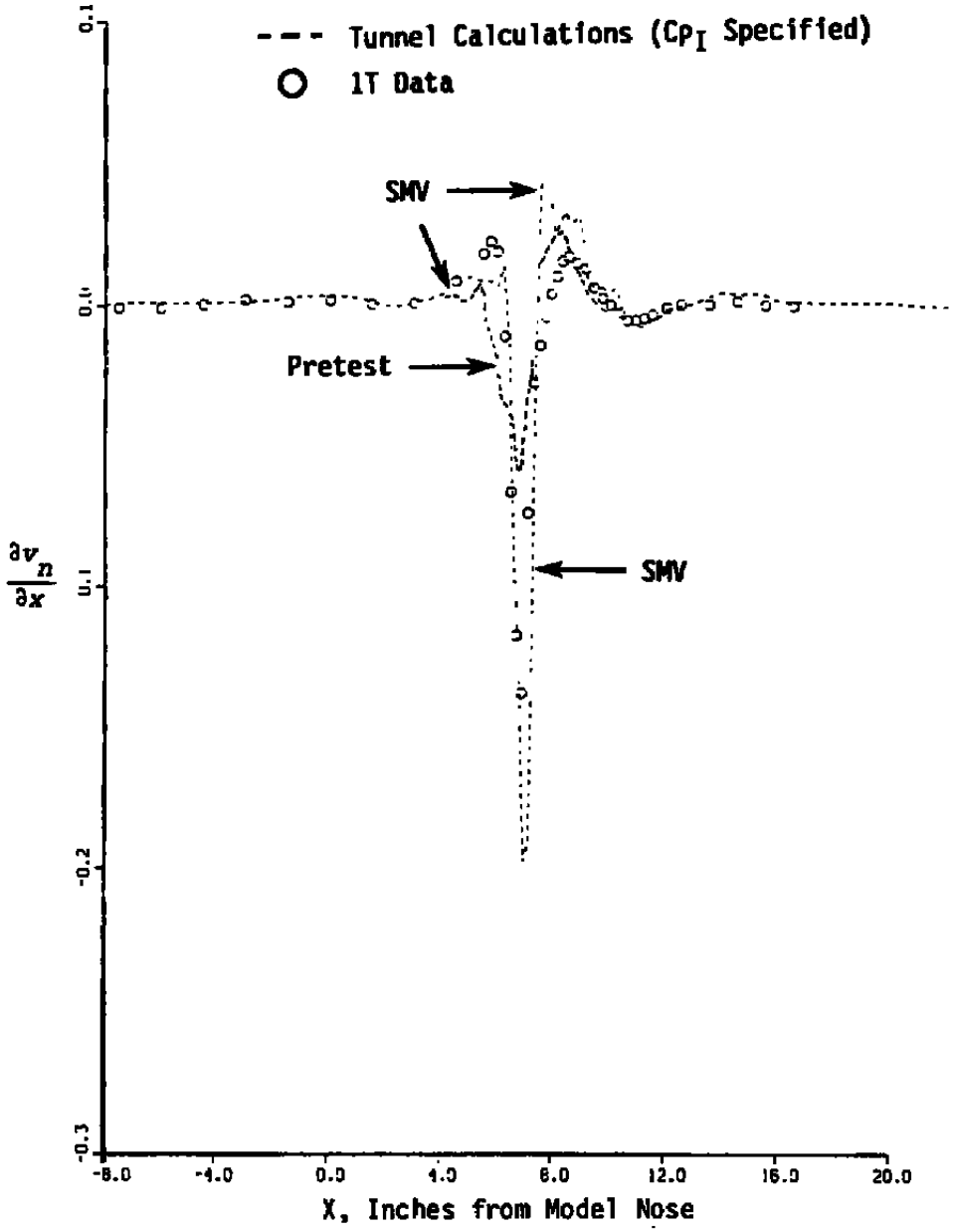

b. θ_p = 95 deg
Figure 26. Concluded.

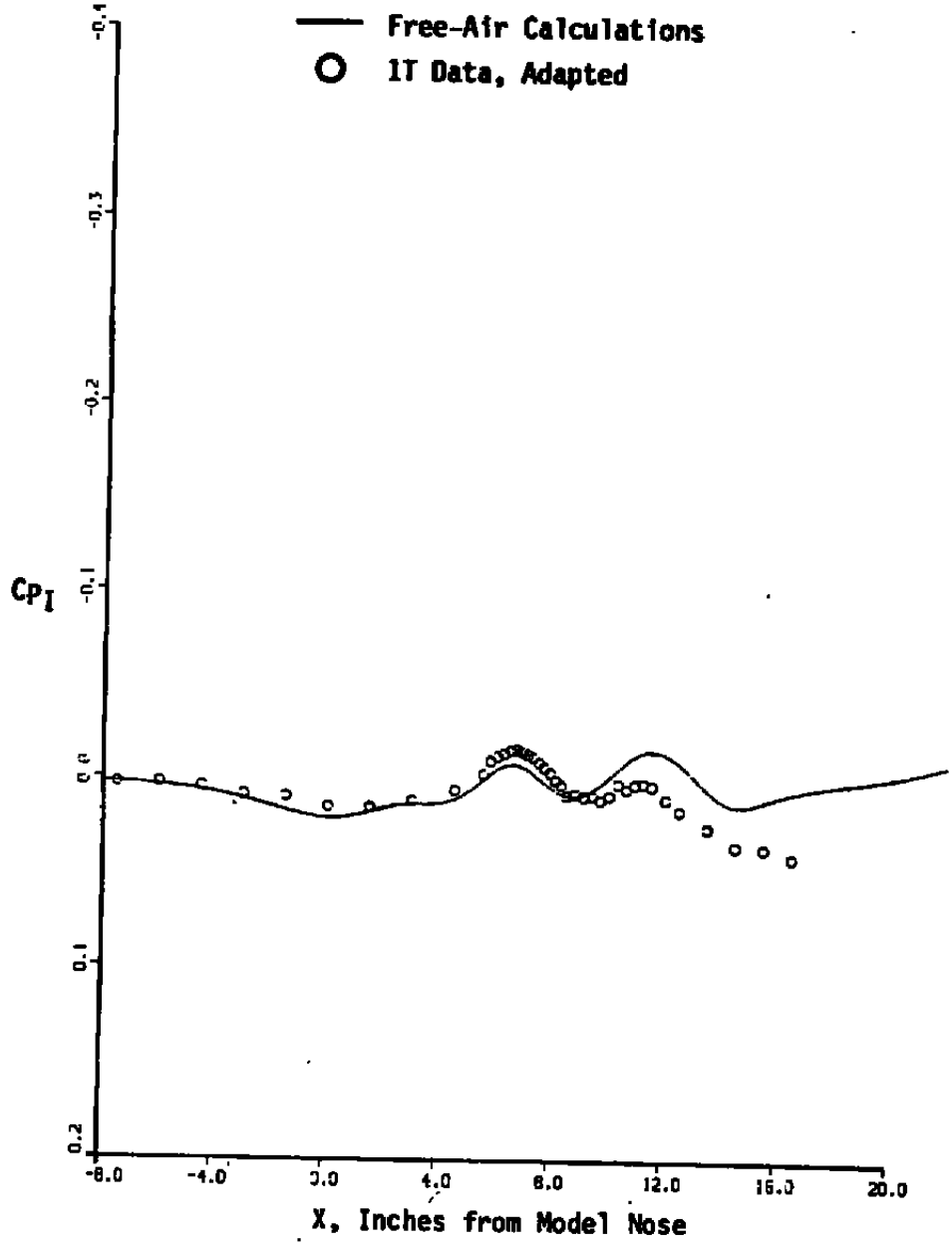

a. θ_p = 15 deg

Figure 27. Interface pressures measured and calculated using the Euler Code, M_E = 0.90 and α_E = 4 deg.

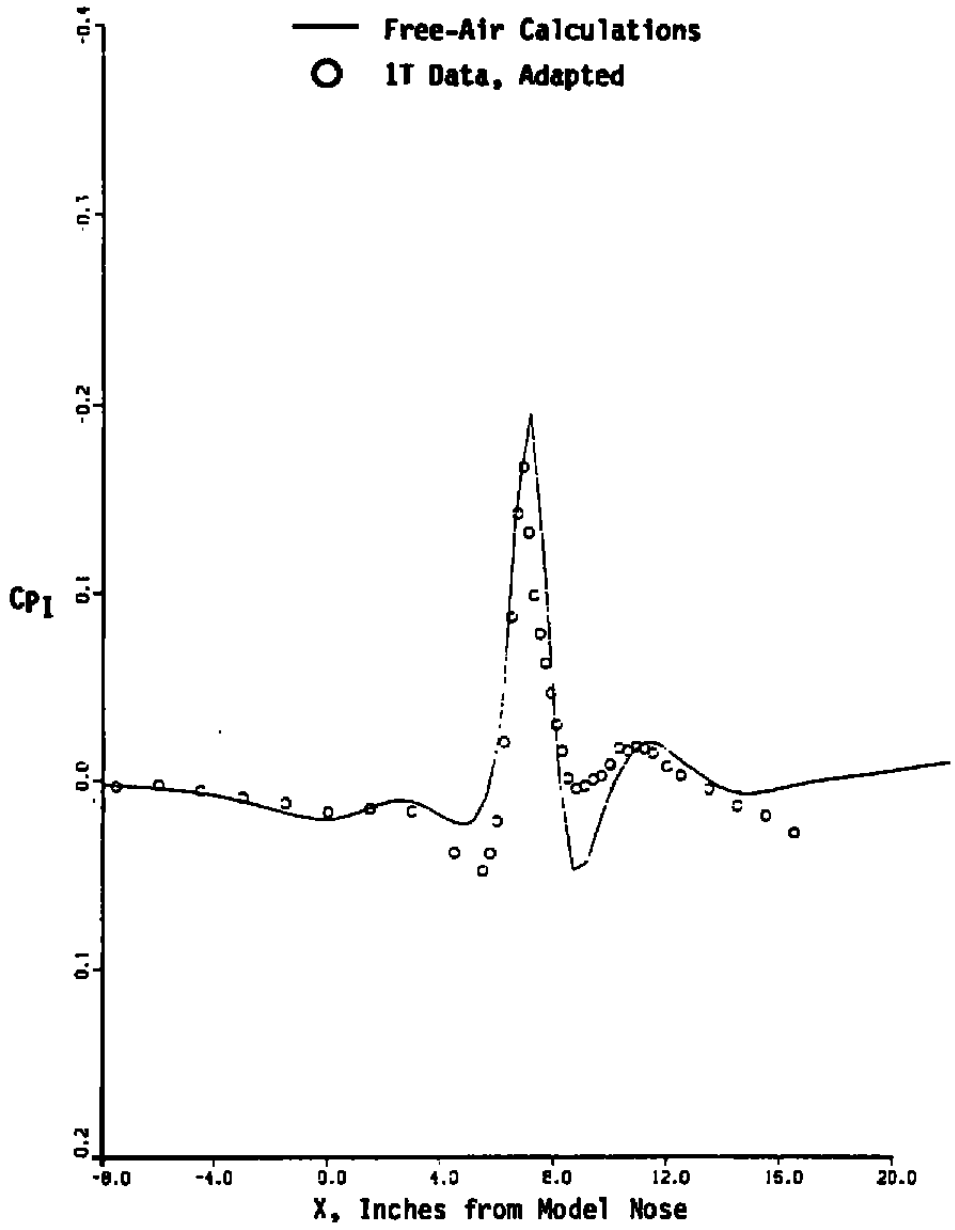

b. θ_p = 85 deg
Figure 27. Continued.

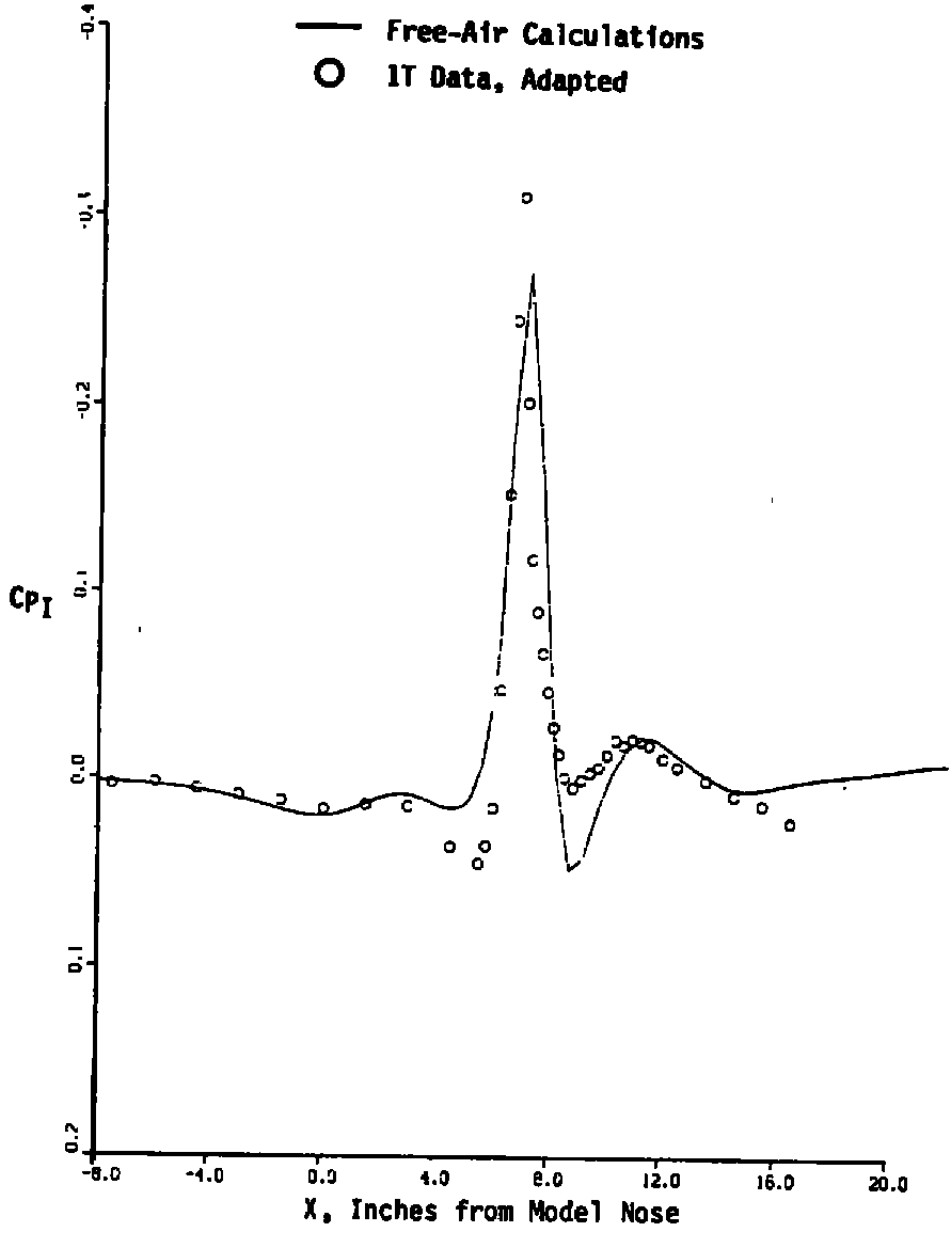

c. θ_p = 95 deg
Figure 27. Continued.

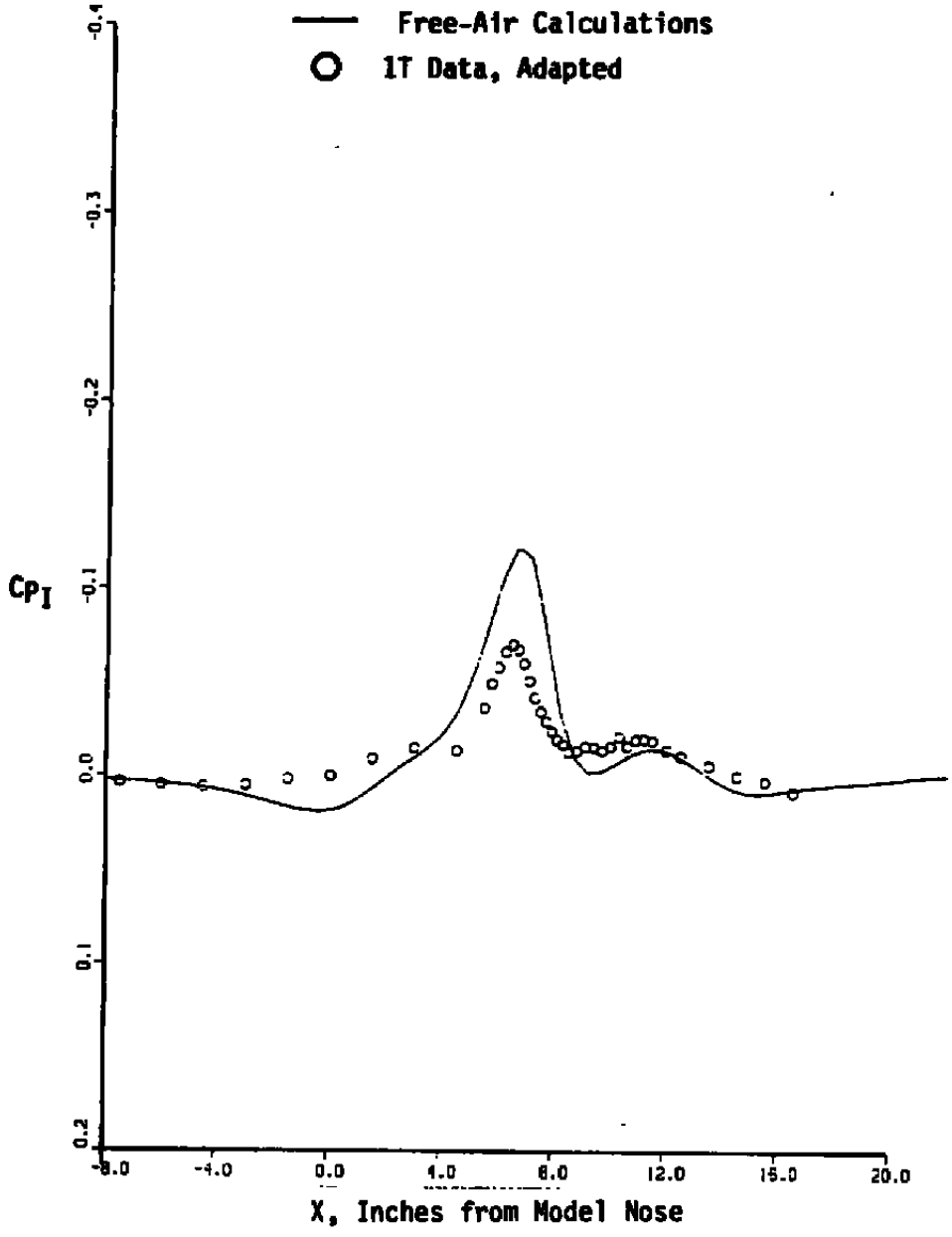

d. θ_p = 165 deg
Figure 27. Concluded.

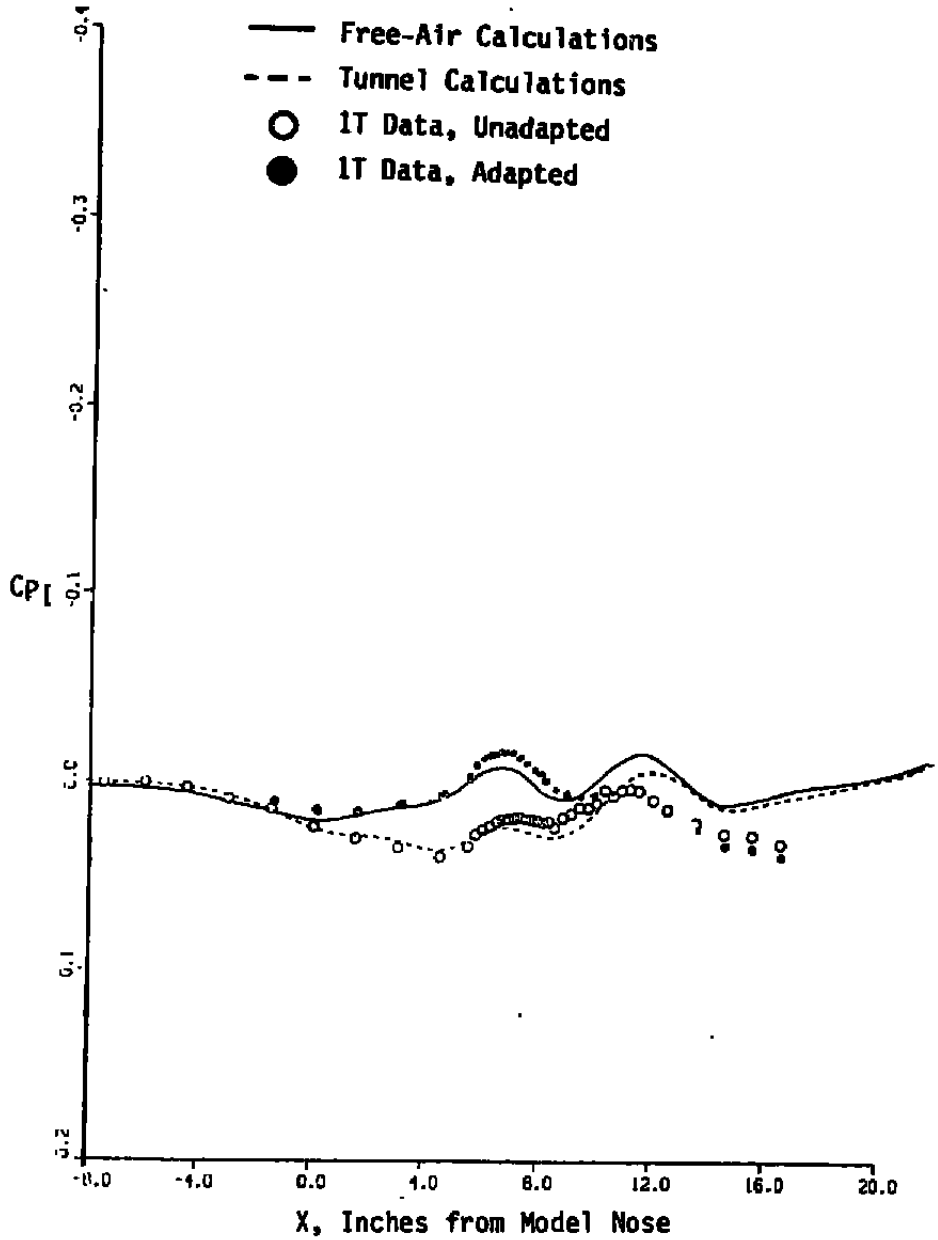

a. θ_p = 15 deg

Figure 28. Interface pressures measured and calculated using the Euler Code, M_E = 0.90, and α_E = 4 deg.

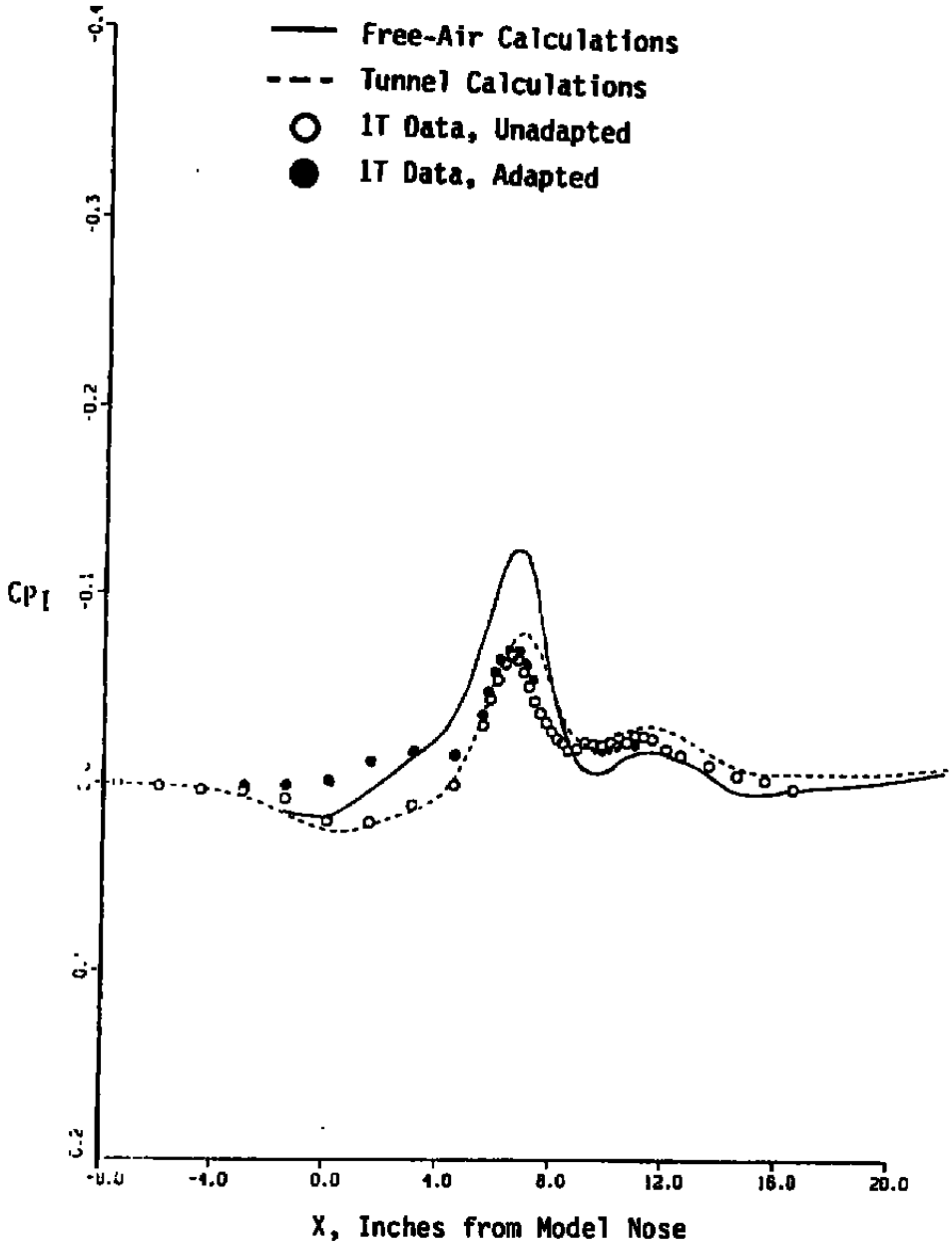

b. θ_p = 165 deg
Figure 28. Concluded.

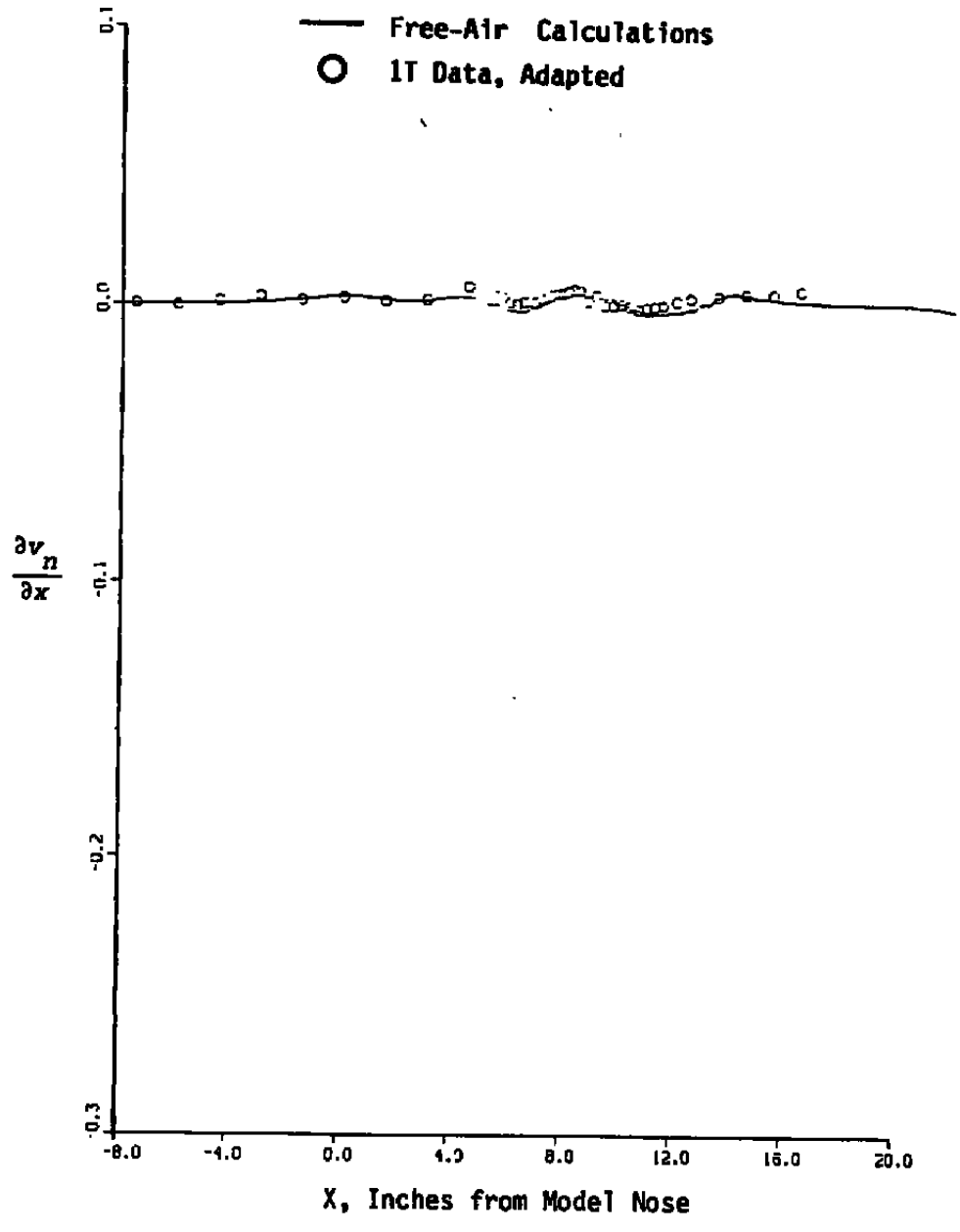

a. θ_p = 15 deg

Figure 29. Interface $\partial v_n/\partial x$ measured and calculated using the Euler Code, M_E = 0.90 and α_E = 4 deg.

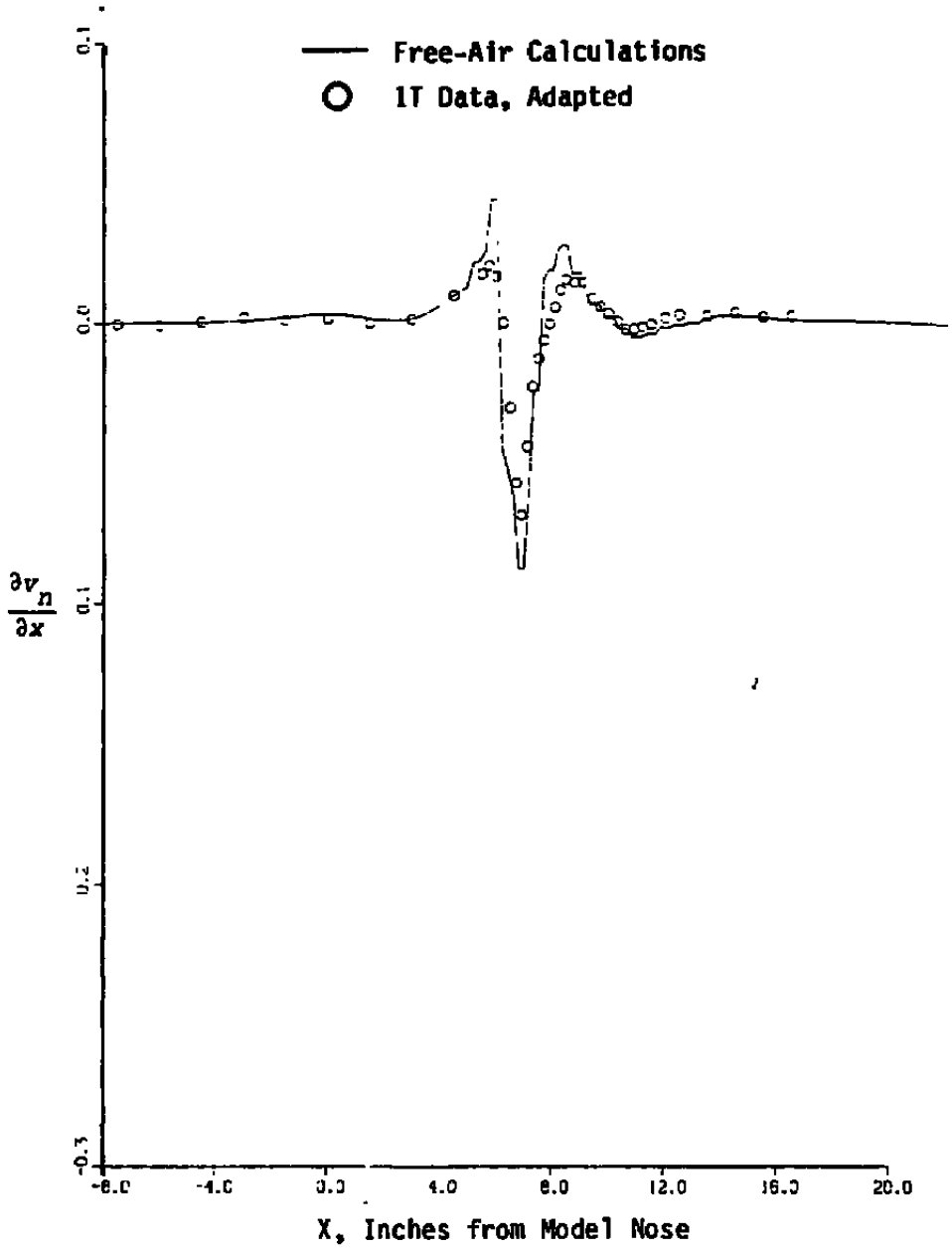

b. θ_p = 85 deg
Figure 29. Continued.

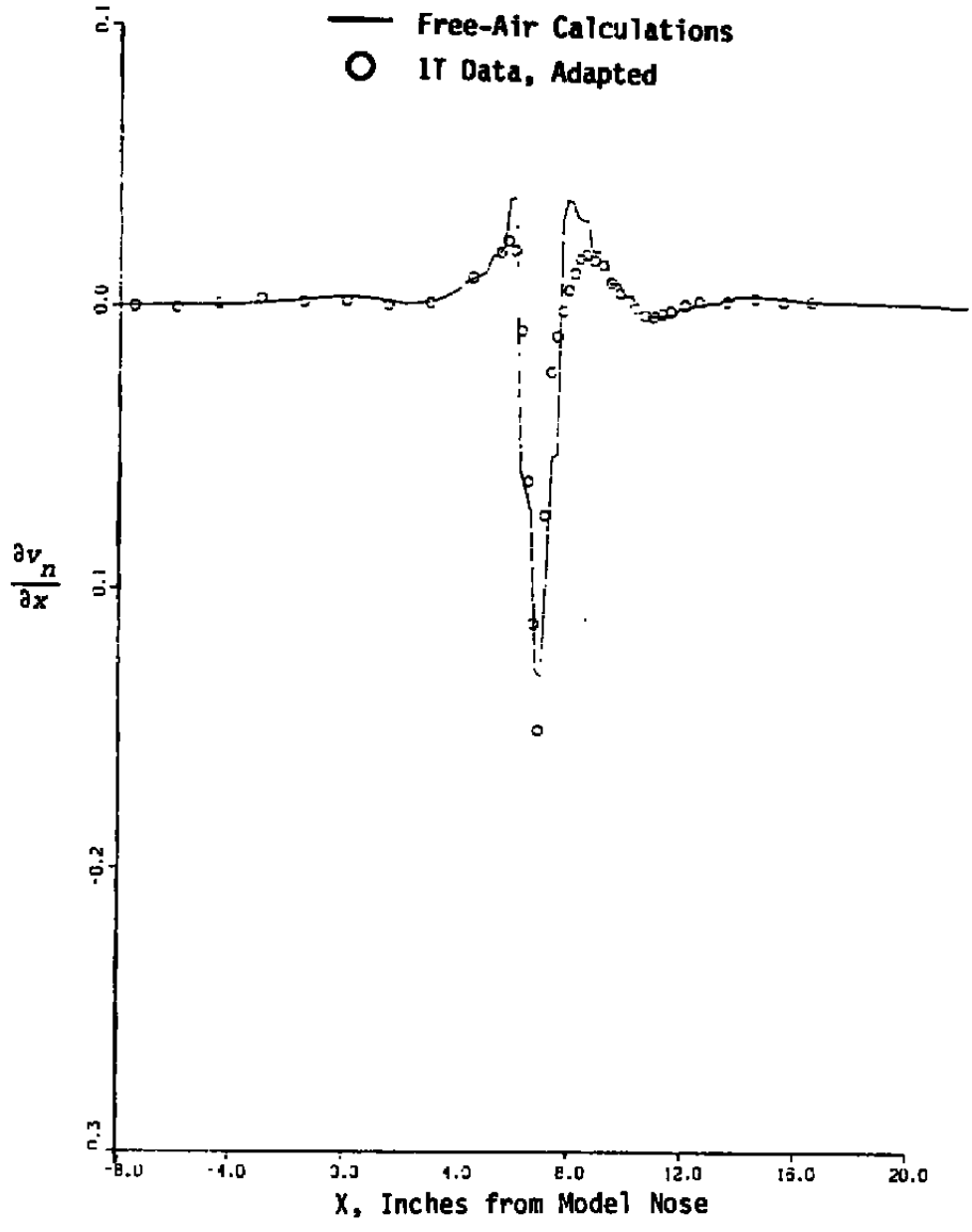

c. θ_p = 95 deg
Figure 29. Continued.

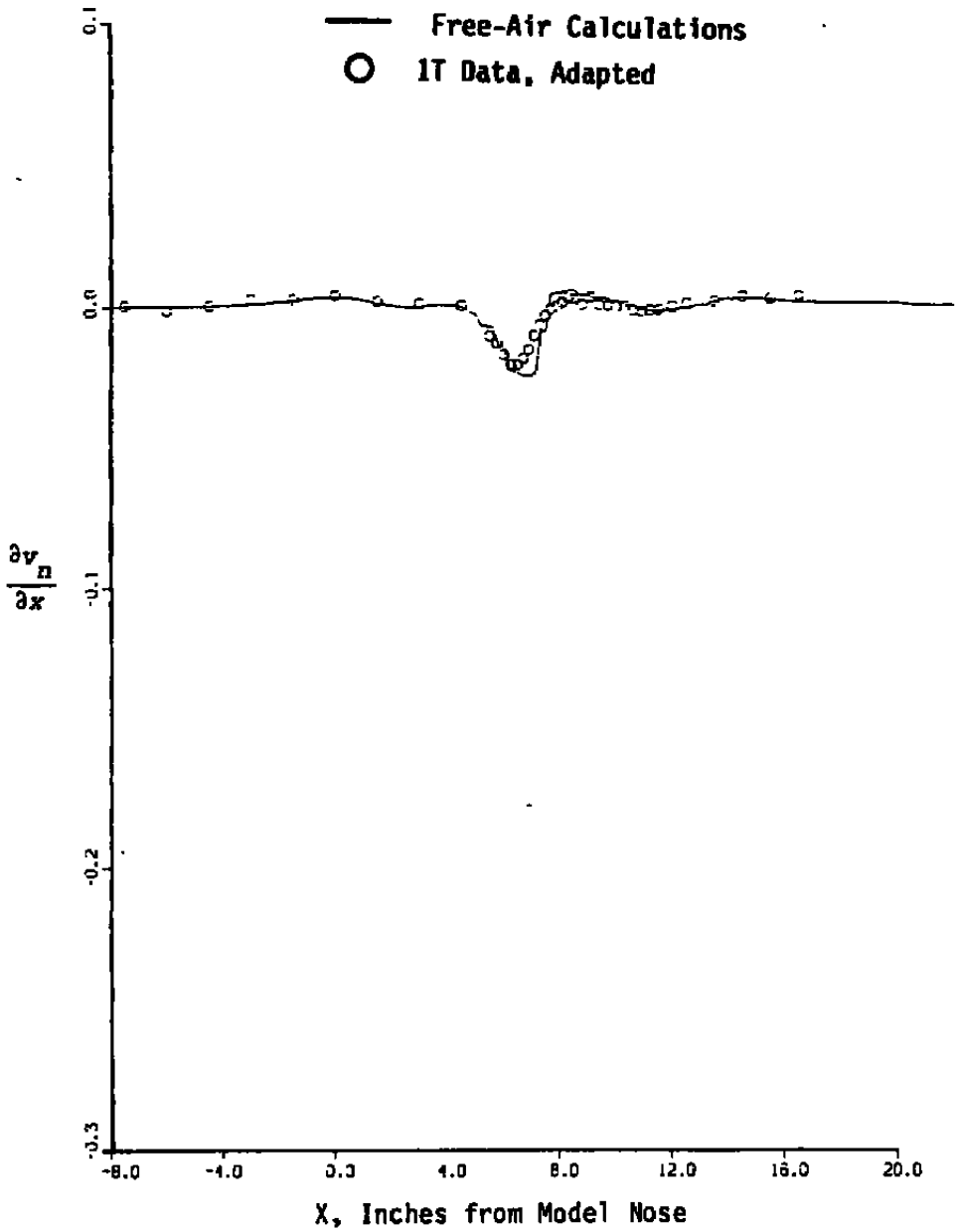

d. θ_p = 165 deg
Figure 29. Concluded.

Table 1. Test Conditions in Aerodynamic Wind Tunnel (1T)

M_E	α_E, deg	τ, percent
0.60	10	2, 5, 7
0.65	0	5
0.65	4	5
0.80	0	2, 5
0.80	2	2, 5
0.80	6	2, 5
0.90	0	2, 5, 7; 3 plus adaptive-wall iterative steps
0.90	2	2, 5, 7
0.90	4	2, 5, 7; 3 plus adaptive-wall iterative steps
0.95	0	2, 5, 7
0.95	2	2, 5, 7
0.95	4	2, 5, 7

Table 2. Lift Coefficient Increments - Subcritical and Mildly Supercritical Cases, SMV-TSD Results.

M_E	α_E, deg	τ, percent	ΔC_{L_E}	$\Delta C_{L_C}(\alpha_E)$	$\Delta C_{L_C}(\alpha_T)$	α_T, deg
0.60	10	2	−0.050	−0.027	0.032	17.2
0.60	10	5	−0.008	0.007	0.068	17.0
0.60	10	7	0.018	0.022	0.078	16.6
0.65	4	5	0.015	0.004	0.023	6.4
0.80	2	2	−0.009	−0.005	0.013	3.2
0.80	6	2	−0.032	−0.017	0.037	9.5
0.80	2	5	0.004	0.006	0.025	3.2
0.80	6	5	0.009	0.010	0.066	9.3

Table 3. Lift Coefficient Increments - Strongly Supercritical Cases, SMV-TSD Results.

M_E	α_E, deg	τ, percent	ΔC_{L_E}	$\Delta C_{L_C}(\alpha_E)$	$\Delta C_{L_C}(\alpha_T)$	α_T, deg
0.90	2	2	−0.017	0.009	0.022	2.5
0.90	4	2	−0.027	0.022	0.040	4.8
0.90	4	3	−0.011	0.028	0.043	4.6
0.90	2	5	−0.006	0.025		
0.90	4	5	−0.013	0.043		
0.90	2	7	−0.007	0.024		
0.90	4	7	0.001	0.050	0.068	4.8
0.95	2	2	−0.016	−0.012		
0.95	4	2	−0.029	0.003		
0.95	2	5	−0.005	0.005		
0.95	4	5	−0.012	0.018		
0.95	2	7	0.000	0.015		
0.95	4	7	0.000	0.029		

Table 4. Lift Coefficient Increments - Comparison of TSD and Euler Flow Solvers, $M_E = 0.90$ and $\alpha_E = 4$ deg

		$\tau = 3$ percent	$\tau = 7$ percent
ΔC_{L_E}		−0.011	0.001
SMV-TSD	$\Delta C_{L_C}(\alpha_E)$	0.028	0.050
	$\Delta C_{L_C}(\alpha_T)$	0.043	0.068
	α_T	4.6 deg	4.8 deg
SMV-Euler	$\Delta C_{L_C}(\alpha_E)$	0.021	0.044
	$\Delta C_{L_C}(\alpha_T)$	0.016	0.040
	α_T	3.3 deg	3.4 deg
Pretest-Euler	$\Delta C_{L_C}(\alpha_E)$	−0.002	0.025
	$\Delta C_{L_C}(\alpha_T)$	−0.002	0.021
	α_T	3.3 deg	3.4 deg

NOMENCLATURE

b	Wing span
C_L	Lift coefficient
C_p	Pressure coefficient
c	Wing chord
L	Model length
L	Lift
M	Mach number
M	Pitching moment
P_c	Tunnel plenum pressure
P_T	Tunnel total pressure
r	Radius of static pipe
S	Model surface
s	Wing span location
x	Streamwise direction
v_n	Velocity normal to interface surface
α	Model angle of attack
ΔC_L	Lift correction (C_{L_∞} - C_{L_T})
ΔC_ℓ	Sectional lift correction, Eq. (4)
ΔC_p	Local pressure correction on model, Eq. (3)

ΔM	Mach number correction
$\Delta\alpha$	Angle-of-attack correction
θ_p	Pipe azimuth (See Fig. 2)
τ	Tunnel porosity

Subscripts

C	Corrected parameter
E	Experimental parameter
FA	Adjusted free-air parameter
I	Interface measurement surface
ℓ	Interior row of pipe orifices, Eqs. (1) and (2); otherwise, lower lifting surface
m	Model surface
T	Tunnel parameter
t	Tail surface
u	Exterior row of pipe orifices, Eqs. (1) and (2); otherwise, upper lifting surface
w	Wing surface
∞	Free-air parameter